

EXPERIMENTAL AND THEORETICAL INVESTIGATION OF HEAVY ION COLLISIONS AT RHIC

NEHÉZION-ÜTKÖZÉSEK KÍSÉRLETI ÉS
ELMÉLETI VIZSGÁLATA A RHIC-NÉL

M.Sc. Thesis

Máté Csanád

ELTE TTK, Department of Atomic Physics
csanad@elte.hu

Supervisor: Tamás Csörgő, Dr. Hung. Acad. Sci.

MTA RMKI KFKI
csorgo@sunserv.kfki.hu

Budapest, Hungary

10th June 2004

Contents

1 Hungarian overview	5
Magyar nyelvű áttekintés	5
1.1. Bevezetés – a fizika módszere	6
1.2. Adatfelvétel – a relativisztikus nehézion-ütköztető	6
1.3. Adatfeldolgozás – korrelációs függvények	7
1.4. Modellépítés – a Buda-Lund hidrodinamikai modell	8
1.5. Összefoglalás	10
2 Introduction	13
2.1 Method of physics	14
2.2 Data taking - the relativistic heavy ion collider	14
2.3 Data analysis - correlation functions	15
2.4 Model building - the Buda-Lund hydro model	15
3 Data taking	17
3.1 Introduction	18
3.2 The Relativistic Heavy Ion Collider	18
3.2.1 Tandem Van de Graaff generator	18
3.2.2 Linear Accelerator	19
3.2.3 The Booster synchrotron	19
3.2.4 The Alternating Gradient Synchrotron	19
3.2.5 The AGS to RHIC transfer line	19
3.2.6 The experiments	19
3.3 The PHENIX	21
3.4 The zero degree calorimeter	24
3.4.1 Goals of the calorimeter	24
3.4.2 Construction of the ZDC	25
3.5 The Shower Max Detector	25
3.6 The online monitoring	26
3.6.1 Beam energy monitoring	27
3.6.2 Vertex position monitoring	27
3.6.3 Beam position monitoring	27
3.6.4 Main expert plots	27
3.6.5 LED signal monitoring	27
3.6.6 Other expert plots	35
3.7 The vernier scan	35
4 Data analysis	41
4.1 Experimental definitions	42
4.1.1 The two-particle correlation function	42
4.1.2 The three-particle correlation function	43
4.2 Goals of measuring the correlation functions	44
4.2.1 Partial coherence and core-halo picture	44

4.3	Details of the analysis	45
4.3.1	Particle identification	45
4.3.2	Cuts	46
4.3.3	Statistics	47
4.4	Results of the analysis	50
4.4.1	Pair distributions	50
4.4.2	Two-particle correlation functions	50
4.4.3	Triplet distributions	51
4.4.4	Three-particle correlation functions	51
4.5	Future	51
4.5.1	Improving cuts	51
4.5.2	Coulomb-correction	51
4.5.3	Fitting the correlation function	51
4.6	Summary	51
5	Model building	66
5.1	The Buda-Lund hydro model	67
5.1.1	Introduction	67
5.1.2	General Buda-Lund hydrodynamics	67
5.2	Axially symmetric Buda-Lund hydro model	69
5.2.1	The emission function	69
5.2.2	Buda-Lund fit results to central Au+Au data	71
5.2.3	Conclusions	74
5.3	Ellipsoidal Buda-Lund hydro model	75
5.3.1	Introduction	75
5.3.2	Buda-Lund hydro for ellipsoidal expansions	76
5.3.3	Integration and saddlepoint approximation	78
5.4	Results from the ellipsoidal model	80
5.4.1	The invariant momentum distribution	80
5.4.2	The elliptic flow	82
5.4.3	The correlation function	82
5.5	Comparing the ellipsoidal model to the data	86
5.5.1	Elliptic flow for tilted ellipsoidal expansion	86
5.5.2	Comparing v_2 to the data	88
5.6	Predictions	90
5.7	Summary and conclusions	91
6	Summary	93
	List of tables	95
	List of figures	95
	Acknowledgements	97
	Bibliography	98

Chapter 1

Hungarian overview

Magyar nyelvű áttekintés

Modellen olyan matematikai konstrukciót értünk, amely – bizonyos szóbeli értelmezést hozzáadva – leírja a megfigyelt jelenségeket. Az ilyen matematikai konstrukciót kizárólag és pontosan az igazolja, hogy működik.

Model means a mathematical construction which describes – with the help of a verbal interpretation – the observed phenomena. Such a mathematical construction can be verified solely and exactly through the fact that it works.

NEUMANN JÁNOS

1.1. Bevezetés – a fizika módszere

A fizika, mint a természettudományok általában, hasonlóan működik a pszichoanalízishez, más-képp szólva, a kutatás folyamata egészen analóg azzal a folyamattal, ahogy megismerünk valakit. Először kérdéseket teszünk fel neki, figyeljük, hogyan viselkedik adott szituációkban, majd megpróbáljuk megérteni, feldolgozni, hogy mit válaszolt, hogyan reagált, végül pedig a válaszai, reakciói alapján kialakítunk róla egy képet.

Ami ezt az egész folyamatot egy állandóan emelkedő spirállá teszi, az az, hogy amikor – a kialakult képen finomítani akarván –, az addigi válaszokkal összhangban újabb kérdéseket teszünk fel, akkor újabb válaszokat kapunk, ezek pedig felvetik az újabb kérdéseket, és így tovább.

A fizikában nagyon fontos ezt a folyamatot egészében látni. Ugyanis míg a személyes kapcsolatok területén ez általában magától működik, a feladatok nagy részét ösztönösen végzi az ember, addig a tudományban az egyes részfeladatok sikeres elsajátításához hosszú évek gyakorlata szükséges. Ezáltal nehéz összehangolni az egyes részfolyamatokat, amelyeket gyakran nem is ugyanazok az emberek végeznek.

Mik is tehát ezek a feladatok? Íme, a lista, az analógiákkal együtt:

- Adatfelvétel \Leftrightarrow Kérdésfeltevés
- Adatfeldolgozás \Leftrightarrow A válaszok megértése
- Modellépítés \Leftrightarrow A válaszadó keresése a válaszok mögött

Ha nem látjuk az egész folyamatot egyben, csak az egyes részfeladatokra koncentrálunk, a problémák sokkal bonyolultabbá válhatnak számunkra, mint amilyenek valójában. Ugyanis ki tudhatná jobban, hogy milyen kérdést kellene feltenni még, mint az, aki a válaszadó természetét kutatja? Ha ráhagyjuk a kérdésfeltevőre, kérdezzen, amit akar, könnyen zsákutcába kerülhetünk. A kérdésfeltevő pedig segíthet megérteni a választ, mivel ő rendelkezik a legpontosabb ismeretekkel a feltett kérdésekről.

Szakdolgozatomban mindhárom feladat részleteibe szeretnék betekintést engedni az olvasónak. A példák mind a nagyenergiás nehézion-fizika területéről származnak, de más és más feladatokról szólnak.

Ezen rövid bevezető után lássuk a részleteket.

1.2. Adatfelvétel – a relativisztikus nehézion-ütköztető

Nhézion-fizikában jelen pillanatban a legfontosabb és legérdekesebb kérdéseket a RHIC-nél, a relativisztikus nehézion-ütköztetőnél lehet feltenni a természetnek. Itt, a nevének megfelelően fénysebességhez igen közeli relatív sebességű nehézionokat ütköztetnek egymással. Ezekben az ütközésekben olyan körülmények jönnek létre, amilyenek talán legutoljára Világegyetemünk létrejöttékor, a Nagy Bumm idején uralkodtak. Emiatt a nehézion-ütközéseket – a bennük uralkodó óriási energiasűrűség és hőmérséklet miatt – Kis Bummnak is nevezhetjük.

Amikor a felgyorsított nehézionok – melyek a Lorentz-kontrakció hatására két lapos korongnak tűnnek – szembetalálkoznak és összeütköznek, a létrejött hatalmas energiasűrűségnek köszönhetően anyaguk a megszokottól egészen eltérően viselkedik, a protonok és a neutronok felbomlanak, és új részecskék hadát hozzák létre. A nagy energiasűrűség miatt a nyomás is igen nagy, ez pedig azonnal szétveti az addig kis térfogatba koncentrált anyagot, amely hűlni kezd, majd mire – különféle, jól ismert részecskék formájában – az ütközési pont köré rendezett detektorainkba ér, újra a megszokott formáját mutatja. Azonban az észlelt részecskék fizikai jellemzőit (impulzusát, energiáját, tömegét, töltését ...) megmérve, eloszlásukat vizsgálva, fontos információkat kaphatunk arról, hogy milyen is volt az az anyag, amely közvetlenül az ütközés után létrejött.

Detektoraink segítségével így különféle kérdéseket tehetünk fel a természetnek. Az egyik legfontosabb kérdés például, hogy kiszabadulhatnak-e nukleon-börtönükből a protonok és neutronok

építőkövei, a kvarkok és a gluonok, és ha igen, mekkora energiára van ehhez szükség, illetve hogyan viselkedik ez a – kérdéses egzisztenciájú, de már kvark-gluon plazmának elnevezett – régi-új anyag.

Ehhez azonban igen kifinomult detektor-rendszerekre van szükség, amelyek alkalmasak a kérdéseink megválaszolására. Ha például olyan detektort alkalmazunk, amelynek az energia-mérés során mutatott pontatlansága nagyobb, mint egy, az energia-spektrumban várt csúcs szélessége, azt a csúcst sosem fogjuk detektálni. Ezért már a kísérlet megtervezésekor fontos előre tudni, milyen kérdéseket szeretnénk feltenni.

Ezenkívül a feltett kérdésekben szereplő fogalmak tisztázása is rendkívül fontos. Például ha megmérjük valamely pentakvark spektrumát, az elméleti értelmezéshez elengedhetetlen a mérés pontos folyamatának ismerete, különben a mérési eredmény egyes effektusairól kialakult képünk gyökeresen hibás lehet.

Láthatjuk tehát, milyen fontos a kutatás folyamatának lépéseire teljes egészésként tekinteni. Nem mondhatjuk például, hogy „Én kísérleti fizikus vagyok, nem törődöm az elméletekkel”, de azt sem tehetjük, hogy modelleket építünk, gyönyörködünk a szépségükben és tökéletességükben, közben pedig elfelejtjük összehasonlítani őket a természettel. Legyen egy fizikai modell mégoly tökéletes és szemet gyönyörködtető *matematikailag*, ha nem tisztázzuk, hogy a természetet milyen körülmények között és milyen pontossággal tudja leírni, nincs haszna a fizika számára.

Visszatérve a RHIC-nél zajló kísérleti munkára, itt tehát az anyag nagy nyomások és hőmérsékletek hatása alatt tanúsított viselkedését vizsgáljuk, az ilyen körülmények között létrejövő részecskék detektálása által. A részecskék sokfélesége és széles energiatartományban való előfordulása miatt detektorok egész sorára van szükség, hogy megfelelő képet kapjunk az ütközés során végbemenő folyamatokról. A RHIC gyorsítógyűrűjében egymással szemben keringő nehézionok pályája hat ponton keresztezi egymást, ezen kereszteződésekből négyenél telepítettek kísérletet, más és más speciális adottságokkal, hogy kérdések minél szélesebb körére kaphassunk válaszokat.

Magam a PHENIX kísérletnél dolgoztam az adatfelvételen, ezen kívül speciálisan a Zero Degree Calorimeter (ZDC) nevű detektor fejlesztésében és üzemeltetésében vettem részt. Az általános felügyelet és az itt-ott felmerülő problémák kezelése mellett saját feladatomban az úgynevezett Online Monitoring szoftverrendszer ZDC-re vonatkozó részének megírása és folyamatos fejlesztése volt. Ez a szoftverrendszer arra szolgál, hogy a kísérletet folyamatosan felügyelő személyzet (amely az ottani kutatásokon dolgozó, fejenként néhány hét felügyeletet vállaló fizikusokból tevődik össze) számára lehetővé teszi, hogy különösebb speciális ismeret nélkül el tudja dönteni, hogy az egyes detektorok által felvett adatok olyanok-e, amilyenek várjuk őket, amilyenekre szükség van.

A ZDC a nehézion-nyaláb tulajdonságait tudja mérni: az energiáját, a nyalábirányra merőleges síkban vett eloszlását; ezen kívül alkalmas az ütközés nyalábirányú pozíciójának meghatározására. Én ezen méréseket végeztem el és automatizáltam a kaloriméter segítségével, eredményük valós idejű megjelenítését illetve adatbázisban való tárolását oldottam meg. Ezen munkát mutatja be szakdolgozatom harmadik fejezete.

Az online monitoring szoftver megtekinthető a [1] számú referenciában.

1.3. Adatfeldolgozás – korrelációs függvények

Az adatfeldolgozás a válaszok dekódolását és megértését jelenti. Nehézion-fizikában ez konkrétan a következő folyamatot takarja:

1. A detektorok digitalizált jeleiből kiszűrjük az egyes eseményeknek megfelelő adathalmazokat
2. Ezeknek kiválogatjuk az egyes részecskékhez tartozó részeit
3. Meghatározzuk az egyes részecskék fizikai tulajdonságait (tömeg, töltés, impulzus ...)
4. Kiszámoljuk a kívánt mennyiséget (például a pionok energia-eloszlását)
5. Értelmezzük a kapott eredményt (a mérés körülményeit és pontosságát figyelembe véve)

Az én feladatomban a két- és három-részecske korrelációs függvények vizsgálata volt. Ezen függvények megmutatják – közvetve –, hogy mekkora a valószínűsége annak, hogy találunk egy részecskepárt illetve részecskehármaszt adott impulzusokkal. Ezeket a függvényeket azután a relatív impulzusok függvényében szokás megmérni. Ha ezek után a kétrészecske korrelációs függvény értéke – például – kis relatív impulzusnál nagy, az azt jelenti, hogy a részecskék jellegzetesen közel azonos impulzusú párokba rendeződnek. Ha ugyanez az érték igen kicsi, az azt jelenti, hogy nem nagyon találhatunk két részecskét azonos impulzussal. Ez jellemző például az azonos típusú fermionokra, amelyeknek nem *lehet* azonos impulzusuk, ha minden egyéb tulajdonságuk megegyezik.

Hasonló módon lehet vizsgálni a több- vagy n -részecske korrelációs függvényeket, ezeket C_n -nel jelöljük. Ezek összességében részletesebb információt adnak a részecske-sokaság viselkedéséről, mint a kétrészecske korrelációs függvény önmagában. Mint látni fogjuk, bizonyos kérdések megválaszolásához nem elég C_2 meghatározása, hanem szükséges a magasabb rendű korrelációk analízise is.

Hanbury-Brown és Twiss csillagok rádiótartományban mért jelének intenzitáskorrelációit elemezve észrevette [2], hogy a kétpont korrelációs függvény (a kétrészecske korrelációs függvénynek megfelelő mennyiség folytonos eloszlásokra) információt hordoz a forrás geometriájáról. Ez a módszer nehézion-ütközésekben is alkalmasnak látszott a forrás geometriájának megismerésére. Később kiderült, hogy utóbbi esetben a forrás egyéb jellemzői (tágulása, hőmérsékletének változása) is befolyással vannak a korrelációra, ezért ezen mennyiségek megmérése különösen fontos.

Például ha feltesszük, hogy a forrás egy ritka, hideg tartományra és egy hidrodinamikai táguláson keresztül, termalizált részre osztható, ezenkívül utóbbinak van koherens és nem koherens része, akkor ezen részek aránya, mint paraméter a segítségével az n -részecske korrelációs függvények nulla relatív impulzusnál vett értéke kiszámolható. Amennyiben utóbbiak közül kettőt megmérünk, meghatározhatjuk az előbbi arányokat.

De amíg a részecskék impulzus- és energia-eloszlásából megkapjuk a korrelációs függvényeket, hosszú utat kell megtennünk. Többek között tömegük és töltésük alapján, a detektorok hatásfokának és pontosságának ismeretében azonosítanunk kell a részecskéket, különféle vágásokat kell alkalmaznunk az adatokon, hogy csak a *megfelelő* eseményeket és részecskéket használjuk fel, illetve az eredményt bizonyos hatások figyelembevételével korrigálnunk kell.

Én a PHENIX 200 GeV-es arany-arany ütközéseinek adatai alapján számoltam ki a két- és háromrészecske korrelációs függvényeket. Választottam egy megfelelő részecskeazonosítási módszert, alkalmaztam a szükséges egy- és kétrészecske vágásokat, és kiszámítottam az aktuális és a háttér pár és triplet eloszlásokat pionokra, kaonokra, protonokra és azonosítatlan részecskékre, az összes lehetséges töltéskombináció esetében. A mérés (számolás) menete a negyedik fejezet első és harmadik részében szerepel részletesen. A kiszámított eloszlások ismeretében meghatároztam a nyers korrelációs függvényeket. Nyers korrelációs függvények ezek, mert nem végeztem el rajtuk olyan korrekciókat, mint például a Coulomb-korrekció, amely a részecskék közötti elektromágneses kölcsönhatás okozta torzulást veszi figyelembe.

A kiszámított korrelációs függvények a várt alakot mutatják, nagy impulzuskülönbségeknél egyhez tartanak, kis relatív impulzusoknál pedig megnő az értékük. Azonban szembevetve a rossz statisztika, a jövőben elsősorban ezen kell javítani – a felvett adatok nagyobb részének feldolgozásával –, ugyanis éppen a legérdekesebb tartományban, kis relatív impulzusoknál van kevés részecskepár és triplet. A mérés majd a szükséges korrekciók elvégzésével zárul.

1.4. Modellépítés – a Buda-Lund hidrodinamikai modell

Azért építünk modelleket, hogy megismerjük a válaszok mögött a válaszadót. Elképzelünk lehetséges válaszolókat, és megnézzük, a miénk is úgy válaszol-e, mint ahogy az elképzelt, a *modell*. Ha igen, tovább kérdezzük, hogy megtaláljuk a korlátait, vagy pontosan megtudjuk, mik is az érvényességének keretei. Ha olyan választ kapunk, amit a modellünknek megfelelő valóság sohasem adott volna, akkor, ha lehet, modellünket módosítjuk úgy, hogy mégis alkalmazható legyen, illetve tovább kérdezzük, hátha esetleg mégis találunk olyan körülményeket, amelyek mellett alkalmazható. Általában mindenesetre az igazi kihívás találni egyetlen olyan modellt is, amely

megfelel a látott képnek, azaz *leírja a valóság megfigyelt szegmensét*. Ha ez sikerül, akkor pedig el kell kezdeni olyan kérdéseket keresni, amelyekre nem tudjuk a természet választát, viszont predikciót, jóslatot tudunk tenni a saját modellünk alapján. Ezzel a lépéssel visszajutunk az elsőtől, az adatfelvételhez.

Modellépítésen belül konkrétan a Buda-Lund hidrodinamikai modellel foglalkoztam, amely a valóság nagyenergiás nehézion-ütközésekben, a „kis bummokban” mutatott arcát hivatott leírni [3]. A hidrodinamika egyenleteire ad egy megoldást, amelyből paramétereinek adott értéke esetén már ki lehet számítani különféle részecskespektrumokat, korrelációs függvényeket és egyéb, nehézion-ütközésekben mért mennyiségeket.

A modell az ütközések „forró zónájában” létrejövő tűzgömbből indul ki, paramétereit pedig ezen tűzgömb hőmérsékleti és áramlási profilját határozzák meg. Ha a modell eredményeit a paraméterek értékét változtatva illesztjük a mérési eredményekhez, akkor azon kívül, hogy meg tudjuk, hogy működik-e a modell, a paraméterek értékét is meghatározhatjuk.

Végül a kapott paraméter-értékekkel jóslatokat tehetünk nem illesztett mennyiségekre is. Az ezekre vonatkozó kísérleti adatok segítségével finomíthatunk a modellen, és tisztább képet kaphatunk a valóságról. De azt, hogy milyen mennyiségeket lenne még érdemes megmérni, csak a modell készítői és fejlesztői tudják, ezért is kiemelkedően fontos az elméleti és a kísérleti munka összehangolása.

Szakdolgozatom 5. fejezetében a fentiek alapján először az eredeti, tengelyszimmetrikus, nem-relativisztikus Buda-Lund modell eredményeit vizsgálom meg a kísérleti adatok tükrében.

A 5.1 táblázat és az 5.1-5.2 ábrák alapján megállapítható, hogy a Buda-Lund modell jól működik mindkét RHIC energiánál, leírja az egyrészecske-spektrumok és korrelációs sugarak transzverz impulzus függését. Ez a korábban – meglehetősen gyakran – „RHIC HBT rejtvényként” emlegetett probléma megoldásának tekinthető, ugyanakkor az erre vonatkozó irodalom alapján kitűnik, hogy ez a „rejtvény” csak olyan modellekben volt jelen, amelyek nem vették figyelembe a CERN SPS eredményeit.

Megállapíthatjuk, hogy a modell alapján a legcentrálisabb (0-5%), $\sqrt{s_{NN}} = 130$ GeV-es arany-arany ütközésekben létrejövő tűzgömb középponti hőmérséklete kifagyáskor $T_0 = 214 \pm 7$ MeV, bariokémiai potenciálja pedig $\mu_B = 77 \pm 38$ MeV. A legújabb ráctérelméleti számítások alapján a kvark-gluon plazmába való átalakulás kritikus hőmérséklete a $0 \leq \mu_B \leq 300$ MeV intervallumban hibán belül a konstans $T_c = 164 \pm 3$ MeV értéket veszi fel (lásd [22] és [23], háromszoros illetve valós kvarktömegekkel számolva). Ez, és a fenti eredmények alapján a (T, μ_B) érték a RHIC $\sqrt{s_{NN}} = 130$ GeV-es arany-arany ütközéseiben kifagyáskor szignifikánsan a kritikus vonal felett van. Ez a viselkedés a kvarkok kiszabadulására való erős utalásként értelmezhető.

Hasonló jelenséget tapasztalhatunk $\sqrt{s_{NN}} = 200$ GeV-es ütközések esetében, ahol 0-30% centralitási adatokat dolgoztunk fel. Ugyanakkor itt a modell és a fittelés jelenlegi pontossága és az illesztett PHENIX és BRAHMS adatok alapján nem tehetünk a fentiekkel azonos erősségű kijelentést. Azonban megállapíthatjuk, hogy $\sqrt{s_{NN}} = 200$ GeV-es ütközésekben is a kvark-gluon plazmába való átalakulás nyomaként értelmezhető jelet találtunk.

Az 5. fejezet következő részében bemutatom a Buda-Lund modell elliptikusan szimmetrikus esetre való általánosítását. Megtartottam az egyrészecske-spektrumok és korrelációs függvények illesztéséből meghatározott paramétereket, és ezeket felhasználva az általánosított modellt összehasonlítottam a kísérleti adatokkal.

Azt kaptam, hogy a tűzgömb két transzverz irányban vett tágulási sebességének csekély felhasadása és a forrás kis elforgatása elég ahhoz, hogy egyszerre leírjuk a spektrum második harmonikus momentumának, az elliptikus folyásnak a transzverz momentum [25] és pszeudorapiditás függését [26, 27].

Az eredményeket az 5.5 és az 5.6 ábrákon és az 5.2 táblázatban mutatom be. Ezek megerősítik a kvarkok kiszabadulására, a kvark-gluon plazma létrejöttére korábban talált utalást (lásd 5.2. részt és a [66, 19] referenciákat). Ez azon a megfigyelésen alapszik, hogy a részecskék egy hányada egy a kritikusnál nagyobb hőmérsékletű, $T > T_c = 170$ MeV tartományból származik. A modell alapján megbecsültem, hogy ezen $\tau = \tau_0$ hiperfelületen vett tartomány térfogata a teljes térfogatnak hozzávetőlegesen $1/8$ -a, azaz 754 fm^3 .

Ez a megfigyelés, hogy a hőmérséklet egyes térrészekben magasabb a kritikusnál, azonban

csak jel, más szavakkal az új fázis létrejöttére vonatkozó indirekt bizonyíték vagy utalás, mert a kritikus hőmérsékletet nem közvetlenül az adatokból határoztuk meg, hanem egyszerűen átvettük a legfrissebb rácstérelméleti eredményeket.

Az analízis ugyanakkor azt is megmutatja, hogy a forrás átlagos hőmérséklete lényegesen kisebb, $T_s \approx 105$ MeV, így a részecskék legnagyobb része egy hideg hadron gázból származik.

Ezen eredményeket a RHIC $\sqrt{s_{NN}} = 130$ GeV-es arany-arany ütközéseiben a kvark-gluon plazma illetve egy cross-over jellegű átmenet nyomaként lehet értelmezni.

1.5. Összefoglalás

Szakedolgozatomban bemutatom a természet fizika általi megismerésének folyamatának három fő lépését, az adatfelvételt, az adatanalízist és a modellépítést, egy-egy példán keresztül.

A magyar nyelvű összefoglaló és a bevezetés után a 3. fejezetben a RHIC-ről, a Relativisztikus Nehézion Ütköztetőről írok, ezen kívül a PHENIX kísérlet Zero Degree Calorimeter nevű berendezésének működtetéséről és az általa felvett adatokról. Itt a következő munkákat végeztem el:

- Az adatfelvétel időszakos felügyelete a PHENIX kísérletnél
- A Zero Degree Calorimeter online monitoring szoftverének kifejlesztése és karbantartása (3.6. rész)
- A Zero Degree Calorimeterhez kapcsolódó kisebb-nagyobb munkák elvégzése
 - Vernier scan analízis (3.7. rész)
 - Szakértői felügyelet (3.4. rész)

Tovább haladva a 4. fejezetben az adatanalízis terén végzett munkámat mutatom be, ennek eredménye a PHENIX 200 GeV-es arany-arany adatokból kiszámolt két- és háromrészecske korrelációs függvények pionokra, kaonokra, protonokra és azonosítatlan részecskékre, az összes lehetséges töltéskombináció esetében.

A munka lépései a következők voltak:

- Az felvett adatok struktúrájának megismerése, részecskeazonosítás, eseményselekción, vágások elvégzése (4.3. rész)
- Pár- és triplet-eloszlások kiszámítása (4.4.1. és 4.4.3 részek)
- Nyers két- és három-részecske korrelációs függvények kiszámítása (4.4.2. és 4.4.4. részek)
- Az eredmények értelmezése, további feladatok meghatározása (4.5. és 4.6. részek)

Az 5. fejezetben a folyamat utolsó lépését, az elméleti munkát, a modellépítést mutatom be. A Buda-Lund modellel foglalkoztam, a RHIC adataira való fitteléssel illetve az eredeti, nemrelativisztikus és tengelyszimmetrikus modell elliptikus szimmetriára és relativisztikus alakra való általánosításával. Részletesen a következő feladatokat végeztem el:

- Az eredeti modell feldolgozása (5.1. rész)
- Centrális ütközések vizsgálatában való részvétel (5.2. rész)
 - Nyeregponatok pontosabb megkeresése
 - A modell eredményeinek újraszámolása
- Elliptikus, relativisztikus esetre általánosított modell kialakítása (5.3. rész)
- Az általánosított modelltől mérhető mennyiségek kiszámítása (5.4. rész)
- Az általánosított modell adatokkal való összehasonlítása (5.5. rész)
- Predikciók új mérhető mennyiségekre (5.6. és 5.4.3. rész)

Tudományos publikációk

- 1. Indication of quark deconfinement and evidence for a Hubble flow in 130 and 200 GeV Au+Au collisions**
M. Csanád, T. Csörgő, B. Lörstad, A. Ster
Accepted by Journal of Physics G
<http://arXiv.org/pdf/nucl-th/0403074>

- 2. A hint at quark deconfinement in 200 GeV Au+Au data at RHIC**
M. Csanád, T. Csörgő, B. Lörstad, A. Ster
Accepted by Nukleonika
<http://arXiv.org/pdf/nucl-th/0402037>

- 3. Buda-Lund hydro model and the elliptic flow at RHIC**
M. Csanád, T. Csörgő, B. Lörstad
Accepted by Nukleonika
<http://arXiv.org/pdf/nucl-th/0402036>

- 4. An indication for deconfinement in Au+Au collisions at RHIC**
M. Csanád, T. Csörgő, B. Lörstad, A. Ster
Acta Phys. Polon. B35:191-196, 2004
<http://arXiv.org/pdf/nucl-th/0311102>

- 5. Buda-Lund hydro model for ellipsoidally symmetric fireballs and the elliptic flow at RHIC**
M. Csanád, T. Csörgő, B. Lörstad
Accepted by Nucl. Phys. A
<http://arXiv.org/pdf/nucl-th/0310040>

- 6. Absence of suppression in particle production at large transverse momentum in 200-GeV d+Au collisions**
PHENIX Collaboration (S.S. Adler, ..., M. Csanád, ... et al.)
Phys.Rev.Lett.91:072303,2003
<http://arXiv.org/pdf/nucl-ex/0306021>

- 7. Double helicity asymmetry in inclusive mid-rapidity π_0 production for polarized p+p collisions at $\sqrt{s} = 200$ GeV**
PHENIX Collaboration (S.S. Adler, ..., M. Csanád, ... et al.)
Submitted to Phys.Rev.Lett.
<http://arXiv.org/pdf/hep-ex/0404027>

- 8. Analysis of identified particle yields and Bose-Einstein (HBT) correlations in p+p collisions at RHIC**
T. Csörgő, M. Csanád, B. Lörstad, A. Ster.
To appear in Heavy Ion Physics
<http://arXiv.org/pdf/hep-ph/0406042>

Tudományos előadások

1. **Elliptic flow and correlations from the Buda-Lund model**
2nd Warsaw Meeting on Particle Correlations and Resonances in Heavy Ion Collisions
2003. október 15-18., Varsó, Lengyelország
<http://hirg.if.pw.edu.pl/en/meeting/oct2003/talks/csanad/Csanad.ppt>
2. **Buda-Lund hydro modell and the rapidity dependence of the elliptic flow at RHIC**
3rd Budapest Winter School on Heavy Ion Physics
2003. december 8-11., Budapest, Magyarország
http://www.hef.kun.nl/~novakt/school03/agenda/csanad_bp03.ppt
3. **Indication for quark deconfinement and evidence for a Hubble flow in Au+Au collisions at RHIC**
17th International Conference on Quark Matter
2004. január 11-18., Oakland, California, USA
http://www-rnc.lbl.gov/qm2004/talks/parallel/Tuesday03/MCsanad_PPTWin.ppt
4. **Indication for quark deconfinement and evidence for a Hubble flow in Au+Au collisions at RHIC**
PHENIX Global-Hadron Physics Working Group Meeting
2004. január 30., Upton, New York, USA
https://www.phenix.bnl.gov/WWW/p/draft/csanad/pwg/csanad_pwg_040130.ppt
5. **Three pion correlation function analysis**
PHENIX Global-Hadron Physics Working Group Meeting
2004. április 2., Upton, New York, USA
https://www.phenix.bnl.gov/WWW/p/draft/csanad/pwg/csanad_pwg_040402.ppt
6. **Buda-Lund hydro model**
Brookhaven National Laboratory Nuclear Physics Seminar
2004. április 6., Upton, New York, USA
https://www.phenix.bnl.gov/WWW/p/draft/csanad/seminar/csanad_nps_040406.ppt
7. **Buda-Lund hydro in p+p collision at 200 GeV**
PHENIX Global-Hadron Physics Working Group Meeting
2004. május 21., Upton, New York, USA and Budapes, Hungary
https://www.phenix.bnl.gov/WWW/p/draft/csanad/pwg/csanad_pwg_040402.ppt

Konferencia-poszter

1. **Understanding the rapidity dependence of the elliptic flow at RHIC**
17th International Conference on Quark Matter
2004. január 11-18., Oakland, California, USA
<http://qm2004.lbl.gov/>

Chapter 2

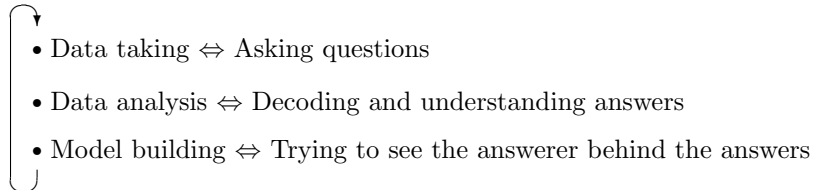
Introduction

*Oh infinite heavens open, open up
Your hidden sacred volumes to my sight*

THE TRAGEDY OF MAN, IMRE MADÁCH

2.1 Method of physics

Physics, as a natural science, works in a way very similar to psychoanalysis, just Nature is our subject of investigation. The three main steps in researching the secrets of nature are data taking, data analysis and model building. These three steps are analogous to a situation, where one wants to get to know another person, by asking questions. The analogies for the three steps are:

- 
- Data taking \Leftrightarrow Asking questions
 - Data analysis \Leftrightarrow Decoding and understanding answers
 - Model building \Leftrightarrow Trying to see the answerer behind the answers

There is one more step, which makes this above process to a continually rising helix. This is represented above by the curved arrow, and means, that a model has to make predictions and call the next questions to see if they are right, and then comes the next answer, the next model and the next prediction, which calls a question again, and so on.

It is very important to see the whole process. For example, the one who does the third task, who tries to discover the source of the answers, knows best what questions to ask, and asker can help to understand answers, because he/she knows to most details about the asked question.

This is not a big problem in the process of getting to know a person, where learning and practicing the separate tasks do not require a whole life, especially the second task, which is done by our ears and brain automatically.

In physics, the situation is not so easy. While the first two tasks are often done by the same people, the third is mostly separated from them. In my present M.Sc. thesis, I would like to show examples for all three tasks. The examples are from the field of heavy ion physics, but they are on different topics, and give insight into different kind of problems.

After this short introduction, let us see a description and some details of the three parts.

2.2 Data taking - the relativistic heavy ion collider

The front line of asking questions from Nature in the field of high energy physics is at heavy ion colliders. Currently, the largest one is in Brookhaven on Long Island, New York, and this is the Relativistic Heavy Ion Collider. Here heavy (or sometimes not so heavy) ions are accelerated to enormous energies and collided to each other. In these high energy collisions lots of new particles are produced, and through observing properties of these particles, we may see circumstances similar to the time when our Universe was created, the Big Bang.

The accelerating is done by linear accelerators and a synchrotron, and then two beams of ions are led in two beampipes which are on the same circle but the ions go in different directions in the two pipes. They cross each other at six points, and at four of these crossings there is an experiment. These experiments are aggregations of detectors, which measure different properties of the particles produced in the collisions.

I was involved in data taking at one of these experiments, in PHENIX (Pioneering High Energy Ion eXperiment). It consists of many detectors, there are some that measure the momentum of the particles, some measure the charge, then time of flight in the detectors and pathlength is measured, and so on.

With these detector-aggregations we can ask questions from nature, for example we could ask:

“Is the spectrum of pions in such collisions a thermal spectrum?”

or

“Are there among the products of these collisions any pentaquarks?”

or

“What is the temperature of the center of the system that comes into existence after the collision?”

First important thing is, that we have to build detectors, which “understand” our questions, eg. if we cannot observe particles with an energy higher than the pion mass, we won’t be able to measure pion spectrum. Or, we have to build detectors, which have a high enough acceptance to measure the decomposition products of pentaquarks. And, our heavy ion collisions have to be intense enough to see lots of particles.

Furthermore, all these questions depend more or less on idea on the meaning of the words in them. For example, it is a question, what we consider as temperature in those collisions, or how we want to see our pentaquarks.

There is a need to see the whole process of physics in one, and not just say: we are experimental physicists, and do not care about theories. Another problem could be, if one builds a model without respect to Nature. A model may be the most original and creative and beautiful model ever made, if it does not describe Nature, it’s beauty does not correct this problem.

My data taking task was specifically to develop and maintain the online monitoring software of PHENIX’s Zero Degree Calorimeter [1].

2.3 Data analysis - correlation functions

Data analysis means decoding and understanding the answers. For example we have to extract the particular events from the digitalized signal of the detectors, the particles in the events and their physical properties. After that, if we have the particles, we can measure eg. the pion spectrum, and in my case, the correlation functions.

Correlation functions measure, how correlated the momenta of the particles in an ensemble are. For example, there are the two particle correlation functions, which depend on the two momenta of particle pairs, but can be projected on the sub-space of the momentum-difference of the pair. If the correlation function is high at zero relative momenta, it means, that there are many particles with nearly the same momentum. We can measure n-particle correlation functions, too, they count, how many particle n-tuple we had at a given momentum n-tuple.

Correlation functions are important to see the collective behavior or properties of particles. For example the observed size of a system can be measured by looking at two particle Bose-Einstein correlations [2], and from the three-particle correlation function we can conclude some other properties of the examined particle-ensemble, because if we see strong correlations, it can be a hint for jets, while less correlated matter means a fireball-like behavior.

But until we get from particle-ensemble to the correlation function, there is a long way, which includes understanding the detectors to be able to make necessary corrections on the measurement and understanding the theory of correlations to be able measure the *right* correlation functions.

2.4 Model building - the Buda-Lund hydro model

We build models to understand the answerer behind the answers. We imagine possible answerers, and if we see, that for example this answerer would have given other answers, that we have heard, we can tell, that the answerer is unlike this picture. And in most cases, the real quest is to find one answerer at all, that would give the same answers. And then, we are back at the first step, ask questions to see, if the answerer is really like what we imagined.

The Buda-Lund model [3] is a hydrodynamical model which was developed to describe the ‘Little Bang’, the heavy ion collisions. It includes a solution of the equations of hydrodynamics, and calculates for a given set of parameters particle spectra, correlations functions and other observable quantities measured in heavy ion collisions. It assumes the existence of an expanding fireball arisen from the hot zone of these collisions, has the fireballs temperature and flow profile

as input parameters. After fitting the results of the model to the data, these input parameters can be determined.

Finally, with the found set of parameters, it is possible to make predictions for not fitted quantities also. If we measure these quantities, we can make refinements on the model to get a more clear picture. But only who works on the model knows, which quantities are to predict from the model, or which measurements could exclude or confirm some characteristic features of the model.

Chapter 3

Data taking

Natura duce errare nullo modo possumus
– *Cannot get lost if lead by nature*

CICERO

3.1 Introduction

Heavy ions are accelerated and collided with relativistic energies at the Brookhaven National Laboratory's RHIC complex. The properties of particles coming from the heavy ion collisions are measured by four experiments, BRAHMS, PHENIX, PHOBOS and STAR. I was working at PHENIX on data taking, my task was specifically to develop and maintain the online monitoring software of PHENIX's Zero Degree Calorimeter for the d+Au, Au+Au and p+p runs. The software calculates from the signals coming from the detectors main properties of the beam, such as energy and transverse profile, as well as the event position. These quantities are then collected on histograms for short time-intervals and put in databases to be able to look at them later. The software is available in ref. [1].

3.2 The Relativistic Heavy Ion Collider

The Relativistic Heavy Ion Collider (RHIC) at Brookhaven National Laboratory is a research facility that began operation in 2000, following 10 years of development and construction. Hundreds of physicists from around the world use RHIC to study what the universe may have looked like in the first few moments after it's creation. RHIC drives two intersecting beams of gold ions head-on into a subatomic collision. These collisions may help us understand more about why the physical world works the way it does, from the smallest subatomic particles, to the largest stars.

An areal view of the RHIC complex with all it's facilities is to see on figure 3.1.

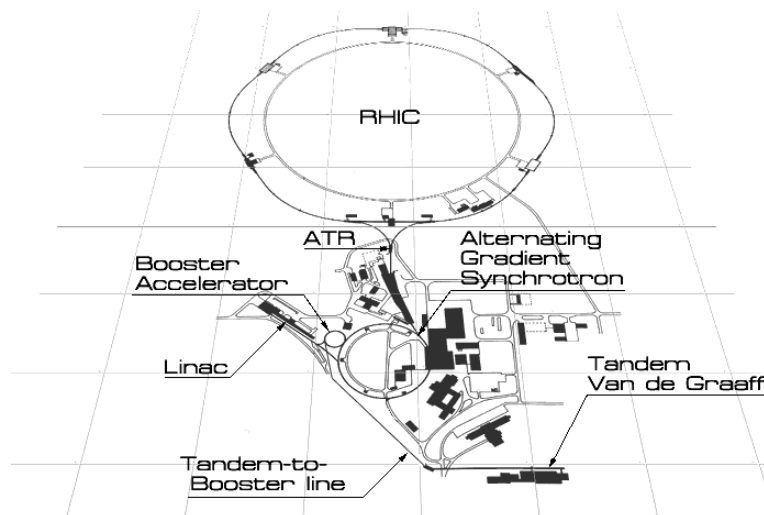


Figure 3.1: Aerial view of RHIC

On this figure, we see the RHIC ring and it's pre-accelerator facilities. Gold ions start their journey in the Tandem Van de Graaff generator, then they travel to the Booster accelerator, after that they are accelerated to a higher speed in the Alternating Gradient Synchrotron, and finally they are injected into the RHIC ring where they reach their final speed and collide into one another.

3.2.1 Tandem Van de Graaff generator

Completed in 1970, the Tandem Van de Graaff facility was for many years the world's largest electrostatic accelerator facility. It provides accelerated ion-beams ranging from hydrogen to uranium. The facility consists of two 15 million volt electrostatic accelerators, each about 24 meters long, aligned end-to-end.

To study heavy ion collisions at high energies, a 700 meter-long tunnel and beam transport system called the Tandem to Booster (TtB) Line was completed in 1986. From the Tandem,

the bunches of ions enter the Tandem to Booster Line, which carries them through a vacuum via a magnetic field to the Booster. At this point, they're traveling at about 5% of the speed of light. This facility allows the delivery of heavy ions from Tandem to the Alternating Gradient Synchrotron (AGS) for further acceleration. The TtB now makes it possible for the Tandem to serve as the Relativistic Heavy Ion Collider's ion source.

3.2.2 Linear Accelerator

In addition to heavy ions, also proton-proton collisions are studied at RHIC. For these measurements, protons are supplied by the Linear Accelerator (Linac).

The basic components of the Linac include ion sources, a radiofrequency quadrupole pre-injector, and nine accelerator radiofrequency cavities spanning the length of 140 meter. The Linac is capable of producing up to a 35 milliamper proton beam at energies up to 200 MeV for injection into the AGS Booster or for the activation of targets at the Brookhaven Linac Isotope Producer. The Linac's location relative to the rest of the AGS complex is shown on figure 3.1.

3.2.3 The Booster synchrotron

The Booster synchrotron is used to pre-accelerate particles entering the AGS ring. It's construction was begun in 1986 and completed in 1991. The Booster is less than one quarter the size of the AGS.

The Booster also plays an important role in the operation of the Relativistic Heavy Ion Collider (RHIC) by accepting heavy ions from the Tandem Van de Graaff facility via the Tandem to Booster beamline. It then feeds them to the AGS for further acceleration and delivery to RHIC. Due to its superior vacuum, the Booster makes it possible for the AGS to accelerate and deliver heavy ions up to gold with its atomic mass of 197.

3.2.4 The Alternating Gradient Synchrotron

The Alternating Gradient Synchrotron name is derived from the concept of alternating gradient focusing, in which the field gradients of the accelerator's 240 magnets are successively alternated inward and outward, permitting particles to be propelled and focused in both the horizontal and vertical plane at the same time. Capable of accelerating 25 trillion protons with every pulse, and heavy ions such as gold and iron, the AGS is used by 850 users from 180 institutions from around the world annually.

As ions enter the AGS from the Booster, they are travelling at about 37% the speed of light. Then in the AGS, the velocity of the ions reaches 99.7% the speed of light.

Since 1960, the Alternating Gradient Synchrotron (AGS) has been one of the world's premiere particle accelerators, well known for the three Nobel Prizes won as a result of research performed there.

3.2.5 The AGS to RHIC transfer line

When the ion beam is travelling at top speed in the AGS, it is diverted to another beam line called the AGS to RHIC transfer line. At the end of this line, there is a "fork in the road", where a switching magnet sends the ion bunches down one of two beam lines. Bunches are directed either left to the clockwise RHIC ring or right to travel counter-clockwise in the second RHIC ring. From here on, the counter-rotating beams are accelerated, as in the Booster and AGS, and then circulate in RHIC where they will be collided into one another at six interaction points.

3.2.6 The experiments

RHIC's 2.4 mile ring has six intersection points where it's two rings cross each other, allowing the particle beams to collide.

If RHIC's ring is thought of as a clock, the four current experiments are at 2 o'clock (BRAHMS), 6 o'clock (STAR), 8 o'clock (PHENIX) and 10 o'clock (PHOBOS) and. There are two additional intersection points at 12 and 4 o'clock where there are no experiments, but in the future some may be placed.

Let us now see some details about the four experiments.

BRAHMS

One of RHIC's two smaller detectors is the Broad Range Hadron Magnetic Spectrometer, or "BRAHMS". This device studies charged hadrons as they pass through its spectrometers.

BRAHMS measures only a small number of particles emerging from a specific set of angles during each collision. The momentum, energy and other characteristics of the particles are measured very precisely.

This collaboration has 51 participants from 14 institutions in eight countries.

PHENIX

The PHENIX detector records many different particles emerging from RHIC collisions, including photons, electrons, muons, and hadrons.

Photons and leptons are not affected by the strong interaction and can emerge unchanged from the interior of a RHIC collision, so they carry unmodified information about processes within the collision. A good analogy is that PHENIX looks "inside" the hot, dense matter formed in the collision, much like x-ray or MRI images show medical doctors the "inside" of the human body. For example, escaping photons can reveal information about the temperature of the collision.

PHENIX weighs 4,000 tons and has a dozen detector subsystems. Three large steel magnets produce high magnetic fields to bend charged particles along curved paths. Tracking chambers record hits along the flight path to measure the curvature and thus determine each particle's momentum. Other detectors identify the particle type and/or measure the particle's energy. Still others record where the collision occurred and determine whether each collision was a central one, a peripheral one, or something in between.

PHENIX has over 450 members from 51 institutions in 11 countries. A more detailed description of PHENIX is shown in the next section.

PHOBOS

The PHOBOS experiment is based on the premise that interesting collisions will be rare, but that when they do occur, new physics will be readily identified. Thus PHOBOS is designed to examine and analyze a very large number of unselected gold ion collisions. It consists of many silicon detectors surrounding the interaction region. With these detectors, it is possible to count the total number of produced particles and study their angular distribution. With this array it is looked for unusual events, such as fluctuations in the number of particles or angular distribution, because it is known from other branches of physics that a characteristic of phase transitions is a fluctuation in observable events.

Seventy scientists from 12 institutions in three nations are working on PHOBOS.

STAR

The Solenoidal Tracker at RHIC (STAR) is an experiment which specializes in tracking the thousands of particles produced by each ion collision at RHIC.

STAR's "heart" is the Time Projection Chamber, which tracks and identifies particles emerging from the heavy ion collisions. As a collision occurs, STAR measures many parameters simultaneously to look for signs of the quark-gluon plasma. By using powerful computers it reconstructs the sub-atomic interactions which produce the particles emerging from the collision.

The STAR team is composed of over 400 scientists and engineers from 33 institutions in 7 countries.

3.3 The PHENIX

The PHENIX Experiment consists of a collection of detectors, each of which perform a specific role in the measurement of the results of a heavy ion collision. The detectors are grouped into two central arms, which are capable of measuring a variety of particles including pions, protons, kaons, deuterons, photons, and electrons, and two muon arms which focus on the measurement of muon particles. There are also additional event characterization detectors that provide additional information about a collision, and a set of three huge magnets that bend the trajectories of the charged particles. In table 3.1 is a list of the detectors of PHENIX and what they do. How the detectors are arranged in the experiment is to see on figure 3.2.

Central Arm Detectors	
Drift Chamber (DC)	Measures the position and momentum of charged particles
Pad Chambers (PC)	Measures the position of charged particles with precision
Ring Imaging Cherenkov Detector (RICH)	Identifies electrons
Time Expansion Chamber (TEC)	Measures the position and momentum of charged particles. Identifies particles.
Time-of-Flight (TOF)	Measures the position of charged particles. Identifies particles.
Electromagnetic Calorimeter (EMCal)	Measures the position and energy of charged and neutral particles. Identifies photons and charged particles. Has two types of detectors: Lead scintillator (PbSc) and lead glass (PbGl)
Muon Arm Detectors	
Muon Tracker (MuTr)	Measures the position and momentum of muon particles
Muon Identifier (MuID)	Identifies muon particles
Event Characterization Detectors	
Beam-Beam Counters (BBC)	Measures collision location and centrality. Starts the stopwatch for an event.
Zero Degree Calorimeters (ZDC)	Measures collision location and centrality.
Forward Calorimeters (FCal)	For deuteron+Au collisions, it can measure surviving neutrons and protons from the original deuteron.
Multiplicity Vertex Detector (MVD)	Measures collision location and charged particle distributions.
Heavy Metal Detector	
PHENIX Magnets	Bends charged particles so that their charge and momentum can be measured in both the central arm and the muon arm detectors.

Table 3.1: PHENIX detector overview

The primary goal of PHENIX is to discover and study a new state of matter called the Quark-Gluon Plasma (QGP). This form of matter was predicted from perturbative QCD calculations to exist when quarks and gluons are not bound inside of nucleons. Our Universe is thought to have been in this state for a very short time after it's birth. There is still no real consensus in physics, what we consider as the QGP, and if we have already seen it or not. The situation is a little bit similar to that of Columbus, who thought to have found India, but it took decades until

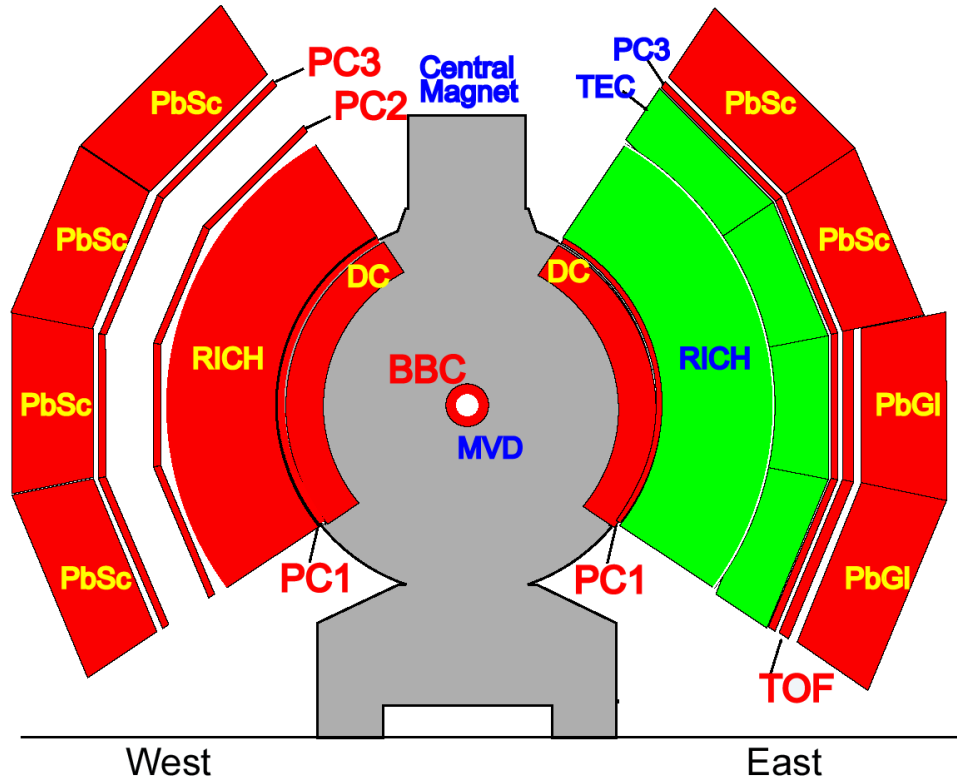
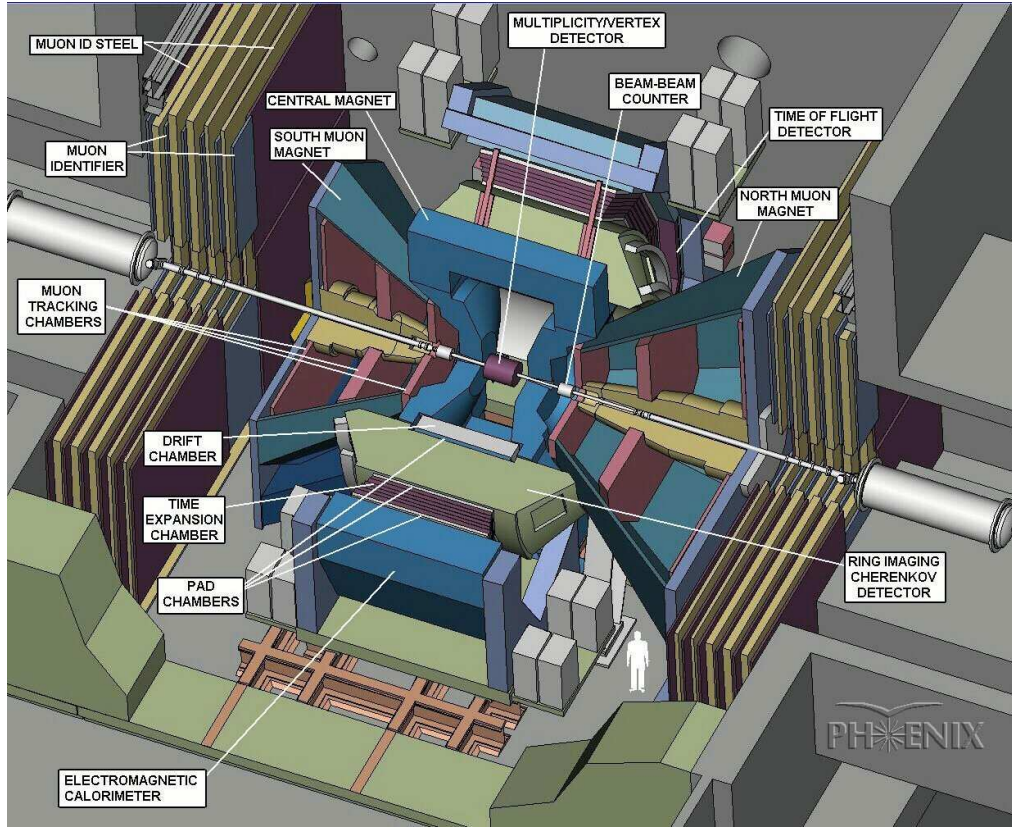


Figure 3.2: Detector arrangement in PHENIX during Run 3

it was clear where his ships dropped the anchors [4].

Now, the science mission of PHENIX can be summarized as follows:

- Search for a new state of matter called the Quark-Gluon Plasma, which is believed to be the state of matter existing in the universe shortly after the Big Bang. If it is found, then measure its properties.
- Study matter under extreme conditions of temperature and pressure.
- Study the most basic building blocks of nature like quarks and gluons, and the forces that govern them.

Some important results of PHENIX are the following:

There appears to be suppression of particles with a high transverse momentum – the momentum component perpendicular to the beam axis – in Au+Au collisions [5]. PHENIX observes that there are fewer particles with a high transverse momentum than what is expected from measurements of simpler proton collisions. This effect is referred to as jet suppression, since the majority of these particles are products of a phenomenon called jets, high energy and high transverse momentum particles. Jet suppression was predicted to occur if the QGP is formed, because of the energy loss of partons in the dense and hot matter.

There does not appear to be suppression of particles with a high transverse momentum in d+Au (deuteron+gold) collisions [6]. In these collisions, due to the small size of the deuteron, QGP can be formed only a very small region. This observation confirms that the suppression seen in Au+Au collisions is most likely due to the influence of a hot, dense and strongly interacting matter being produced, such as a Quark-Gluon Plasma.

PHENIX is unique at RHIC in that it can identify individual electrons coming from the collision, many of which are the result of decays of heavier particles within the collision. PHENIX measures a number of electrons that is above the expected background [7]. The excess electrons are likely coming from decays of special particles with heavy charm quarks in them. Further study of these charmed particles will help us better understand if the Quark-Gluon Plasma has been formed.

PHENIX has measured the fluctuations in the charge and average transverse momentum of each collision, because during a phase transition, it is typical to see fluctuations in some properties of the system. Thus far, PHENIX reports no large charge fluctuations that might be seen if there is a phase transition from a Quark-Gluon Plasma [8]. PHENIX reports that there are excess fluctuations in transverse momentum, but they appear due to the presence of particles from jets [9]. The behavior of the fluctuations is consistent with the jet suppression phenomenon mentioned previously. Recent lattice calculations indicate, that the QGP may be formed in a cross-over like transition, so we do not have to see signs of a phase-transition necessarily, but these features need further investigation.

PHENIX observes high particle flow, which is expected when heavy ions collide [10]. However, those high transverse momentum particles surprise again, and show a flow effect that is not yet understood.

Finally, here are some questions which need to be answered by PHENIX in the future:

- Are the jets really disappearing? Do they really look different than what has been seen before in collisions of protons? If the jets are disappearing, where does all of the energy go?
- Are J/Ψ particles disappearing? Do they decay differently than expected? Data taken in 2004 should be able to answer this question.
- Can we see photons radiating directly from a Quark-Gluon Plasma? PHENIX has a preliminary measurement that confirms the presence of these direct photons. Data taken in 2004 should improve this measurement.
- Are the masses of the particles moving due to physical effects in a Quark-Gluon Plasma?

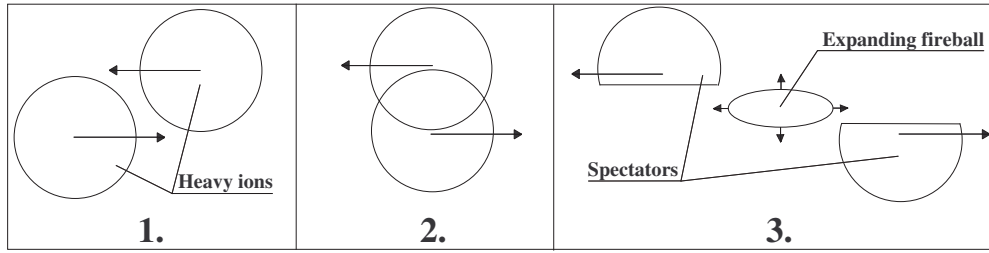


Figure 3.3: Sketch of a high energy heavy ion collision

In the first part, the two heavy ions are nearing to each other. Lorentz-contraction is neglected here to have a more clear picture. After that, they collide. From the region where they overlap arises an expanding fireball of new particles, and the other parts, the so called spectators continue their way. From these parts, protons and neutrons evaporate.

- Do the particles decay in the same way as has been measured in simpler particle collisions?

Has PHENIX found the Quark-Gluon Plasma? It is too early to say for sure, but the observation of jet suppression and the very large amount of flow are very promising, while there are lots of unanswered questions. The optimistic point of view says, that we see already a few signs of QGP, so we may have found it. From the pessimistic point of view one could think, that we have some signals, which should not appear if the QGP was formed. A realistic point of view is, that we have found a hot, dense matter, and it's properties have to be investigated to decide, if it is the expected QGP or something else.

We would like to study more data in order to answer all these questions.

3.4 The zero degree calorimeter

The Zero Degree Calorimeter (ZDC) is a neutron detector, which is placed in the line where the two beams of RHIC cross each other (the interaction region). It is present at all four experiment of the Relativistic Heavy Ion Collider and may be considered to be part of RHIC instrumentation also.

The ZDC was designed as a detector for luminosity measurement and monitoring, event geometry characterization. In heavy ion collisions it is used for centrality selection (with the Beam Beam Counters), to study Coulomb-dissociation, nuclear fragmentation processes, investigation of γ - γ collisions, etc ... In d+Au runs the ZDC (together with the Forward Hadron Calorimeter) is used for $p(d)+Au \rightarrow n+X$, $n(d)+Au \rightarrow p+X$, $d+Au \rightarrow X$ event classification [11, 12, 13].

My task at the ZDC was to develop the online monitoring software for this detector component. The online monitoring is a program that has to produce plots from the data that is currently taken.

3.4.1 Goals of the calorimeter

It measures the energy of the neutrons that are evaporated from the spectators of the collision. These neutrons do not take part in the collision, and if they decouple from the protons, the magnetic field will not guide them to stay in the beampipe, and go straight forward into the zero degree calorimeter.

The energy of these neutrons can be computed from the center of mass energy ($\sqrt{s_{NN}}$). If we use the center of mass frame, where $\mathbf{p}_1 = -\mathbf{p}_2 = \mathbf{p}$:

$$s_{NN} = (p_1 + p_2)^2 = 2m^2 + 2(|\mathbf{p}| + E)^2 = 4E^2 \quad (3.1)$$

So, by measuring the energy of the evaporated neutrons, we access the fluctuations of the center of mass energy.

channel	number
south analog sum	0
south slabs	1-3
north analog sum	4
north slabs	5-7

Table 3.2: ZDC channels

There are eight ZDC channels, six for the south and north slabs, and two more for the analog sums of these channels.

Another purpose of the ZDC is to measure the vertex position, the position, where the collision happened. This is possible, because the evaporated neutrons start their flight with the spectator part of the nucleus at the same time from the collision point. If in one direction, the neutrons reach the ZDC earlier, the vertex was nearer to this side. This is possible, because we read out not only energy, but timing information, too. The velocity of the neutrons equals within error the speed of light.

Expressed with a formula:

$$z_{vertex} = (t_{south} - t_{north})c \quad (3.2)$$

3.4.2 Construction of the ZDC

The Zero Degree Calorimeter is a Cherenkov light sampling calorimeter, and there is one at both ends of the interaction region.

Mechanically, each arm of the ZDC is subdivided into 3 identical modules with 2 interaction length each. The active medium is made from clear PMMA fibers interleaved with Tungsten absorber plates. This sandwich structure is tilted at 45 degree to the beam to align the optical fibers with the Cherenkov angle of forward particles in the shower. The energy resolution of the ZDC for 100 GeV neutrons is 21%. Time resolution is around 120 ps for 100 GeV neutrons which may be translated into a vertex position resolution of around 2.5cm.

The three analog signals coming from the slabs are digitalized after some amplifying, as well as their analog sum, and a timing signal for each channel. This information is then stored and analyzed by computers.

The energy is calibrated with an LED, which pulses with a low frequency. We take some events where there was no collision only an LED pulse, and we know the energy of the LED signal, and through this, energy of the detected particles can be calibrated. We monitor the LED energy too.

3.5 The Shower Max Detector

The Shower Maximum Detector (SMD) is unique to the PHENIX ZDC's. It is useful for a study of transverse momentum distribution of beam fragmentation products, beam steering and beam profile studies due to beam divergence.

SMD is an X-Y scintillator strip detector inserted between 1st and 2nd ZDC modules. This location corresponds (approximately) to hadronic shower maximum position. The horizontal x coordinate is sampled by 7 scintillator strips of 15 mm width each, while the vertical y coordinate is sampled by 8 strips of 20 mm width each, tilted by 45 degrees. The active area covered by SMD is 105 mm \times 110 mm. The SMD position resolution depends on energy deposited in the scintillator and varies from around 10 mm at small number of charged particles crossing the SMD to values smaller than 3 mm when number of particles exceed 100. For comparison, the spread of neutrons due to of nucleon Fermi motion is about 2.2 cm at 100 GeV.

As mentioned before, with the SMD we can measure the beam position, if we look at the energy distribution of the shower in the vertical and horizontal strips. I measure the beam position on the following way then:

channel	number
south horizontal strips	8-15
south vertical strips	16-22
south analog sum	23
north horizontal strips	24-31
north vertical strips	32-38
north analog sum	39

Table 3.3: SMD channels

There are 32 SMD channels, seven and eight for the vertical and horizontal strips respectively, and two more for the analog sums.

$$x = \sum_{i=1}^7 \left(\frac{E_i x_i}{\sum E_i} - \frac{x_i}{7} \right), \quad (3.3)$$

$$y = \sum_{i=1}^8 \left(\frac{E_i y_i}{\sum E_i} - \frac{y_i}{8} \right), \quad (3.4)$$

where E_i is the energy deposited in the i th slab and x_i is its position. Figure 3.4 shows a possible energy distribution. In the formulas the average position of the slabs is subtracted to have the $(x, y) = 0$ position at the physical center of the SMD.

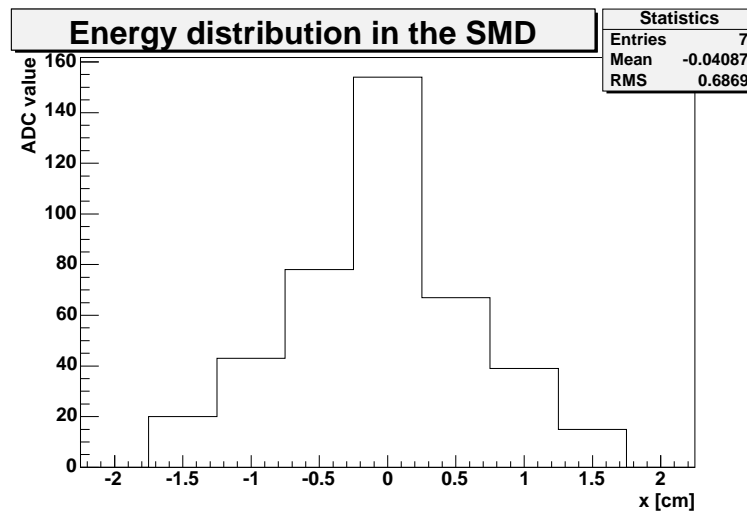


Figure 3.4: SMD energy distribution

In this figure, we see the energy distribution in the horizontal slabs of the north SMD. If we take the average of the positions weighted with the deposited energy, we get the mean position.

Now, we have the beam energy and position at both the north and south side. It is very important to monitor these to see immediately, if there is a change in these basic quantities.

3.6 The online monitoring

The online monitoring is a software system, that has the purpose to monitor the data that is taken at the moment. For every detector-component there has to be an online monitor program,

because if there won't be one, we might not notice that that particular component is not working properly, and the data from that detector is unusable.

In this section, I show some plots of the ZDC and SMD online monitor. The code is available in ref. [1].

3.6.1 Beam energy monitoring

We have a monitor for south and north beam energy. The upper panels in figures 3.5 and 3.6 show the energy distribution in the north and south ZDC. The red dashed lines show the allowed region for the maximum of the curve. This is around 1700-1900 GeV for gold beam, and at 100 GeV for deuterium beam. In the latter case, we can have only one evaporated neutron, so the energy should be around 100 GeV, and in the former case, we saw, that the most likely number of evaporated neutrons is 17-19, so this energy region should be maintained.

3.6.2 Vertex position monitoring

We have a monitor for the south and north beam position. The left middle panel in figures 3.5 and 3.6 show the vertex position, and the middle right is the same just for the events where the BBC level 1 trigger fired. The latter, corrected distribution has a gaussian shape, because if we have an event, where BBC level 1 trigger did not fire, it is very likely, that this was a fake event. Some timing correction is still missing in figure 3.6, as the maximum is very far from zero. This correction was already made for the Au+Au run, so the vertex position is in figure 3.5 near to zero.

3.6.3 Beam position monitoring

There is a monitor for the vertex position. The last two plots in figures 3.5 and 3.6 show the north and south SMD position distribution. Scattering is bigger in the deuteron case, the hits for the gold beam are relatively more concentrated. In figure 3.5 there is a circle drawn around the middle, and the maximum of the distribution should be in this circle.

3.6.4 Main expert plots

If there is something strange in the main monitors, it is more easy to detect the root of the problem, if we have already some special plots which show some useful information. Shifters do not have to understand and monitor these plots, but they are useful for experts.

Main expert plots are in figures 3.7 and 3.8. These show in the first line the separate beam centroid distributions in the SMDs. After that, there are plots to see correlations between position and energy. This is very useful, because if a little peak appears in energy, we could possibly see, from which direction this 'noise' comes. The other four plots show the raw ADC distributions for the sum of the SMD channels.

3.6.5 LED signal monitoring

As we saw already, the energy calibration in ZDC is done via an LED signal. There is a plot for the LED energy values in figure 3.9, where we can see, if the gain of some channels went bad for example, or somehow the energy of the LEDs changed somehow. This would cause the LED energy plots not to be constant. There are green lines on these plots, which show the values of the energy seen a few days ago. The values at the first ZDC slab on the north side deviate from this green line, because gain for that channel was changed in the meantime.

The timing is monitored as we see in figure 3.10, this is more constant.

History of LED values for every channel is stored in a database and monitored. Some of these plots are shown in figure 3.11. Values on the horizontal axis are in units of 10^4 seconds. There were in the monitored interval of a few weeks four changes.

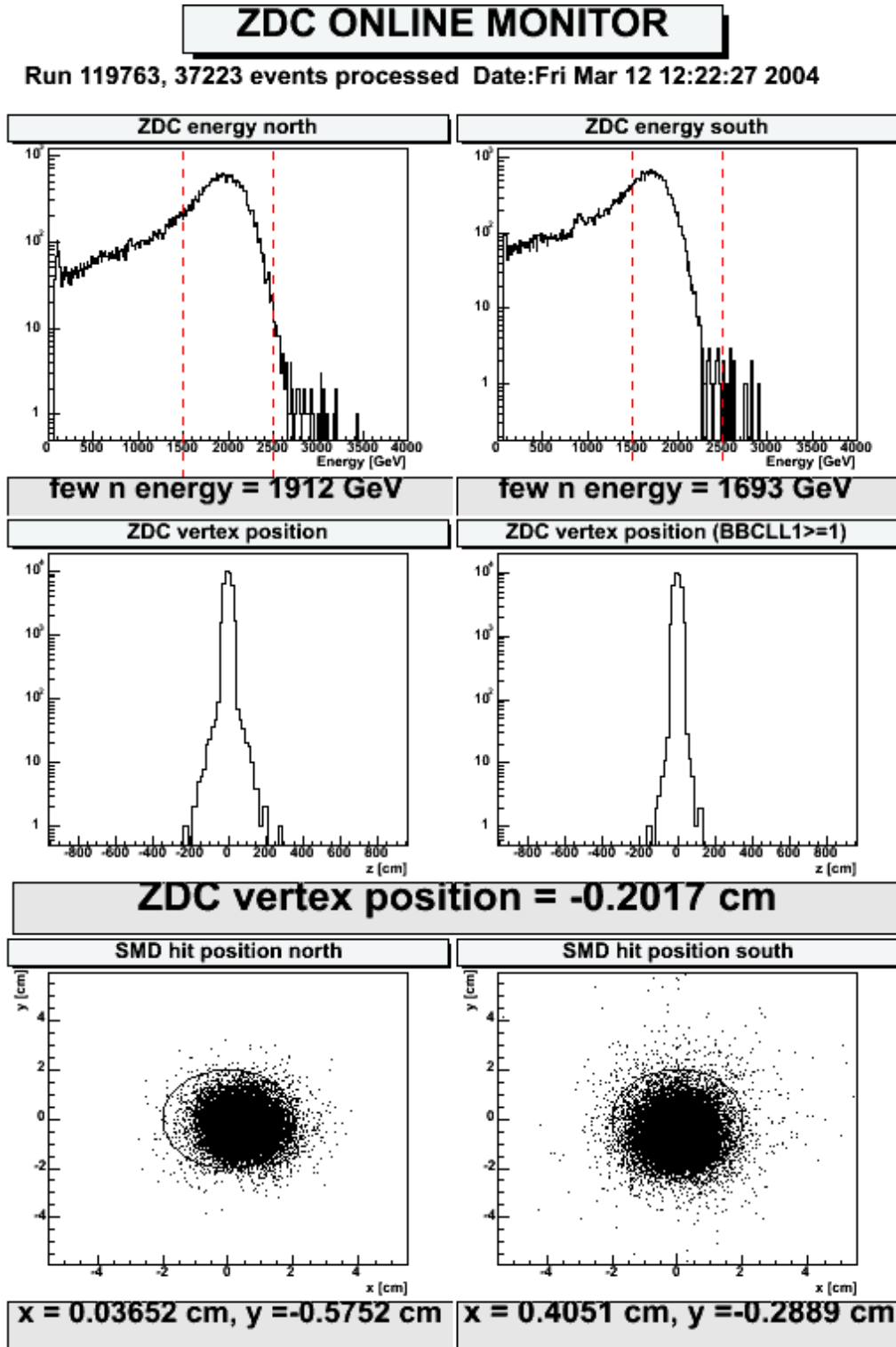


Figure 3.5: ZDC main online monitor in a Au+Au run

This figure shows the ZDC online monitor in a Au+Au run. In the first row, we see the energy distributions in the north and south side calorimeters. The plots in the second row show the vertex position distribution, on the left hand side with a cut made with help of the BBC. In the last row, we see the transverse position distribution measured via the SMD. All plots show values within the normal ranges.

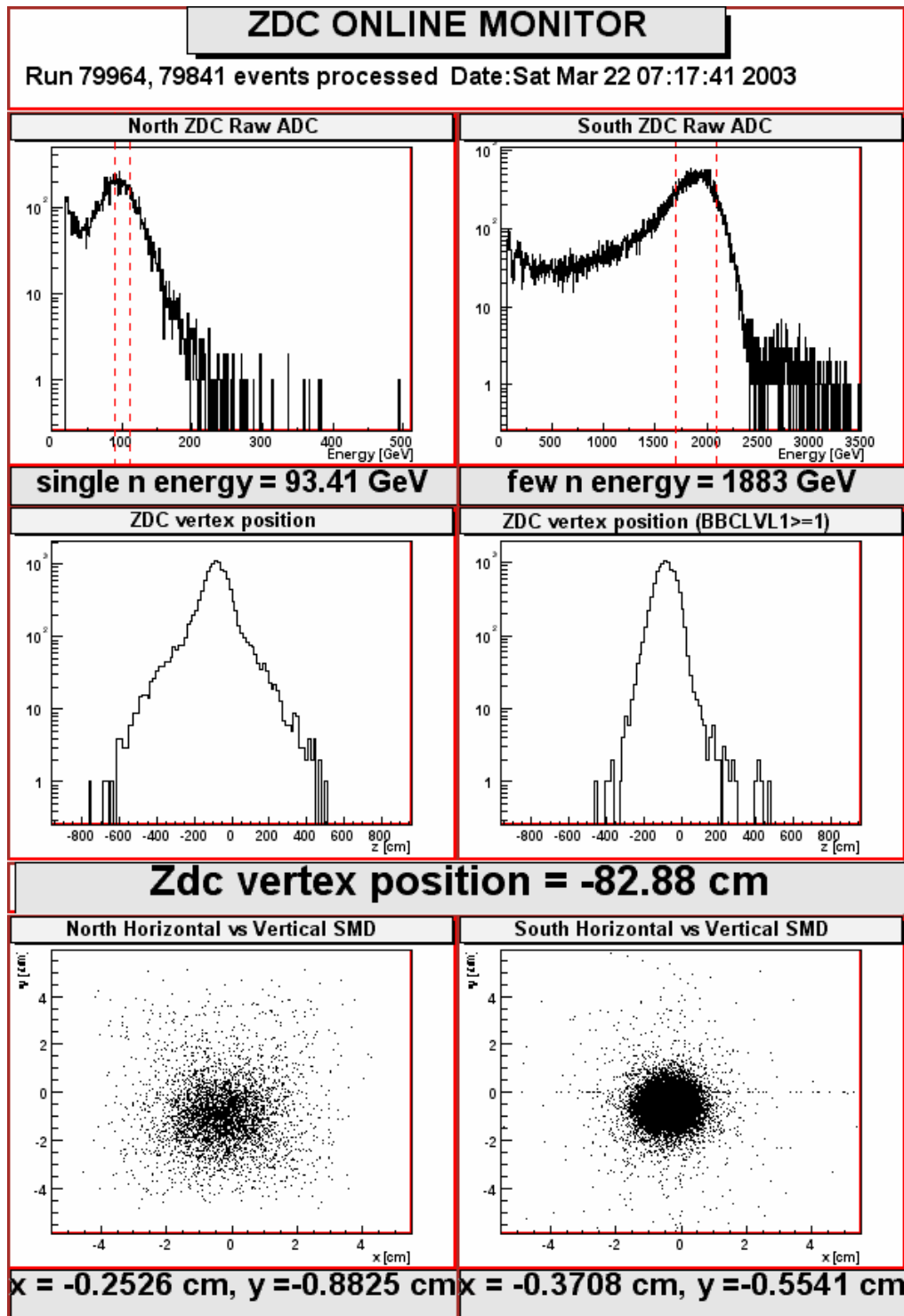


Figure 3.6: ZDC main online monitor in a d+Au run

The plots shown in this figure are similarly arranged as in figure 3.5. The nominal value of the energy maximum on the deuteron side is smaller here, and the measured value is in the allowed $100 \text{ GeV} \pm 10 \text{ GeV}$ range. An other feature is, that the vertex distribution was broader here and had a maximum shifted towards the south side. Later, the ZDC timing was corrected and then the maximum moved to zero, as in figure 3.5.

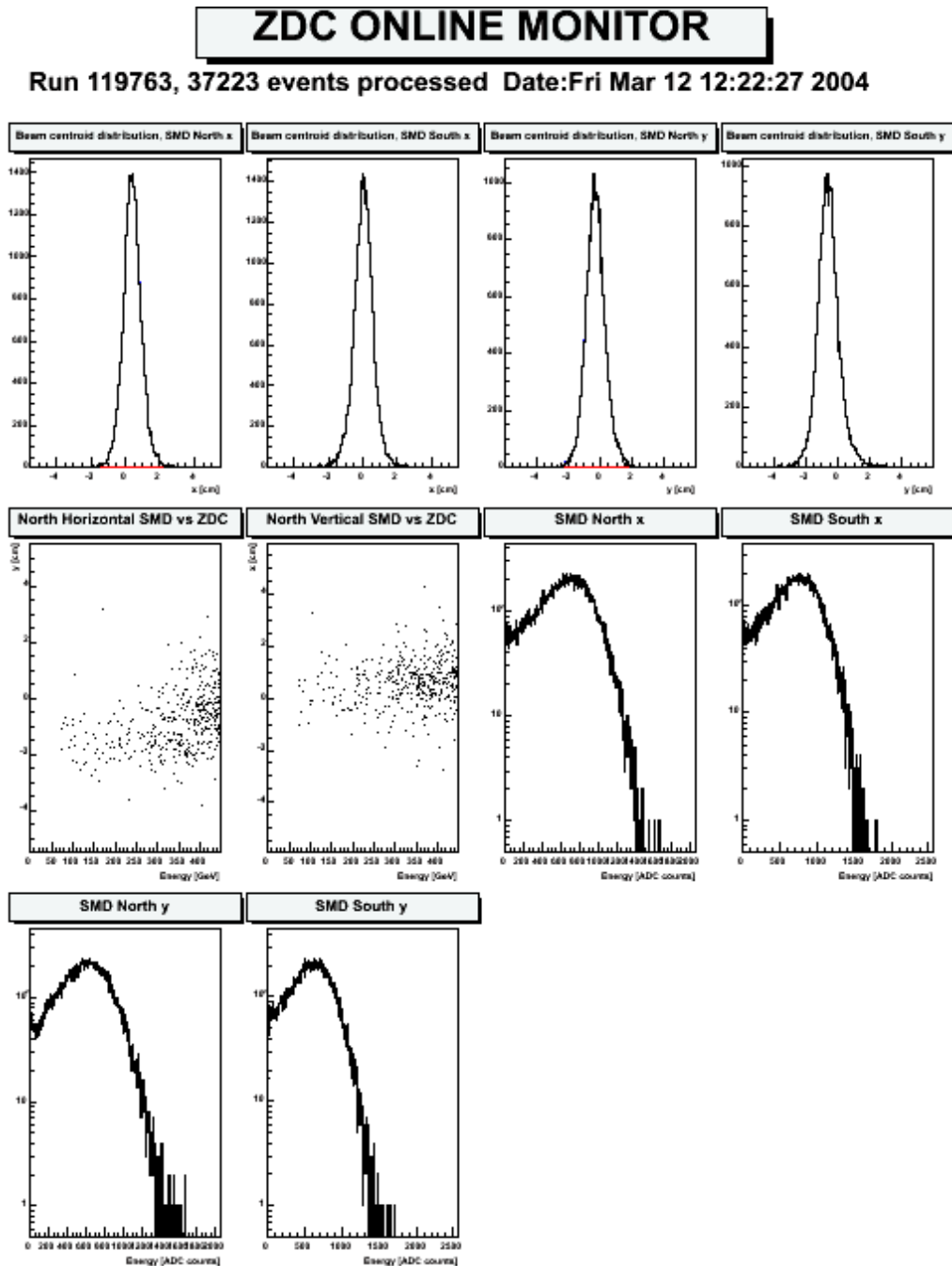


Figure 3.7: Expert plots in a Au+Au run

The first four plots show the beam position distribution in the four (south and north, horizontal and vertical) SMD sets. The first two plots in the second row show the correlation between energy and position, while the in the last plots we see the distribution of the raw ADC signal from the SMDs.

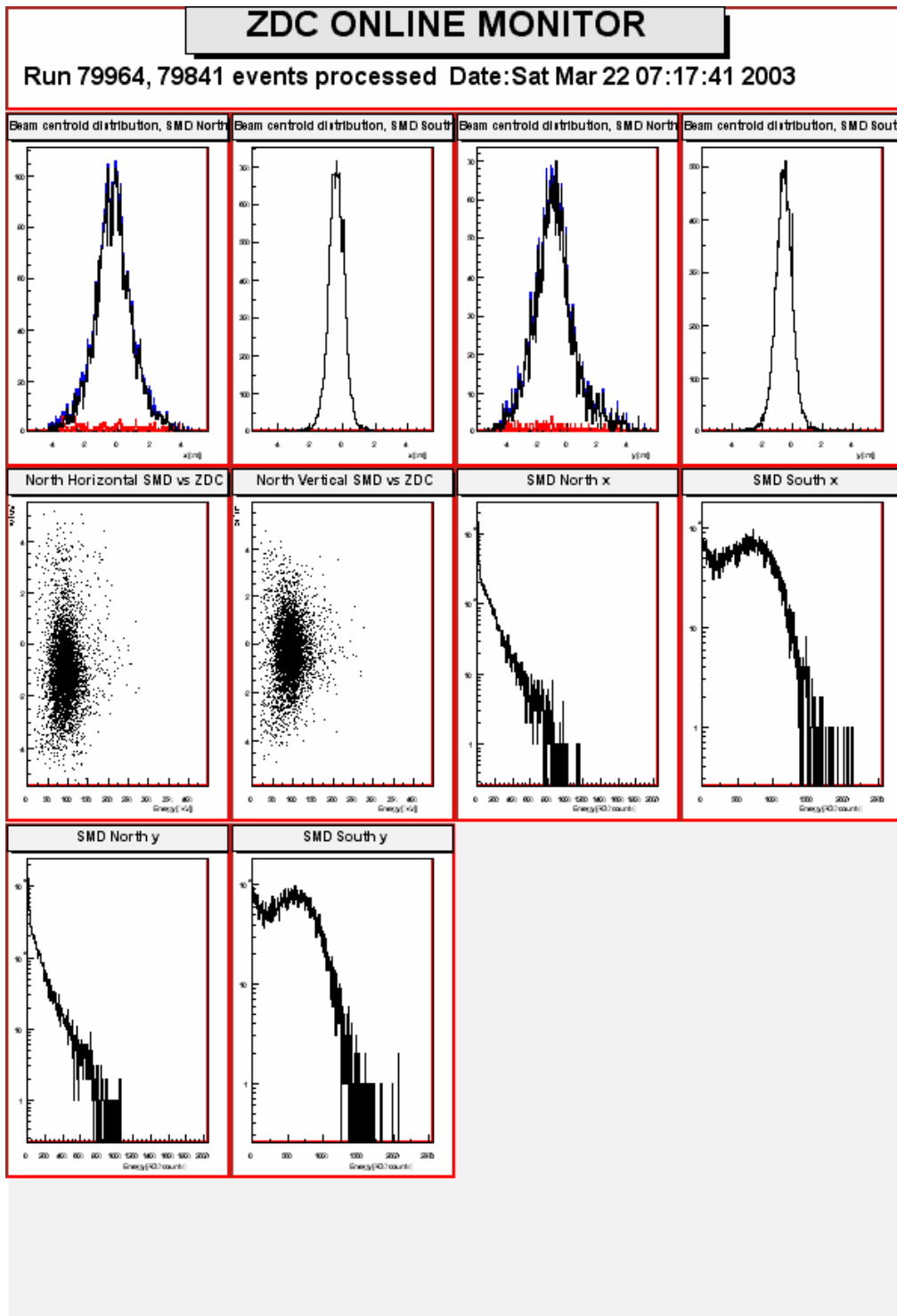


Figure 3.8: Expert plots in a d+Au run

The plots shown here are the same as in figure 3.7, just in a d+Au run. The south, Au side plots are very similar, but on the north side the energy is smaller, and the scale of the correlation plots was changed also.

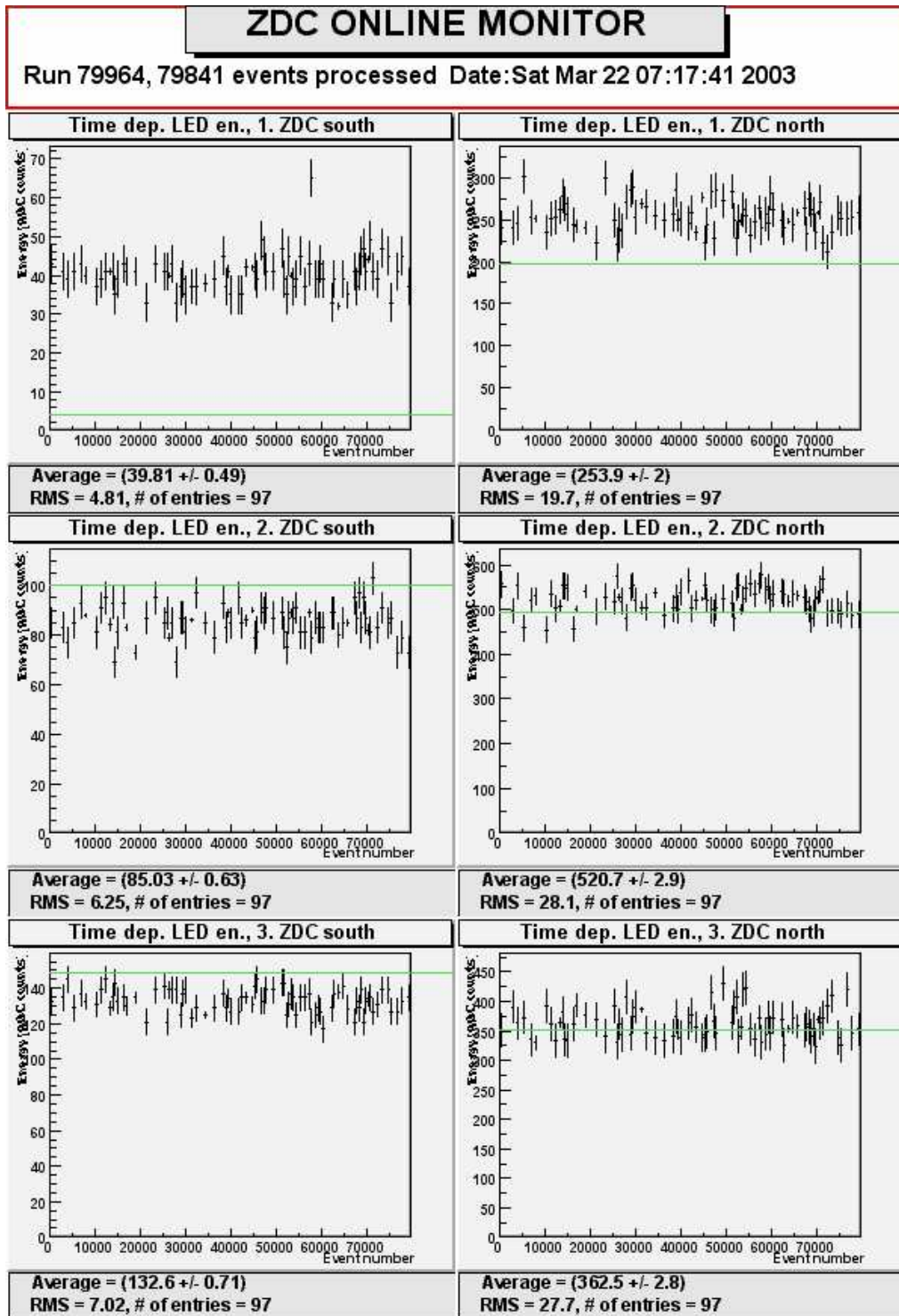


Figure 3.9: LED energy values versus event number

In this set of plots we see the time (event number) dependence of the LED energy. The south side is shown on the right, the north side on the left. The individual rows correspond to the deposited energy measured in the first, second and third ZDC slab, respectively. Green lines represent the average values measured a few days formerly.

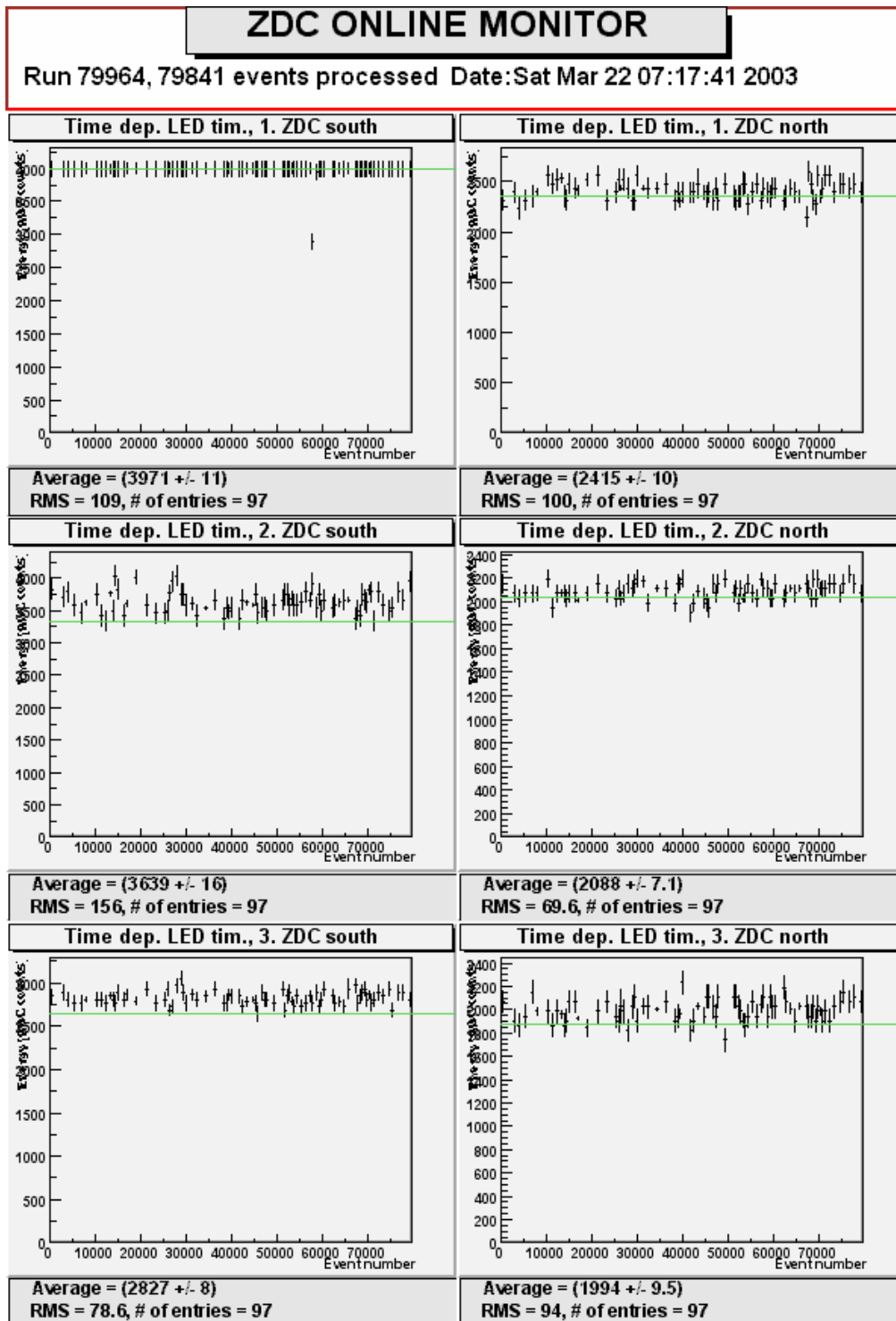


Figure 3.10: LED timing values versus event number

LED timing values are plotted here versus the event number. Arrangement of the plots is the same as in figure 3.9. There are acceptable random fluctuations, but in the first slab on the south side, all values are in the last bin. Because of this overflow, some corrections on the timing signal had to be made.

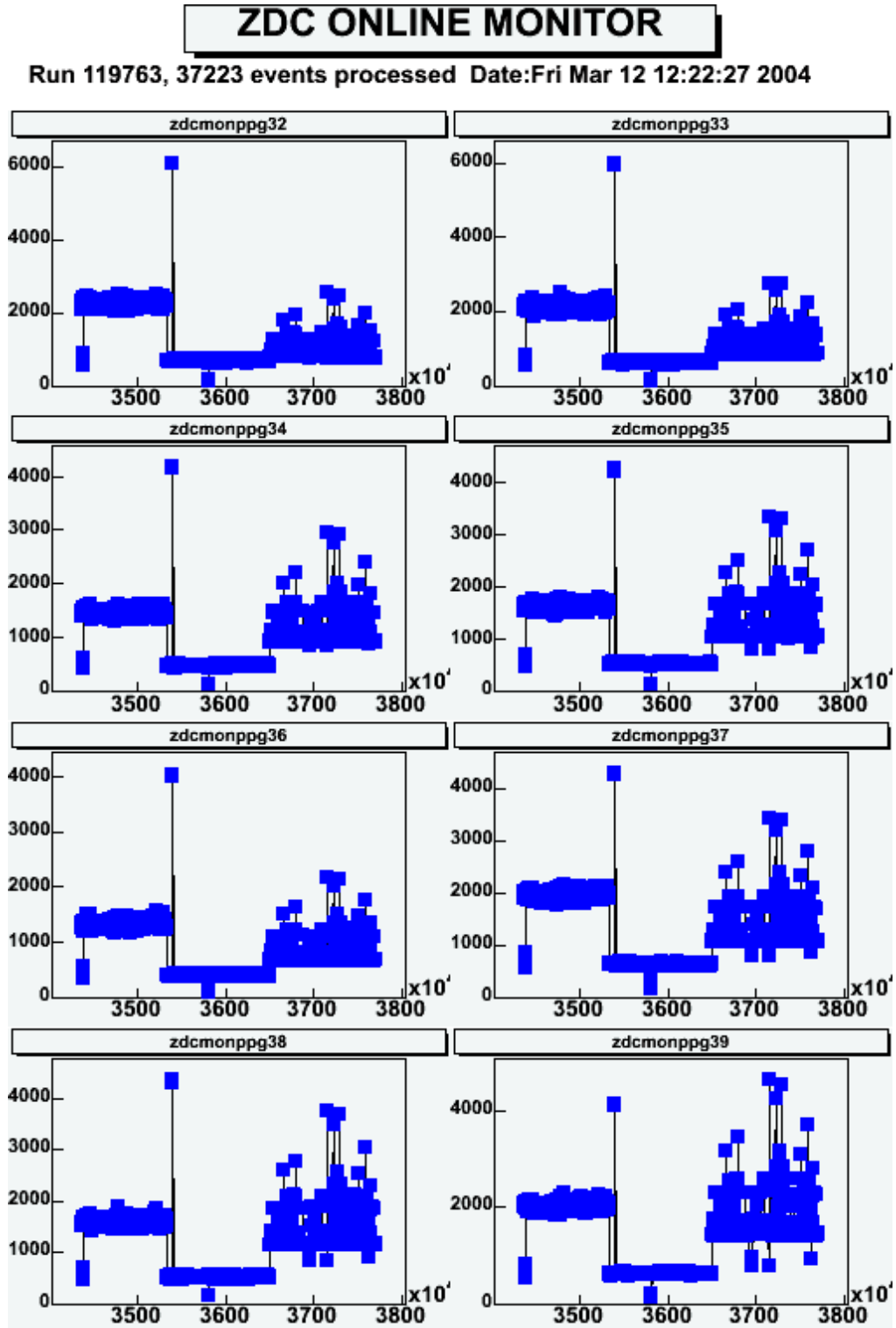


Figure 3.11: Expert plots in a Au+Au run

The average LED energy deposited in the north vertical SMD strips is plotted here versus the time of the run in which it was measured. Two significant changes are noticeable on all eight plots corresponding to the eight strips. Both of the shifts are due to a change in the high voltage setting in our detectors. The covered period of time plotted in these figures is around one and a half month.

3.6.6 Other expert plots

It is important to monitor the history of the main values that are measured by the ZDC, to keep track of changes. Because of this I included figure 3.12 in the online monitoring. On this figure, the first two lines we see the history of the four SMD positions. In the monitored time-interval, there were no big changes, we can just see, that in a short interval of around 80000 seconds we had no beam. The strong deviations on these plots are due to averaging problems. I average 1000 events and put their value to the database, but there can be a short period with lots of bad events, or if a run ends before the completion of 1000 events, averaging goes wrong.

We have two plots for the energy history, what we see here is a constant energy with rare bad values. The explanation for them could be the same as in the previous paragraph. Interesting is here furthermore the small scattering of the energy values.

The vertex position history seems to have a large scattering, but this just due to the lack of strong deviations and small scales. It is nearly constant in the monitored interval.

SMD position history is monitored inside of a run as well, these plots are in figure 3.13. The green lines are at hard-coded values and represent the value seen a few weeks ago. We see, that the south horizontal position did slightly change, the others are pretty constant. The error bars come from the averaging, which is made for 1000 events here also.

The raw ADC values of the SMD channels are included in the online monitoring also, the north channels are to see in figure 3.13. The smaller histogram is made with a cut in the ZDC energy (eg. here in Au+Au, $E_{ZDC} < 200MeV$), and it helps testing that cut. If we see, that these small histograms start to increase, the cut limit has to be revised. Furthermore, the location of the peaks in the larger histograms helps to determine gain factors in SMD channels.

It is important to determine gain factors in the ZDC channels, too. With the plots in figure 3.15 we constantly check, if have correct values for this. If the gains are correct, the ratio deposited energies in the first and second plus third slab should be equal for north and south side, due to same geometry. The bend in the curve is still unexplained, but could be due to different acceptance of the detectors at different energies.

3.7 The vernier scan

Vernier scans are done from time to time in RHIC to be able to calibrate the SMDs. In a vernier scan, the beam position is changed by the main control room stepwise, and we look at our position values, if they give back the motion. We get the positions from the control room as a function of time, and then compare to the monitored values. This is shown in figure 3.16.

What we have learned from the plots, is that there is a small synchronization problem still, and the calibration has to be improved, too, but the beam movement is well monitored.

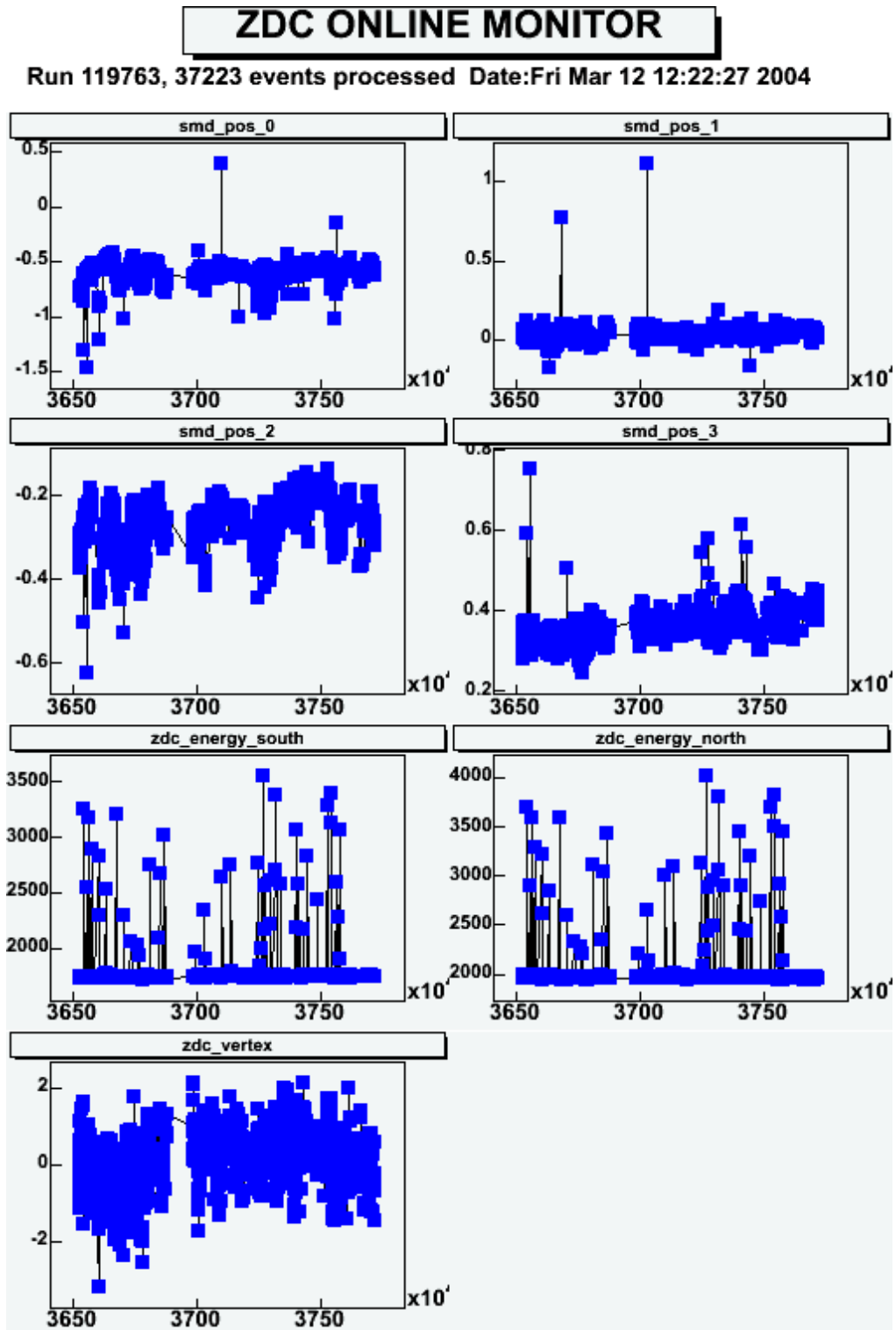


Figure 3.12: Expert plots in a Au+Au run

In the first four figures the history of the position measured in the SMDs is plotted here. After that the average deposited energy in the south and north ZDC is shown. There is a clearly visible constant line at around 2000 GeV, the higher values are due to a numeric problem in the averaging method. The last plot shows the vertex position history. The covered period of time plotted in these figures is around two weeks.

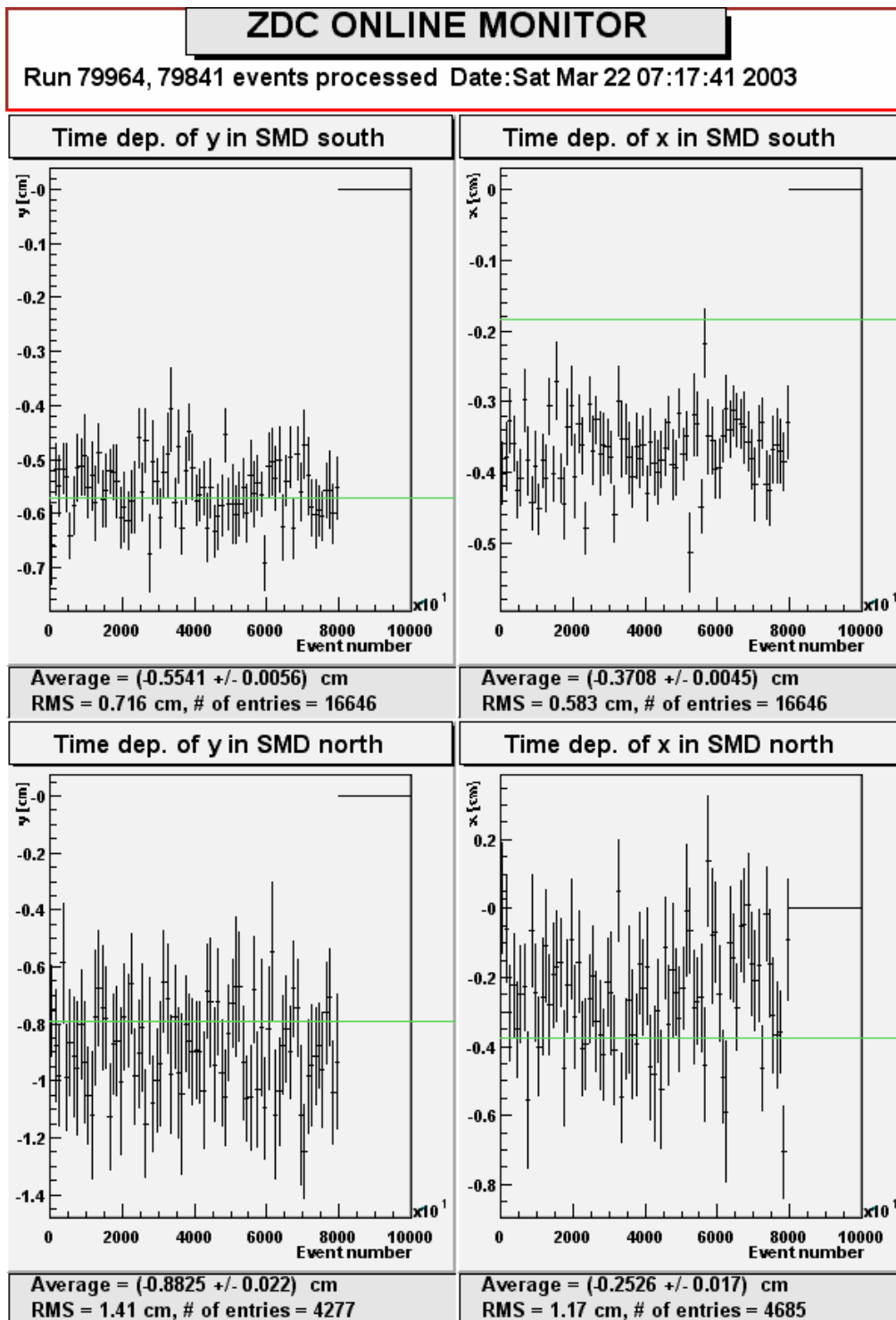


Figure 3.13: SMD position versus event number

Time – event number – dependence of the beam position is shown in these figures. There are large but acceptable random fluctuations in this run.

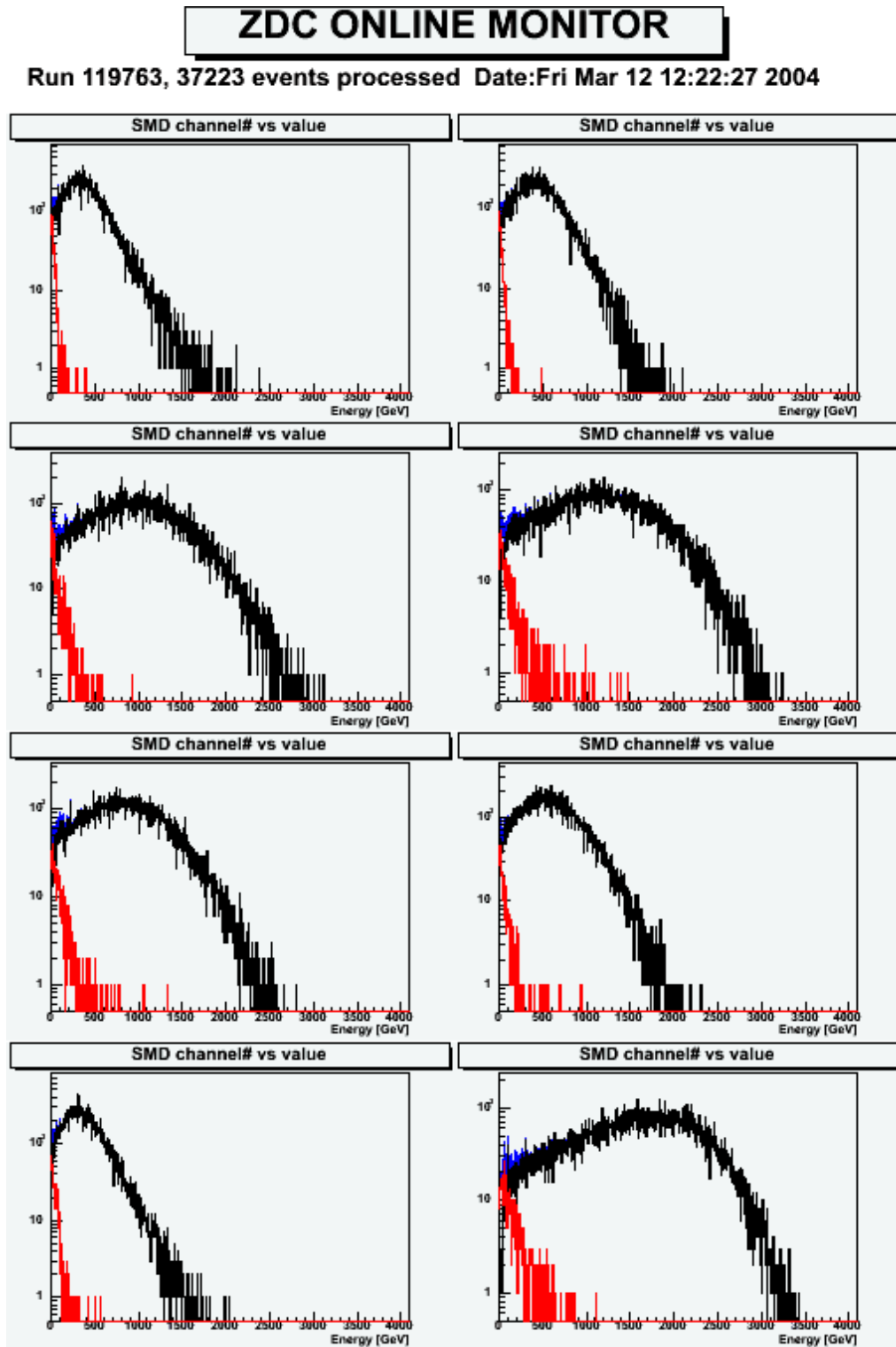


Figure 3.14: Raw ADC value distributions in the north vertical SMD

Distribution of the raw ADC signal coming from north vertical SMDs is shown here. The width of the distribution changes from plot to plot, due to different gains in different photomultipliers. Red curves show the ADC signal only for events with $E_{ZDC} < 200 \text{ MeV}$.

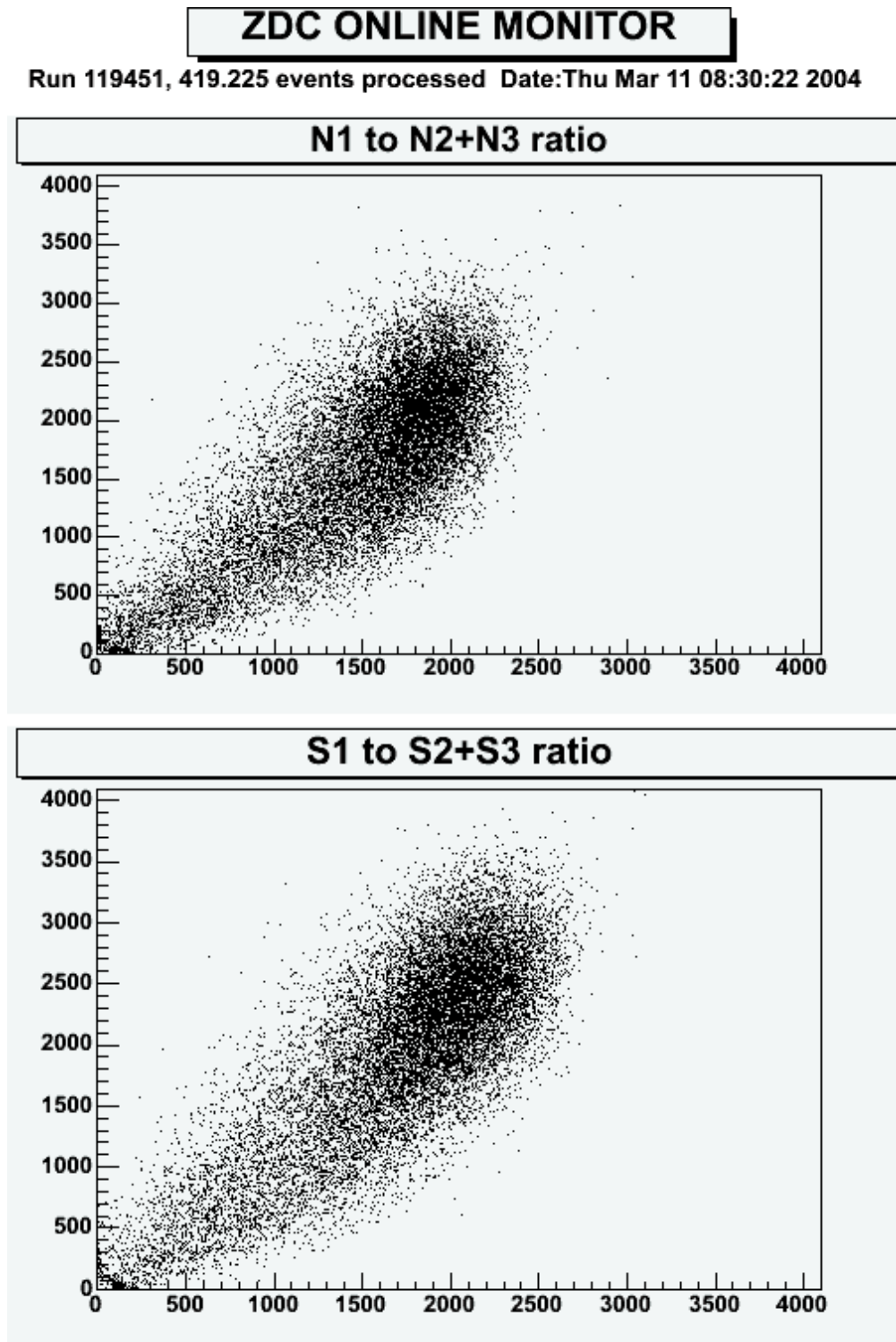


Figure 3.15: Expert plots in a Au+Au run

In the top panel, the correlation between the deposited energies in the first and the second plus third ZDC slab is plotted. The bottom panel shows the same correlation for the south side. The slope of the distributions should be the same for both sides, as it represents the ratio of the gain factors used in the individual ZDC slabs.

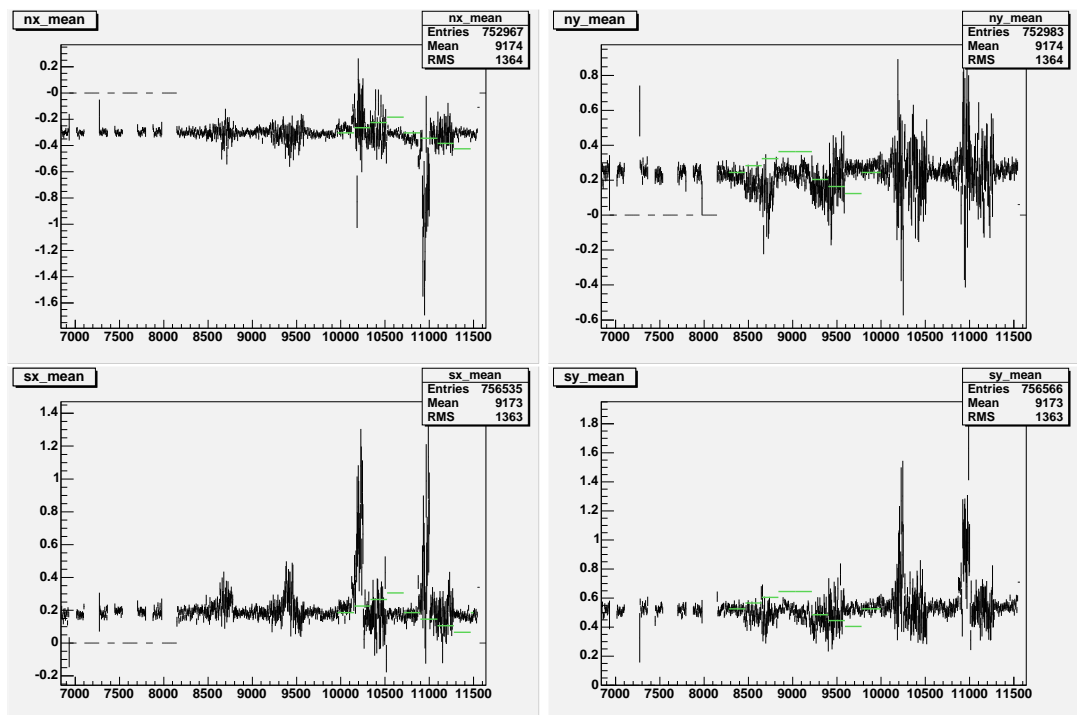


Figure 3.16: Vernier scan plots

Plots of a Vernier scan. Green straight lines show the desired position, while the values with error bars are the monitored positions. The moving is clearly visible while it does not reproduce the beam positions given by the main control room. Further corrections are necessary and the calibration of the detector has to be improved.

Chapter 4

Data analysis

*The answer to the great question . . . of life,
the universe and everything . . . is forty-two.*

THE HITCH HIKER'S GUIDE TO THE GALAXY, DOUGLAS ADAMS

4.1 Experimental definitions

4.1.1 The two-particle correlation function

The two-particle correlation function measures the correlations between particle pairs. Its definition is:

$$C_2(p_1, p_2) = \frac{N_2(p_1, p_2)}{N_1(p_1)N_1(p_2)}, \quad (4.1)$$

where $N_2(p_1, p_2)$ is the two-particle invariant momentum distribution, and $N_1(p)$ is the one-particle spectrum

$$N_1(p) = \frac{E}{\sigma_{tot}} \frac{d\sigma}{dp}, \quad (4.2)$$

where σ_{tot} is the total inelastic cross-section.

The correlation function C_2 can be measured as a function of the two momenta p_1 and p_2 , but if there is not enough statistics, we can project it to one dimension: we measure it as a function of

$$Q_{12} = \sqrt{-(p_1 - p_2)^2}. \quad (4.3)$$

The experimental definition is, when projected to one dimension:

$$C_2(Q_{12}) = \frac{A(Q_{12})}{B(Q_{12})} \quad (4.4)$$

Experimentally, the two particle correlation function is the ratio of the actual and mixed or background pair distributions. The actual pair distribution is

$$A(Q_{12}) = \int d^4p_1 d^4p_2 \tilde{\delta}_{\Delta Q}(Q_{12} - Q_{12}(p_1, p_2)) N_2(p_1, p_2) \quad (4.5)$$

and the mixed or background pair distribution is

$$B(Q_{12}) = \int d^4p_1 d^4p_2 \tilde{\delta}_{\Delta Q}(Q_{12} - Q_{12}(p_1, p_2)) N_1(p_1)N_1(p_2), \quad (4.6)$$

where the $\tilde{\delta}_{\Delta Q}(Q_{12} - Q_{12}(p_1, p_2))$ function is similar to the Kronecker-delta, as it gives one, if the invariant momentum of the pair is in a ΔQ wide bin around a given Q_{12} , and zero otherwise. can be defined via the

$$\Theta(x) = 0 \text{ if } x < 0 \text{ else } 1 \quad (4.7)$$

function as

$$\tilde{\delta}_{\Delta Q}(Q) = \Theta\left(\frac{\Delta Q}{2} + Q\right) \Theta\left(\frac{\Delta Q}{2} - Q\right). \quad (4.8)$$

The momentum distributions can be measured, so we have to integrate them in order to get the two-particle correlation function. But if we integrate over the whole momentum-space, we waste a lot of time as in momentum-space cells there are no pairs. Fortunately, the pair distributions can be computed on a more reasonable way from the data. First, the actual pair distribution can be measured as

$$A(Q_{12}) = \sum_{\text{events}} \left(\sum_{\text{pairs}} \tilde{\delta}_{\Delta Q}(Q_{12} - Q_{12}(p_1, p_2)) \right) \quad (4.9)$$

Here, the first sum is on the selected events, and the second on the detected particles in an event. This way, we get a histogram, which is filled at one Q_{12} value everytime there is a particle pair in an event with this Q_{12} .

Now we have to sum only on the momentum-pairs, where we have a real particle pair, and in eq. 4.5 we summed (or integrated) on all momentum-pairs.

The mixed distribution can be measured similarly, but here we sum on every particle pair, not just on pairs from the same event. This will give a background distribution:

$$B(Q_{12}) = \sum_{\text{mixed pairs}} \tilde{\delta}_{\Delta Q}(Q_{12} - Q_{12}(p_1, p_2)) \quad (4.10)$$

Furthermore, we can pre-normalize the correlation function, as we multiply it by the ratio of the integral of the distributions:

$$C_2(Q_{12}) = \frac{A(Q_{12})}{B(Q_{12})} \times \frac{\int B}{\int A} \quad (4.11)$$

This way, we won't have to worry about the different number of actual and mixed pairs. Also, we neglect long range correlations here.

4.1.2 The three-particle correlation function

The theoretical definition is

$$C_3(p_1, p_2, p_3) = \frac{N_3(p_1, p_2, p_3)}{N_1(p_1)N_1(p_2)N_1(p_3)} \quad (4.12)$$

so it is defined through the three- and one-particle invariant momentum distribution.

Again, we have to project it to one dimension with

$$Q_3 = \sqrt{-(p_1 - p_2)^2 - (p_2 - p_3)^2 - (p_3 - p_1)^2} \quad (4.13)$$

Then, the three-particle correlation function can be measured on the following way, similarly to the two-particle case:

$$C_3(Q_3) = \frac{A(Q_3)}{B(Q_3)} \quad (4.14)$$

here, the normalization can be determined from the fit, or the

$$C(Q_3) = \frac{A(Q_3)}{B(Q_3)} \times \frac{\int B}{\int A} \quad (4.15)$$

definition can be used.

In my calculations, I used the latter definition.

The actual triplet distribution is

$$A(Q_3) = \int d^4 p_1 d^4 p_2 d^4 p_3 \tilde{\delta}_{\Delta Q}(Q_3 - Q_3(p_1, p_2, p_3)) N_3(p_1, p_2, p_3) \quad (4.16)$$

and the mixed triplet distribution is

$$B(Q_3) = \int d^4 p_1 d^4 p_2 d^4 p_3 \tilde{\delta}_{\Delta Q}(Q_3 - Q_3(p_1, p_2, p_3)) N_1(p_1)N_1(p_2)N_3(p_3) \quad (4.17)$$

Here we use the one method described in the previous subsection:

$$A(Q_3) = \sum_{\text{events}} \left(\sum_{\text{triplets}} \tilde{\delta}_{\Delta Q}(Q_3 - Q_3(p_1, p_2, p_3)) \right) \quad (4.18)$$

and

$$B(Q_3) = \sum_{\text{mixed triplets}} \tilde{\delta}_{\Delta Q}(Q_3 - Q_3(p_1, p_2, p_3)) \quad (4.19)$$

4.2 Goals of measuring the correlation functions

If we have the shape of the correlation function, we can fit it by a Gaussian function:

$$C(Q) = Ne^{-R^2Q^2}, \quad (4.20)$$

or the more general Edgeworth function:

$$C(Q) = N \left[1 + e^{-R^2Q^2} \left(1 + \frac{\kappa_3}{3!} H_3(\sqrt{2}RQ) + \frac{\kappa_4}{4!} H_4(\sqrt{2}RQ) + \dots \right) \right], \quad (4.21)$$

with the Hermite-polynomials

$$H_i = -e^{t^2/2} \frac{d^i}{dt^i} e^{-t^2/2} \quad (4.22)$$

Then, we can extrapolate their value at zero relative momenta. This is very useful, because then we can determine basic properties of the observed matter.

4.2.1 Partial coherence and core-halo picture

We defined the two- and three-particle correlation function by the following shape:

$$C_2(p_1, p_2) = \frac{N_2(p_1, p_2)}{N_1(p_1)N_1(p_2)} \quad (4.23)$$

$$C_3(p_1, p_2, p_3) = \frac{N_3(p_1, p_2, p_3)}{N_1(p_1)N_1(p_2)N_1(p_3)} \quad (4.24)$$

But our source can be described in the core-halo picture, where the source has two parts, a hydrodynamically evolving core and a halo of the decay products of the long-lived resonances [14]. This way we will have an N_c and an N_h for the particles which come from the core and the halo, respectively. Then, we define the fraction of the core as

$$f_c(p) = N_c(p)/N_1(p) \quad (4.25)$$

The core may have an incoherent and a partially coherent part, the fraction of the partially coherent part is

$$p_c(p) = N_c^p(p)/N_c(p) \quad (4.26)$$

Coherence can come from Bose-Einstein condensate-like behavior or the presence of jets, while incoherence can be caused by a fireball-like expansion of the system.

We know, that the correlation functions have the following simple shape at zero relative momenta [15]:

$$C_2(p_1 \simeq p_2) = f_c^2[(1 - p_c)^2 + 2p_c(1 - p_c)] \quad (4.27)$$

$$C_3(p_1 \simeq p_2 \simeq p_3) = 3f_c^2[(1 - p_c)^2 + 2p_c(1 - p_c)] \quad (4.28)$$

$$+ 2f_c^3[(1 - p_c)^3 + 3p_c(1 - p_c)^2]$$

and

$$p_1 \simeq p_2 \Leftrightarrow Q_{12} \simeq 0 \quad (4.29)$$

$$p_1 \simeq p_2 \simeq p_3 \Leftrightarrow Q_3 \simeq 0 \quad (4.30)$$

If we now measure the correlation functions at nearly zero momenta, we could determine the value of f_c and p_c . For example, the result of the NA22 collaboration is shown in figure 4.1 from ref. [15].

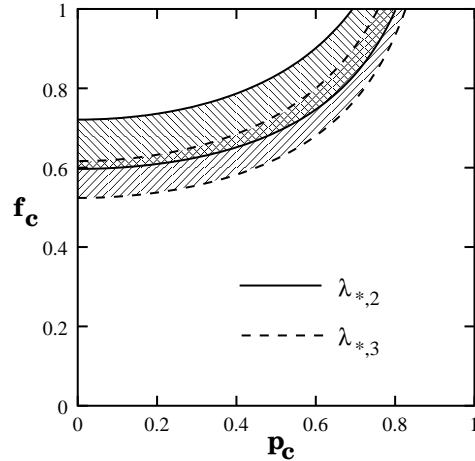


Figure 4.1: Results of the NA22 collaboration from ref [15]

On this figure we see the results from ref. [15]. They determined the (f_c, p_c) range possible from the C_2 analysis and another range from the C_3 analysis. Then, their result is, that the value of the (f_c, p_c) pair has to be in the section of the two ranges.

4.3 Details of the analysis

An analysis of Bose-Einstein correlations of charged pion pairs in Au + Au collisions was done in ref. [16], the method used here is similar to that, as I have to reproduce it's two particle correlation function. So I used similar particle identification and cuts, which are described in the following sections. I used data from RHIC run2 Au+Au collisions, particularly a subset of the data used in ref. [16].

4.3.1 Particle identification

Particles are identified by their mass and charge. The detectors measure momentum, pathlength and time of flight, and from these, we can determine the mass of one particle:

$$m^2 = \left(\left(\frac{t}{L} \right)^2 - 1 \right) p^2 \quad (4.31)$$

Then, we can make cuts on the mass distribution, and regard particles with mass around the pion mass as pions, particles with mass around the kaon mass as kaons, etc. Then we have to decide, where we cut on the mass distribution, at one sigma, two sigma, or so.

The variable is_π , is_K , etc. is provided, and means, how far the actual measured mass of the particle from the physical mass is, in sigma units. So the eg. the definition of is_π is:

$$is_\pi = \frac{m_{meas}^2 - m_{phys}^2}{\Delta m^2} \quad (4.32)$$

Here sigma is determined from detection efficiencies etc.

I made a cut at two sigma for each particle. This can be formulated on the following way:

$$(|is_\pi| \leq 2.0) \wedge (|is_K| \geq 2.0) \wedge (|is_p| \geq 2.0) \quad (4.33)$$

$$(|is_\pi| \geq 2.0) \wedge (|is_K| \leq 2.0) \wedge (|is_p| \geq 2.0) \quad (4.34)$$

$$(|is_\pi| \geq 2.0) \wedge (|is_K| \geq 2.0) \wedge (|is_p| \leq 2.0) \quad (4.35)$$

The result of these PID (particle identification) cuts is to see on figure 4.2.

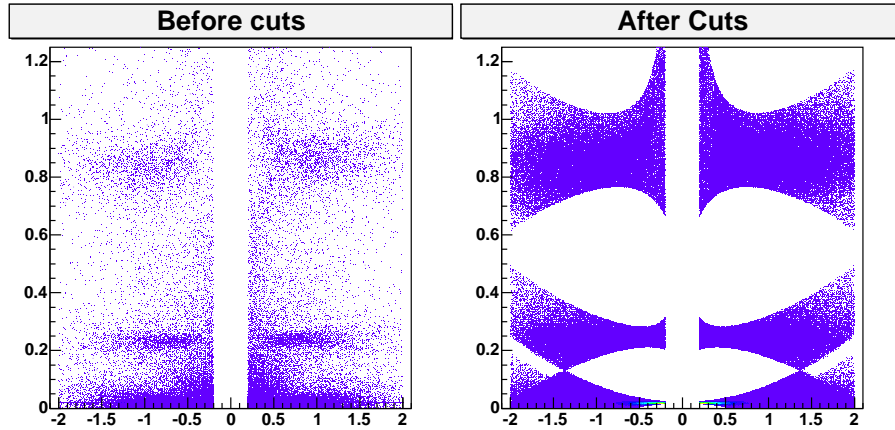


Figure 4.2: Particle identification

In this figure, $mass^2$ versus $charge \times momentum$ was plotted for the selected particles before and after the PID cuts. In the second figure 10 times more data was processed than in the first, but it is still visible, how the most “dense regions” were selected. Note also, how the mass distribution width Δm^2 changes with the momentum.

4.3.2 Cuts

It is necessary to make cuts on the data. This cuts can be classified as one-track cuts or as two-track cuts. The one-tracks are necessary to get rid of the bad tracks, where for example the hit in the detectors was caused by cosmic rays or the particle came from the collision, but it’s momentum was not in the range where the detectors can measure properly. I made several following one-track cuts.

First, I cut on the vertex position:

$$z_{\text{vertex}} \leq 30.0 \text{ cm} \quad (4.36)$$

if the collision happened to far from the midpoint of the detectors, the data is not useful for us.

I made a cut on the drift chamber quality, the exact value of the cut was taken here from previous measurements [16].

$$\text{quality}_{DCH} = 31 \vee 63 \quad (4.37)$$

For particle identification and momentum measurement, the Time Of Flight detector was used, this can measure in the

$$0.2 \text{ GeV} \leq |\mathbf{p}| \leq 2.0 \text{ GeV} \quad (4.38)$$

momentum interval, so we have to drop particles with momentum outside this interval.

Two-track cuts are needed, because all detectors have a finite momentum and space resolution, and cannot separate two tracks if they are too close to each other. Although, we have pairs which are less separated than this resolution, we may not use them.

These two-track cuts were the following:

$$dr_{EMC} \geq 12.0 \text{ cm} \quad (4.39)$$

$$dz_{DCH} \geq 1.0 \text{ cm} \quad (4.40)$$

$$d\varphi_{DCH} \geq 0.02 \text{ rad} \quad (4.41)$$

For example dr_{EMC} means the distance of the two tracks in the Electromagnetic Calorimeter, and the value 12 cm relates to the physical sizes of the EMC modules. The z direction separation is guaranteed by eq. 4.40, and the angular separation by eq. 4.41.

These cuts ensure, that the two tracks were far enough to distinguish them, and not one track was detected two times.

I used only those triplets, in which all pairs matched these above two-track criteria.

-	sum	per event
events	6,453,768	-
unID	223,227,312	35
pions	18,011,527	2.8
protons	1,279,316	0.2
kaons	1,349,631	0.21

Table 4.1: Event statistics

There are 33 unidentified particles in an average event, three are identified as pions, while we have one identified kaon or proton in four events. This data sample of around 6.5 million events was used only to generate statistics. For the purpose of calculating correlation functions, due to time limitations, I used a data sample which is one sixth of the one described here.

-	sum	per event
events	29,874	-
unID	990,077	33
triplets	510,686,484	17,095
+++	54,739,236	1,832
—	73,632,060	2,465
pairs	3,998,784	134
++	907,454	30
-	1,095,550	37

Table 4.2: Statistics for unidentified particles

I had 510 millions of unidentified triplets, and around one tenth of those are of the same charge. Note, that I used here only a little fraction of all events, not to waste lot of time with this type.

4.3.3 Statistics

I used about 10% of all events, this means 800 data files, a total of around 3 million events. Only around 3% of the particles in these events are identified, in case of the other particles, mass could not be measured with the Time Of Flight detector. I call these unidentified particles. The others have a mass, and can be regarded as pions, kaons or protons.

After making the cuts, the number of particles is to see in table 4.1.

Then, I looked for actual pairs and triplets in these particles. There are

$$n_{\text{triplets}} = \frac{n(n-1)(n-2)}{6} \quad (4.42)$$

$$n_{\text{pairs}} = \frac{n(n-1)}{2} \quad (4.43)$$

triplets and pairs in an event with n particles, this means 5456 triplets and 528 pairs for 33 particles (unID) before any pair cuts, and only one triplet and three pairs for the three pions in one event. The situation is a bit complicated, as we see on figure 4.3, but still, we have much more unidentified triplets than pion triplets. Because of this, not to waste time, I used only every 33rd event for gathering unidentified particles. This way, I had around the same number of identified pions and unidentified particles. It is a good approximation, that all particles are pions, so I gave them all pion mass, and made their correlations, too, although among different type of particles, there should not be any Bose-Einstein correlations.

Statistics for the different particle types are shown in tables 4.2-4.5. Interesting is to see, that although we had 3 pions per event, we have more than 300 triplets and 30 pairs per event in average (see table 4.3). This is because although we have only a few events with lots of pions, but these count with a bigger weight (see equations 4.42 and 4.43). As it can be seen on figure 4.3, most of the identified pion triplets come from events with 10-20 pions despite of the little number of these.

-	sum	per event
events	985,848	-
pions	3,284,218	3.3
triplets	344,907,522	350
+++	43,076,400	43.7
—	42,905,754	43.5
pairs	33,417,972	33.9
++	8,380,192	8.5
-	8,320,168	8.4

Table 4.3: Statistics for pions

I had more than 40 million π^+ and π^- triplets in nearly 1,000,000 events, and more than 8 million pairs for both types.

-	sum	per event
events	985,848	-
kaons	261,168	0.26
triplets	254,490	0.26
+++	25,662	0.026
—	36,186	0.037
pairs	254,238	0.26
++	55,548	0.056
-	70,950	0.072

Table 4.4: Statistics for kaons

There are around 260,000 kaons in 1 million events, and we have there 25,662 K^+ triplets while 36,186 K^- triplets, and twice as much pairs.

-	sum	per event
events	985,848	-
protons	256,600	0.26
triplets	252,942	0.26
+++	18,036	0.018
—	48,246	0.049
pairs	262,284	0.27
++	46,184	0.047
-	87,216	0.088

Table 4.5: Statistics for protons

Statistics for protons. The situation is very similar to that of the kaons.

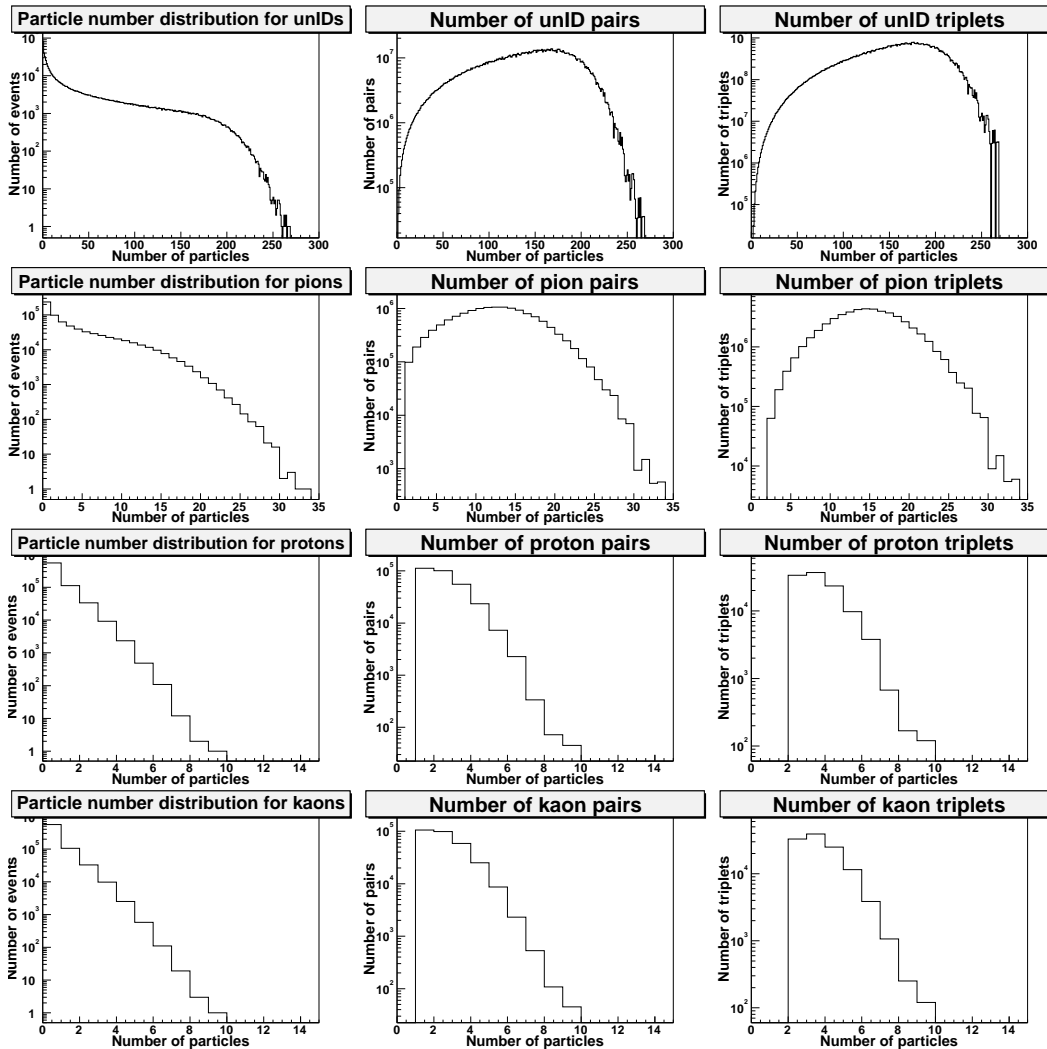


Figure 4.3: Particle and triplet distributions in particular events

These figures show the number of events with a given particle number in the first column, the number of pairs coming from an event with a given particle number in the second column, and the number of triplets in the last column. It is interesting, that eg. although we had only a few protons per event in average, we have lots of triplets, and we have eg. 100 pion triplets per event in average, although we have only 3 pions per event in average. These figures solve this puzzle: there are only a few events with lots of particles, but they count with a bigger weight.

corr	0	1	2	3
i			C_2	C_3
j	unID	π	p	K
k	++	+-	---	
		or		
	+++	++-	+- -	--- -

Table 4.6: Naming convention for the correlation figures

We see the naming convention for the correlation functions on this table. For example, corr2_20 means C_2 for a proton pair, while corr3_12 is the three-particle correlation function of π^+, π^-, π^- triplets.

My three-particle correlation function analysis software is available in ref. [17].

4.4 Results of the analysis

I calculated the actual and background pair and triplet distributions for unidentified particles, identified pions, protons and kaons, and for all possible charge combinations. The naming convention of the correlation functions is shown in table 4.6.

4.4.1 Pair distributions

At first, let us look at the pair distributions for unidentified particles. The idea is here, that most of the particles are pions, so most of the unidentified particle pairs are pion pairs. But for these particles, we do not have a measured mass – that’s why they are unidentified – so I gave these particles the mass of pions.

Figure 4.4 shows us the pair distributions. We see, that at higher p_t end of the curves there is a rise in all the distributions, this could be due to the fact, that these relatively high p_t particles have a higher mass, than the pions mass, so the calculation is not valid for them. Another reason could be, that we see on these plots the sum of two distributions, a narrow one with a maximum in the plotting range, and a broad one, which could have a maximum in the few GeV region.

On figure 4.5 we see the actual and background pair distributions (π^+, π^+), (π^+, π^-), (π^-, π^-) pairs. These distributions go to zero at infinity and at zero, too. The maximum is a little shifted for the +, - case, where we do not expect any Bose-Einstein correlations.

Figures 4.7-4.6 show the pair distributions for (K^+, K^+), (K^+, K^-), (K^-, K^-) pairs, and (p, p), (p, \bar{p}), (\bar{p}, \bar{p}) pairs, respectively. These distribution are a bit noisy due to the small processed number of protons and kaons, but have the same general shape as the pair distributions for pions, just the maximum moved a little toward higher momenta because of the higher mass.

4.4.2 Two-particle correlation functions

$C_2(Q_{12})$ is plotted for unidentified particles and for pions on figure 4.8. In the pion case, there is a clear rise at zero relative momentum for the (+, +) and the (-, -) case, but no one in the (+, -) case, as for different particles there are no Bose-Einstein correlations. A similar effect is observed for the unidentified particles, but their case is still a little bit different because we have there lots of pairs of different particles even in the (+, +) and (-, -) cases. The noise is bigger, too, as I processed almost 10 times more pion pairs as unidentified pairs.

The correlations for protons and kaons are on figure 4.9. We see the common rise for small relative momenta, and it seems to be higher here than for pions, but the errors at the lowest bin are the highest, so this effect is to be investigated in further detail.

4.4.3 Triplet distributions

The pion triplet distributions (fig. 4.11) are very clear, as well as those of unidentified particle triplets (fig. 4.10). We see, that most of the triplets are at higher Q_3 , which makes us the situation a little bit more complicated, as we must have higher statistics to get the correlation function (which is calculated as the ratio of the background and actual distributions) at low Q_3 . If both distributions go to zero too early, C_3 is then 0/0, for such bins I put 0 in C_3 , and so these bins have no physical meaning.

Again, for protons and kaons, the situation is not better. As we have not even less proton triplets, especially a little number of pure, charge-homogenous triplets, the distributions are very noisy (fig. 4.12-4.13). Another problem is, that we have no triplets at all at little momenta, at this will make us hard to track back the C_3 value at $Q_3 = 0$.

4.4.4 Three-particle correlation functions

The three-particle correlation functions for pions and unidentified particles are shown in figure 4.14. In the π^+, π^+, π^+ case, there is a clear rise at low Q_3 -s, the $C_3(Q_3 = 0)$ value could be around 1.6. For unidentified particles, the gap at low Q_3 is higher, but the tail is at one as expected.

In the proton and kaon case (fig. 4.15) we see, that the tails go to one, but the noise gets high in the very region where the correlation function is interesting, so much higher statistics has to be used, i.e. the full data sample available. In

4.5 Future

4.5.1 Improving cuts

If we understand the “funny” behavior of the correlation function, can improve cuts maybe to get better shapes.

4.5.2 Coulomb-correction

Coulomb correction has to be made, because if we calculate for example the two-particle correlation function for π^+ pairs, because of the Coulomb-interaction they repulse each other, and will have a larger momentum-difference, than a π^0 pair would.

The formula for the Coulomb correction was calculated in reference [14]:

$$K_{Coulomb}(Q_3) = \frac{\int d^3\mathbf{x}_1\rho(\mathbf{x}_1)d^3\mathbf{x}_2\rho(\mathbf{x}_2)d^3\mathbf{x}_3\rho(\mathbf{x}_3)|\tilde{\Psi}_{\mathbf{k}_1\mathbf{k}_2\mathbf{k}_3}^{(+S)}(\mathbf{x}_1, \mathbf{x}_2, \mathbf{x}_3)|^2}{\int d^3\mathbf{x}_1\rho(\mathbf{x}_1)d^3\mathbf{x}_2\rho(\mathbf{x}_2)d^3\mathbf{x}_3\rho(\mathbf{x}_3)|\tilde{\Psi}_{\mathbf{k}_1\mathbf{k}_2\mathbf{k}_3}^{(0S)}(\mathbf{x}_1, \mathbf{x}_2, \mathbf{x}_3)|^2} \quad (4.44)$$

4.5.3 Fitting the correlation function

It was discussed in several papers, how these functions should be handled. This means, the fitting should happen with a Gaussian (eq. 4.20) or an Edgeworth (eq. 4.21) shape. At the L3 collaboration, this question was investigated (see figure 4.16). They saw, that the fits with an Edgeworth shape are much better than those with gaussian shape. We will have to look at this, too.

4.6 Summary

From the PHENIX 200 GeV Au+Au data I collected events useful for measuring a correlation function. I selected a particle identification method and made the necessary one-track and two-track cuts. Then I was able to calculate the actual and background triplet and pair distributions A and B for pions, kaons, protons and unidentified particles, for all possible charge-combinations.

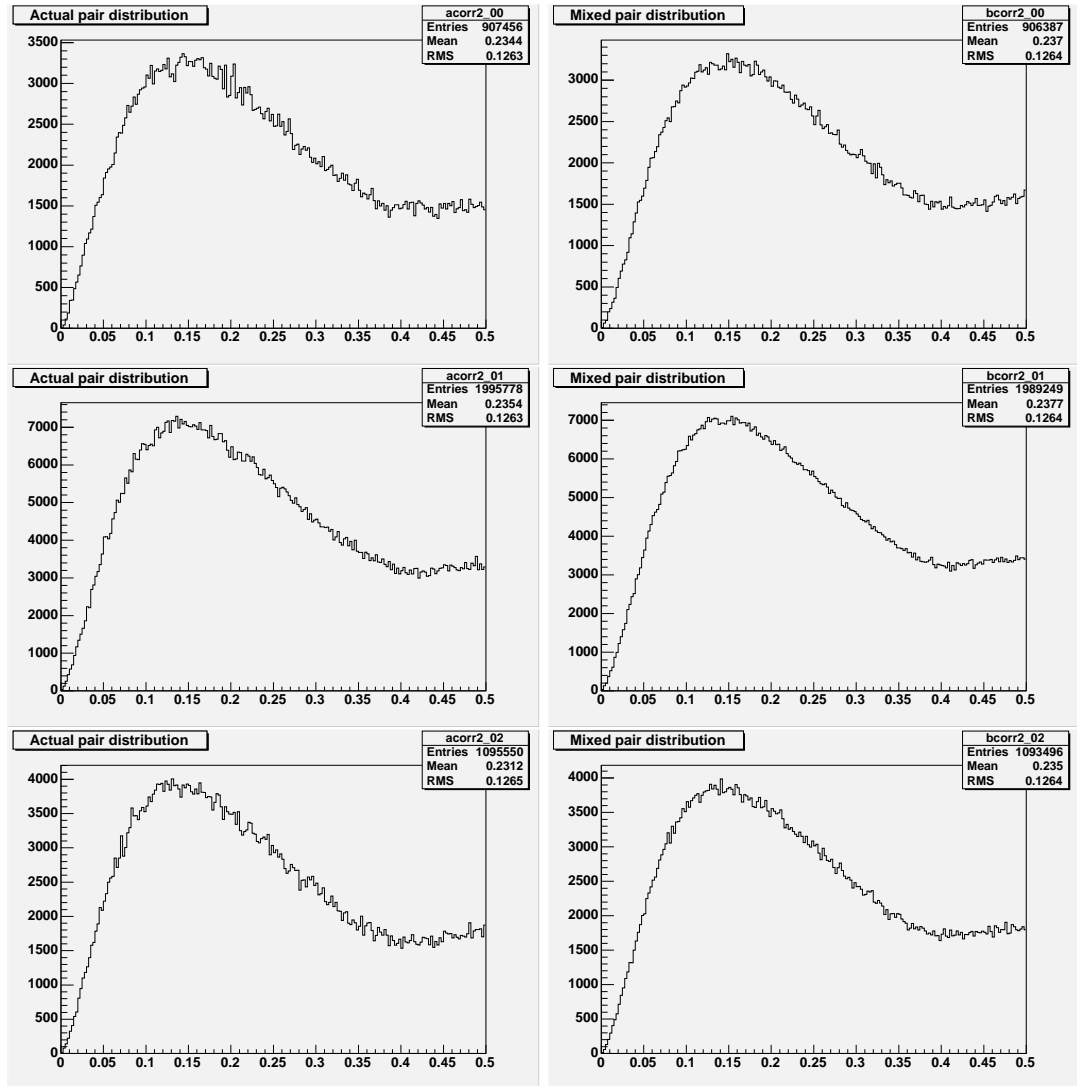


Figure 4.4: Pair distributions for unidentified particles

The actual pair distributions for unidentified particles are plotted in this figure on the left hand side while the background pair distributions are on the right hand side. The three rows represent the charge combinations (+,+), (+,-) and (-,-), respectively. At the higher p_t end of the curves we see the tail of some background distribution, which could be due to long range correlations.

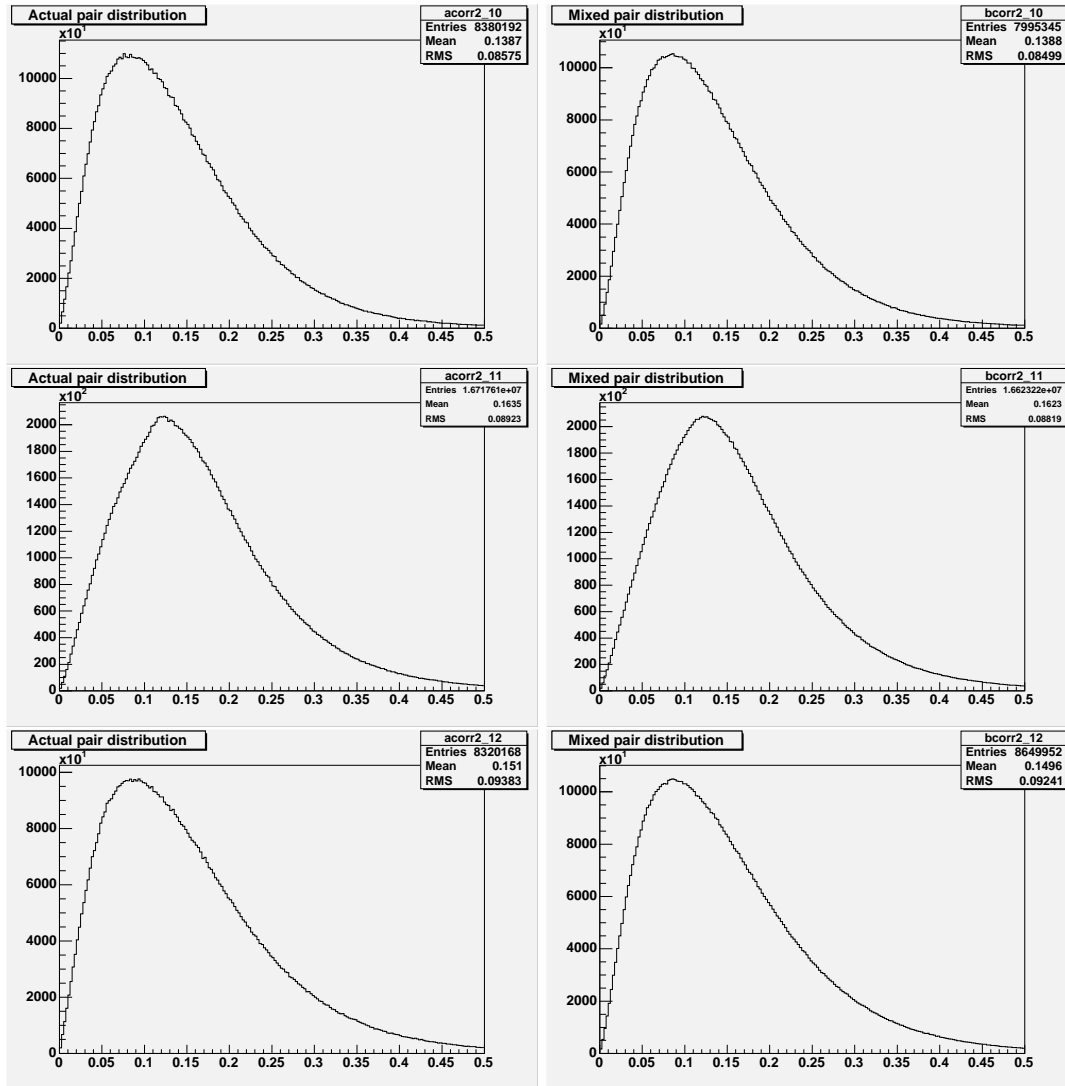


Figure 4.5: Pair distributions for identified pions

In this figure we see the actual (left hand side) and background pair distributions (right hand side) for identified pions. In the first row the (π^+, π^+) pair distributions are shown, in the next line the (π^+, π^-) and in the last line the same for (π^-, π^-) pairs. Note, that the maximum is a little shifted in the $+, -$ case. In this latter case we do not expect any Bose-Einstein correlations.

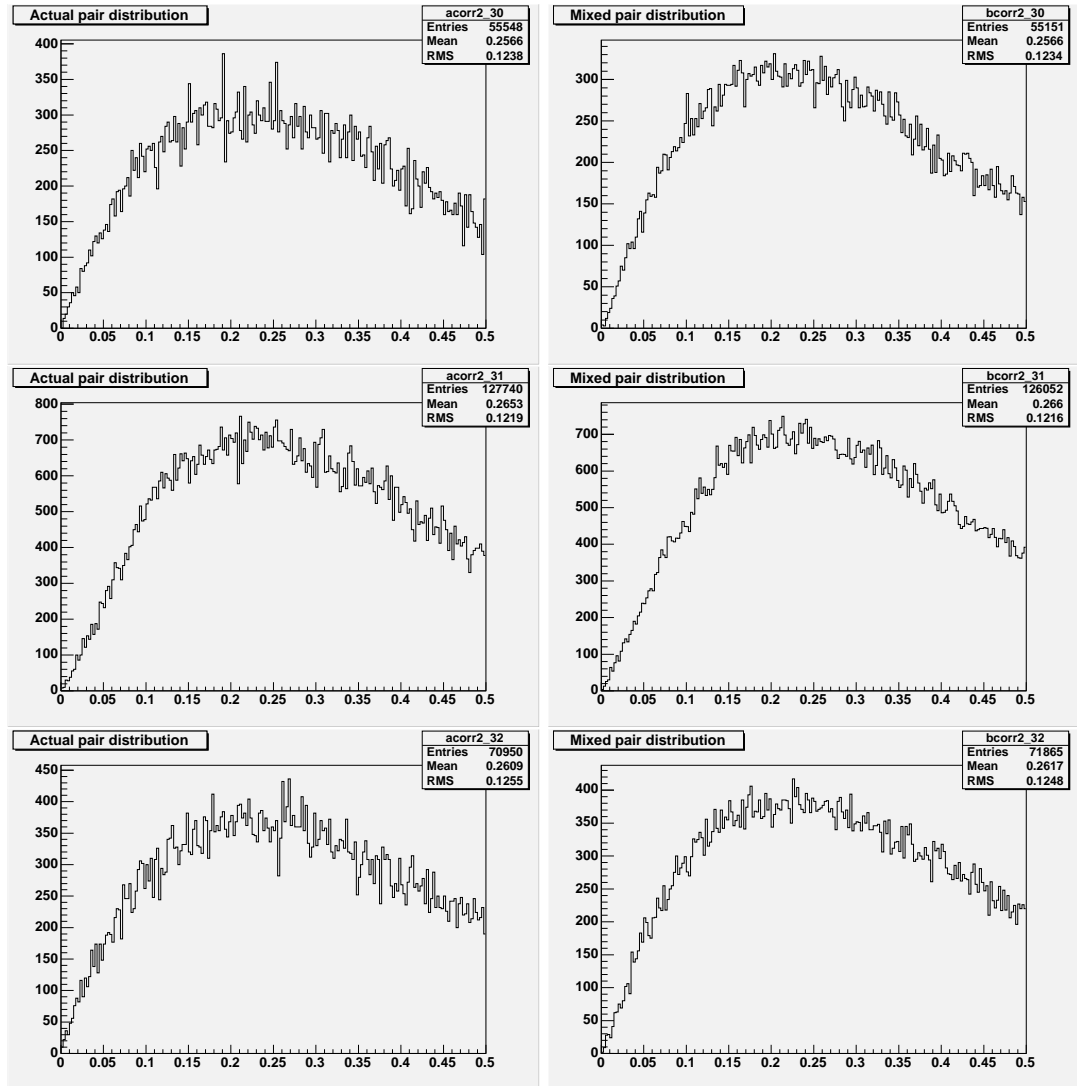


Figure 4.6: Pair distributions for identified kaons

The three rows in this figure show the actual and background pair distributions for (K^+, K^+) , (K^+, K^-) , (K^-, K^-) pairs, respectively. These distributions are a bit noisy due to the small processed number of kaons, but have the same general shape as the pair distributions for pions, just the maximum moved a little toward higher momenta.

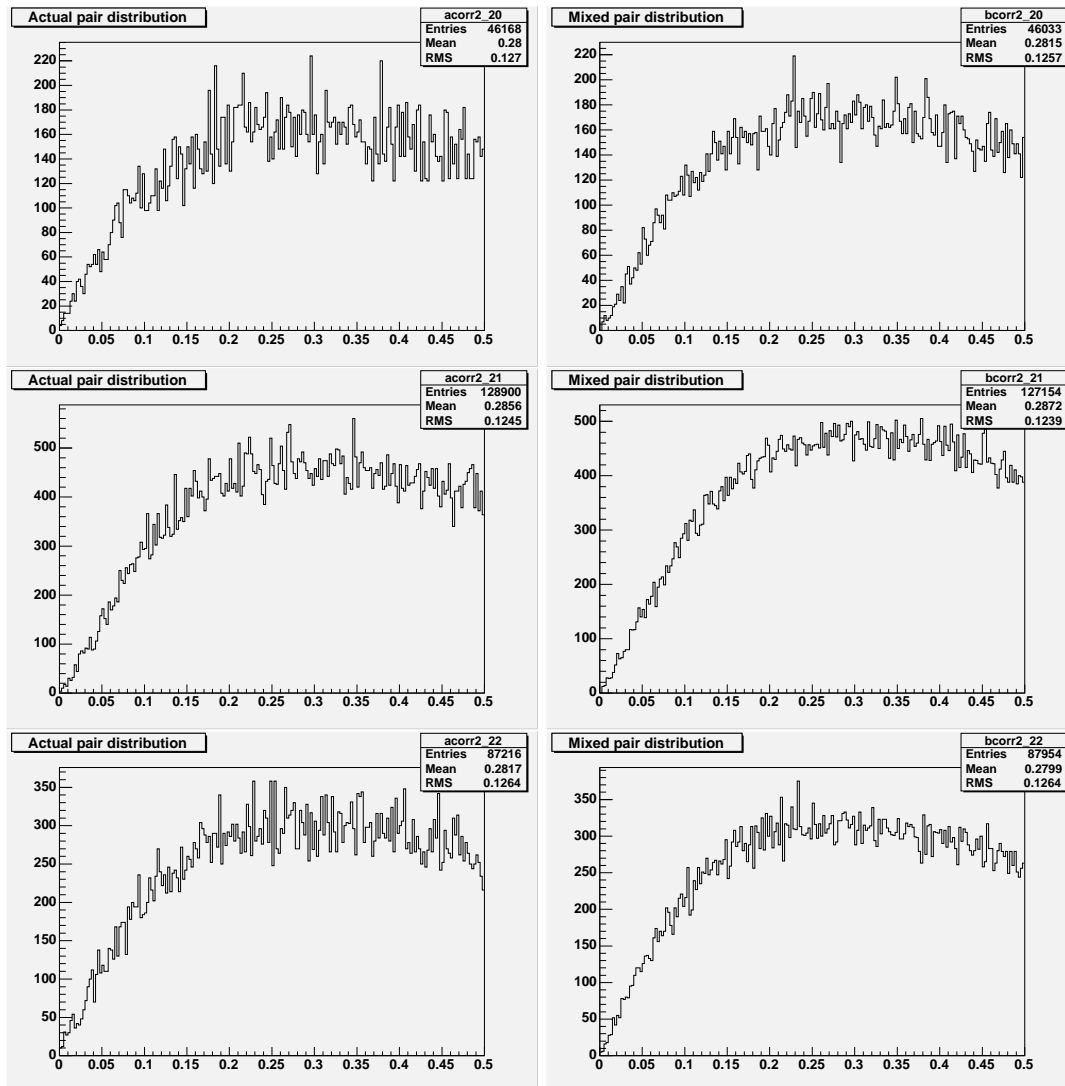


Figure 4.7: Pair distributions for identified protons

In the three rows lines the actual and background pair distributions for (p,p) , (p,\bar{p}) , (\bar{p},\bar{p}) pairs are shown, respectively.

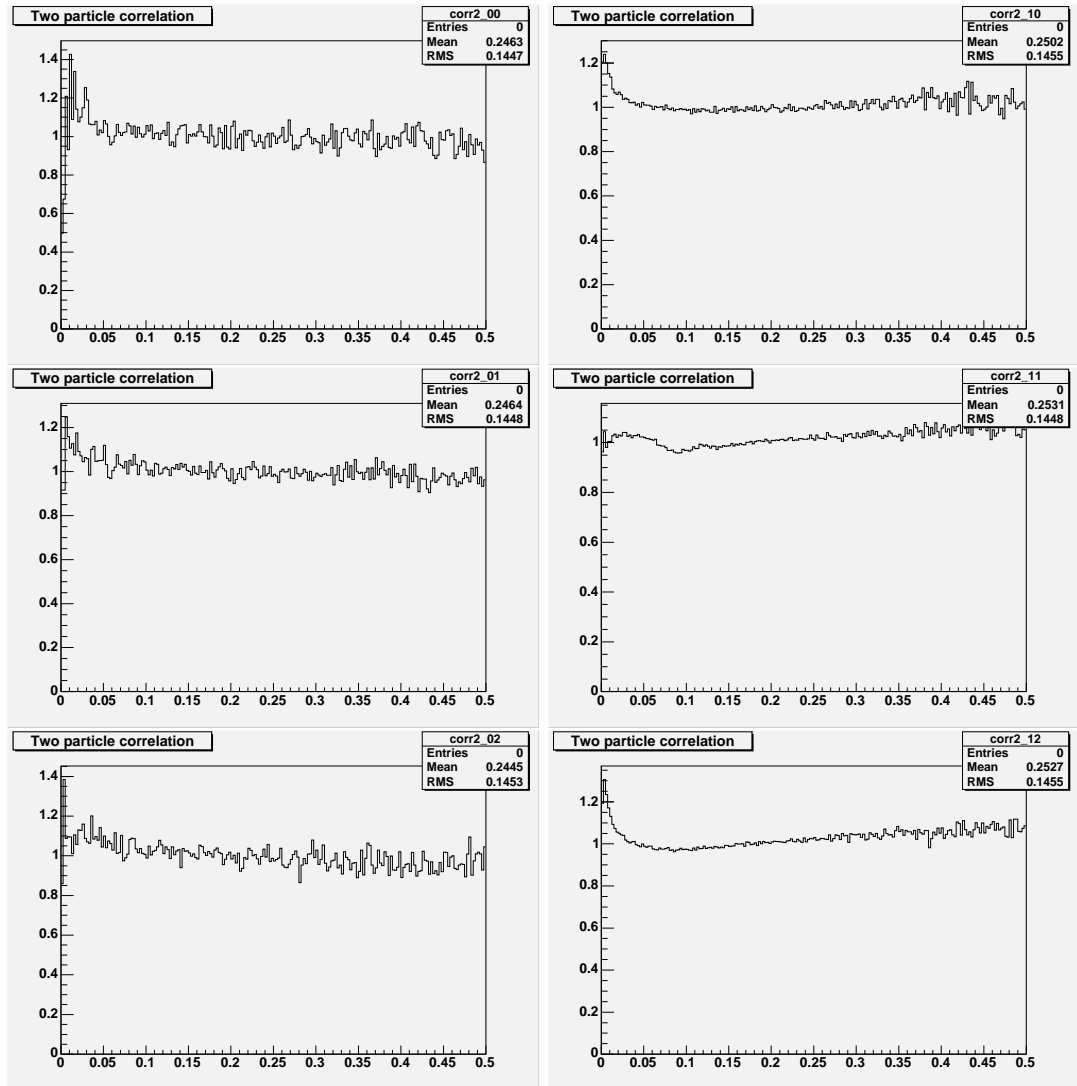


Figure 4.8: Two particle correlation function for unID particles and pions

On the right hand side $C_2(Q_{12})$ is plotted for identified pions. We see there he common two-particle correlation function shape. It is around one at higher momenta, and goes up at zero relative momentum for the $(+, +)$ and the $(-, -)$ case, and is nearly constant for the $(+, -)$ case. The correlation functions of unidentified particles are plotted on the left hand side. Similar shapes are to observe in this latter case.

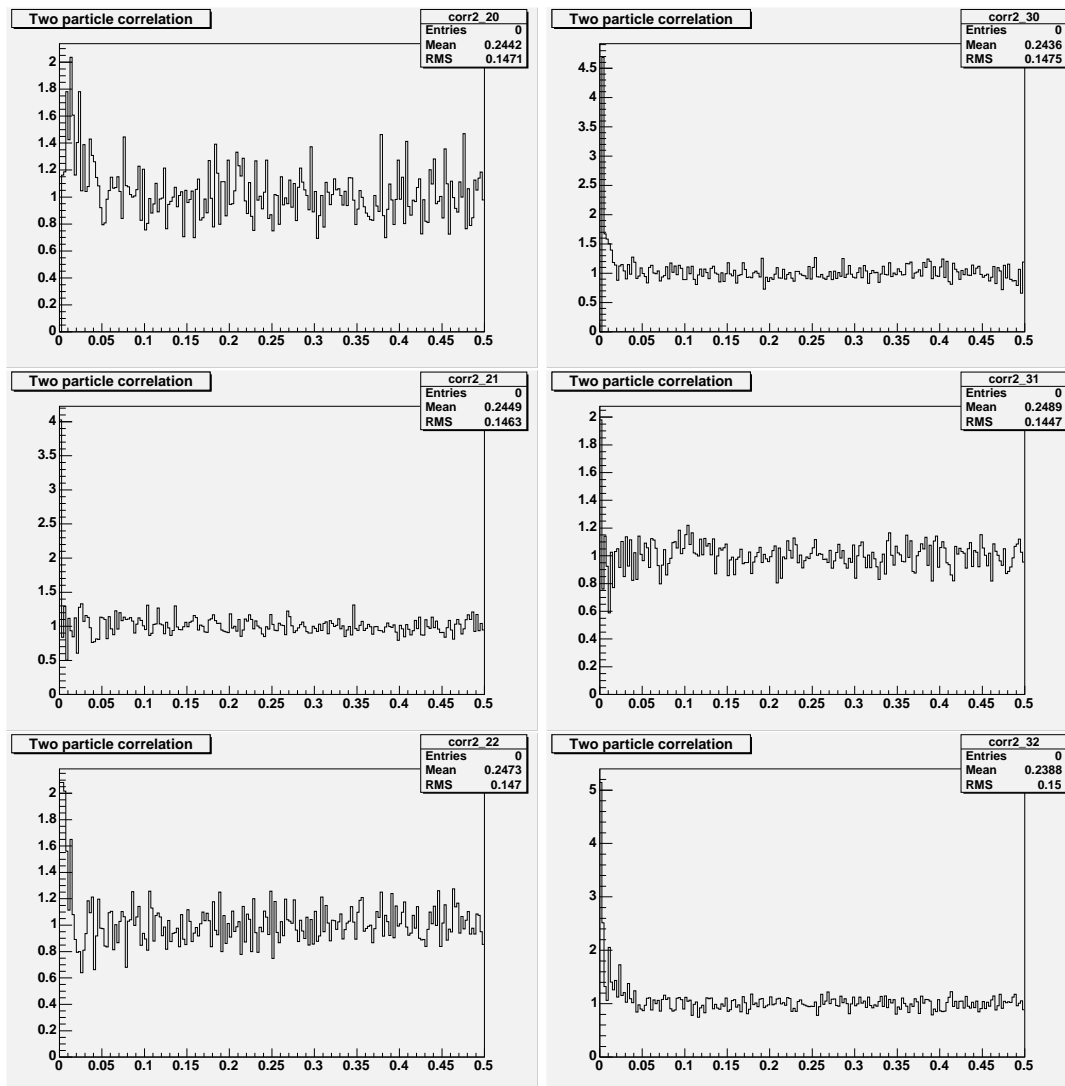


Figure 4.9: Two particle correlation function for protons and kaons

On the left hand side there are the two-particle correlation functions for protons, on the right the same for kaons, in the first row for the $(+, +)$ pairs, then for the $(+, -)$ pairs, and after that for the $(-, -)$ pairs. We see the rise for low relative momenta, and it seems to be higher here than for pions.

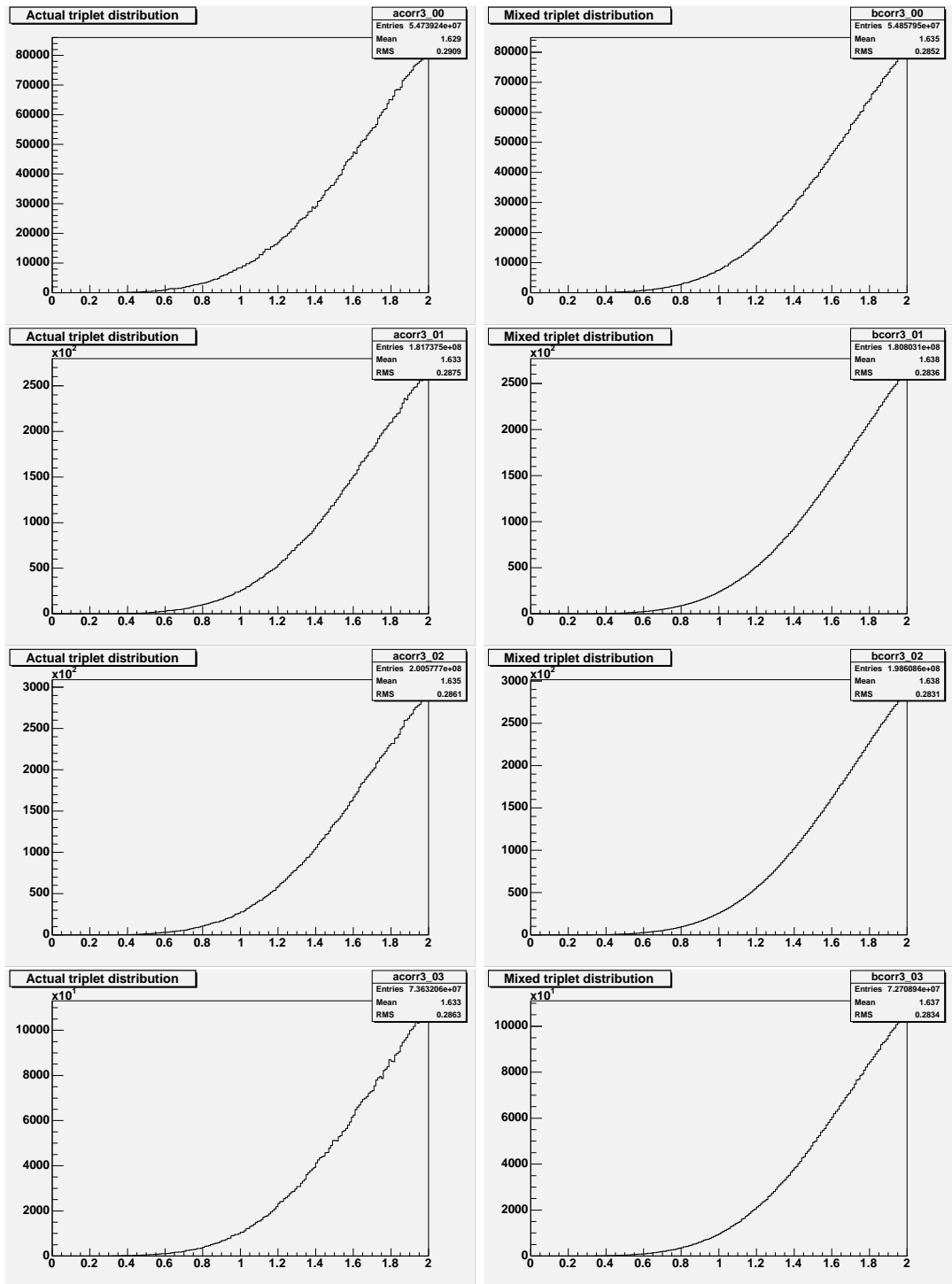


Figure 4.10: Three particle distributions for unidentified particles

The distributions are very clear, and we see, that most of the triplets are at higher Q_3 , which makes the situation a little bit more complicated. Here we have four charge combinations which are represented by the four rows: we can have all three positive, or one, two or three negative charges, too.

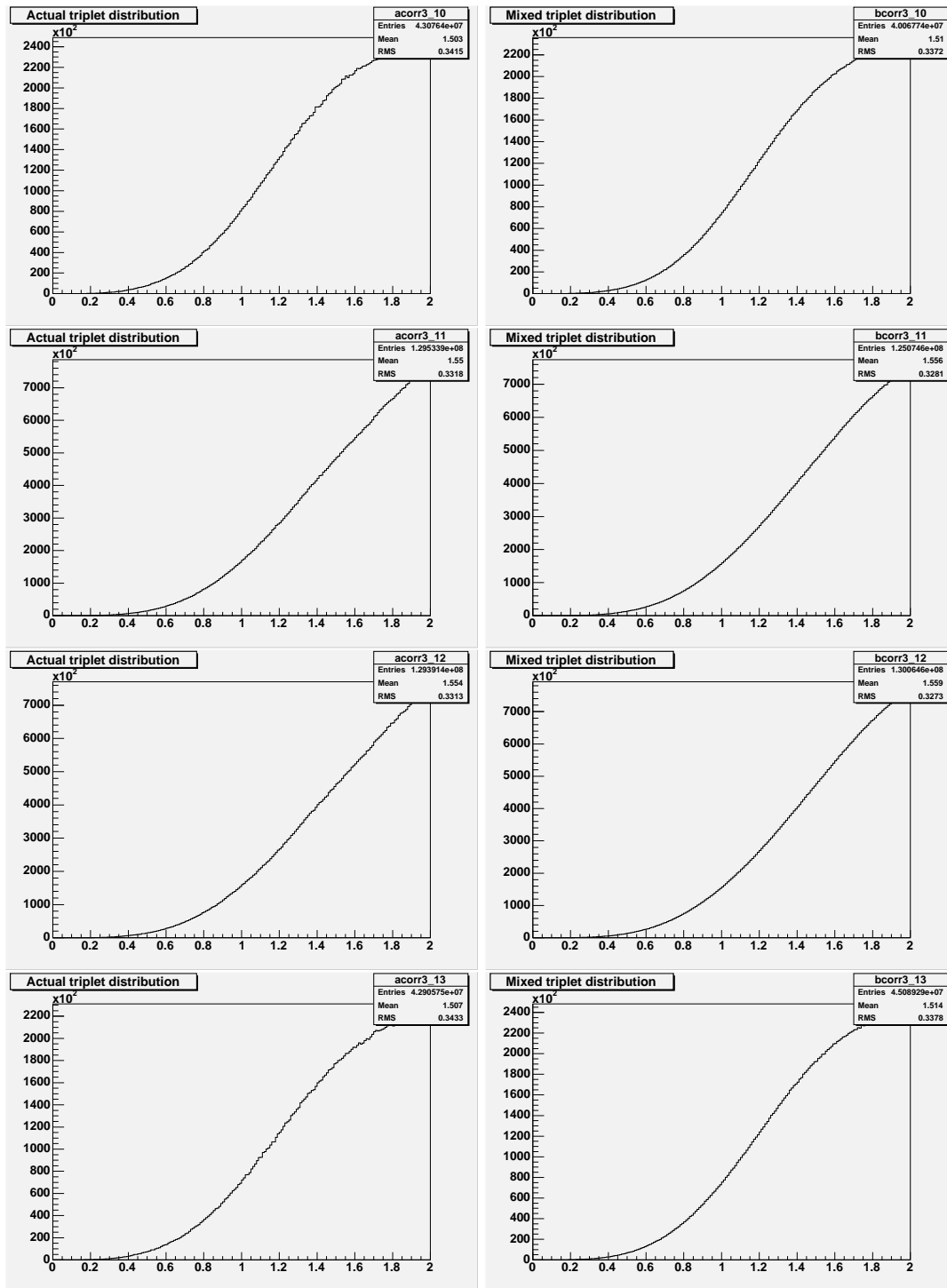


Figure 4.11: Three particle distributions for identified pions

Here we see the beautiful Q_3 spectra of pion triplets, the four rows represent the four possible charge combinations: $\{+, +, +\}$, $\{+, +, -\}$, $\{+, -, -\}$, $\{-, -, -\}$.

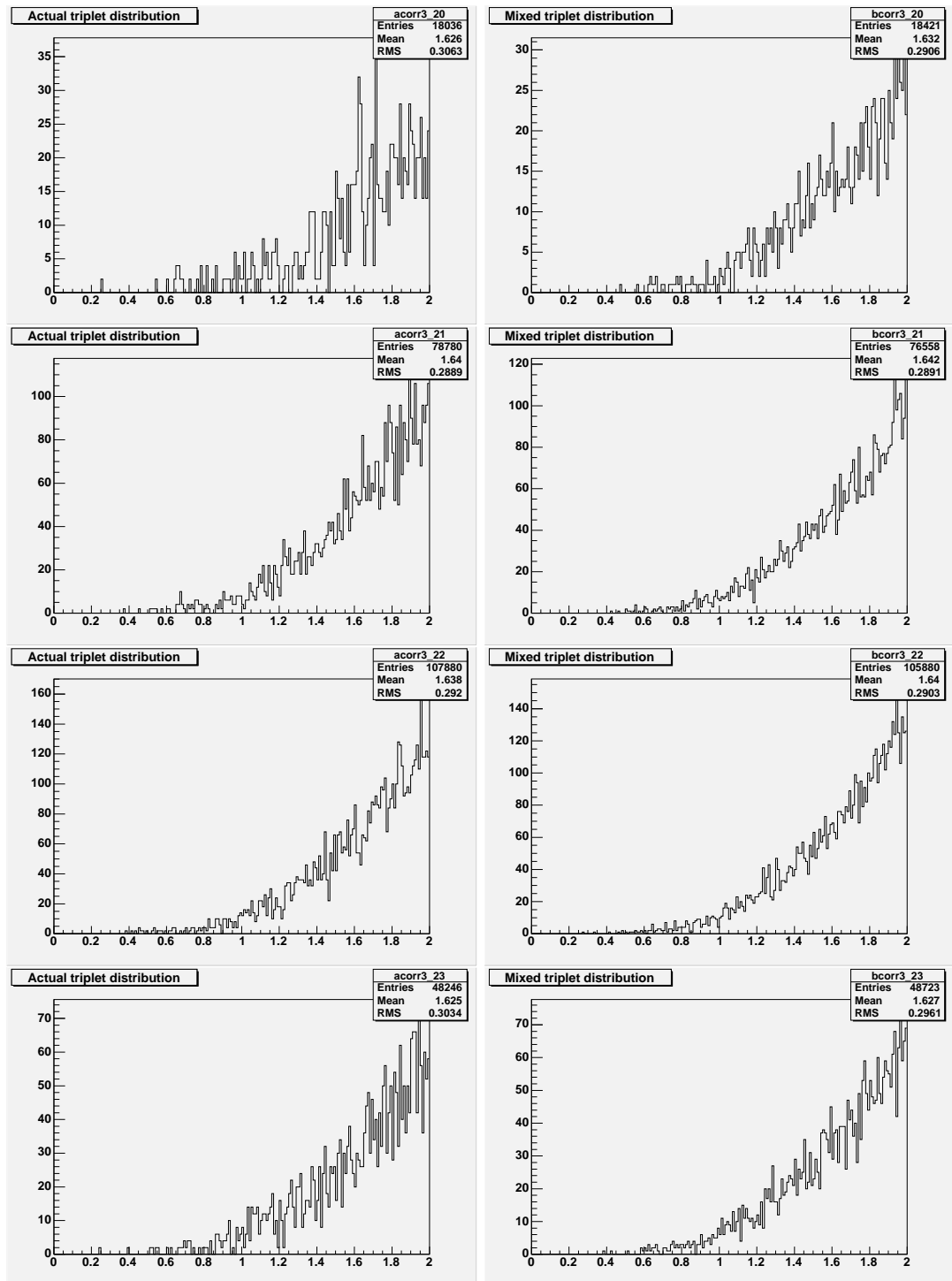


Figure 4.12: Three particle distributions for identified protons

The plots in this figure are arranged on the same way as on figures 4.10 and 4.11. As we have not so many proton triplets, especially a little number of pure, charge-homogenous triplets, the distributions are very noisy. Another problem is, that we have almost no triplets at small relative momenta, at this will make it hard to track back the C_3 value at zero Q_3 .

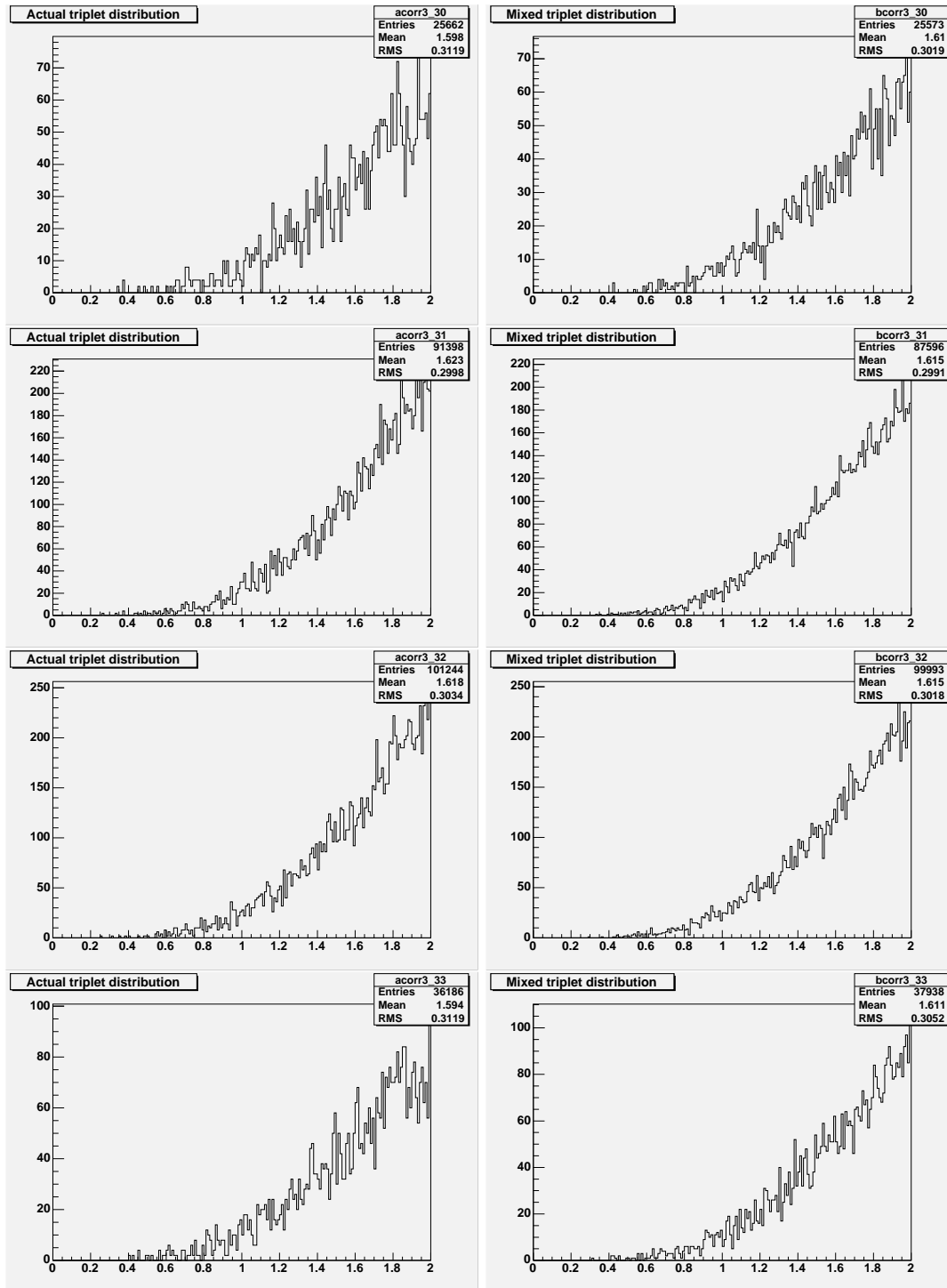


Figure 4.13: Three particle distributions for identified kaons

The situation is similar to that of the protons (see fig. 4.12): noisy distributions, no triplets at small Q_3 . Plot arrangement is the same as before on figures 4.10-4.12.

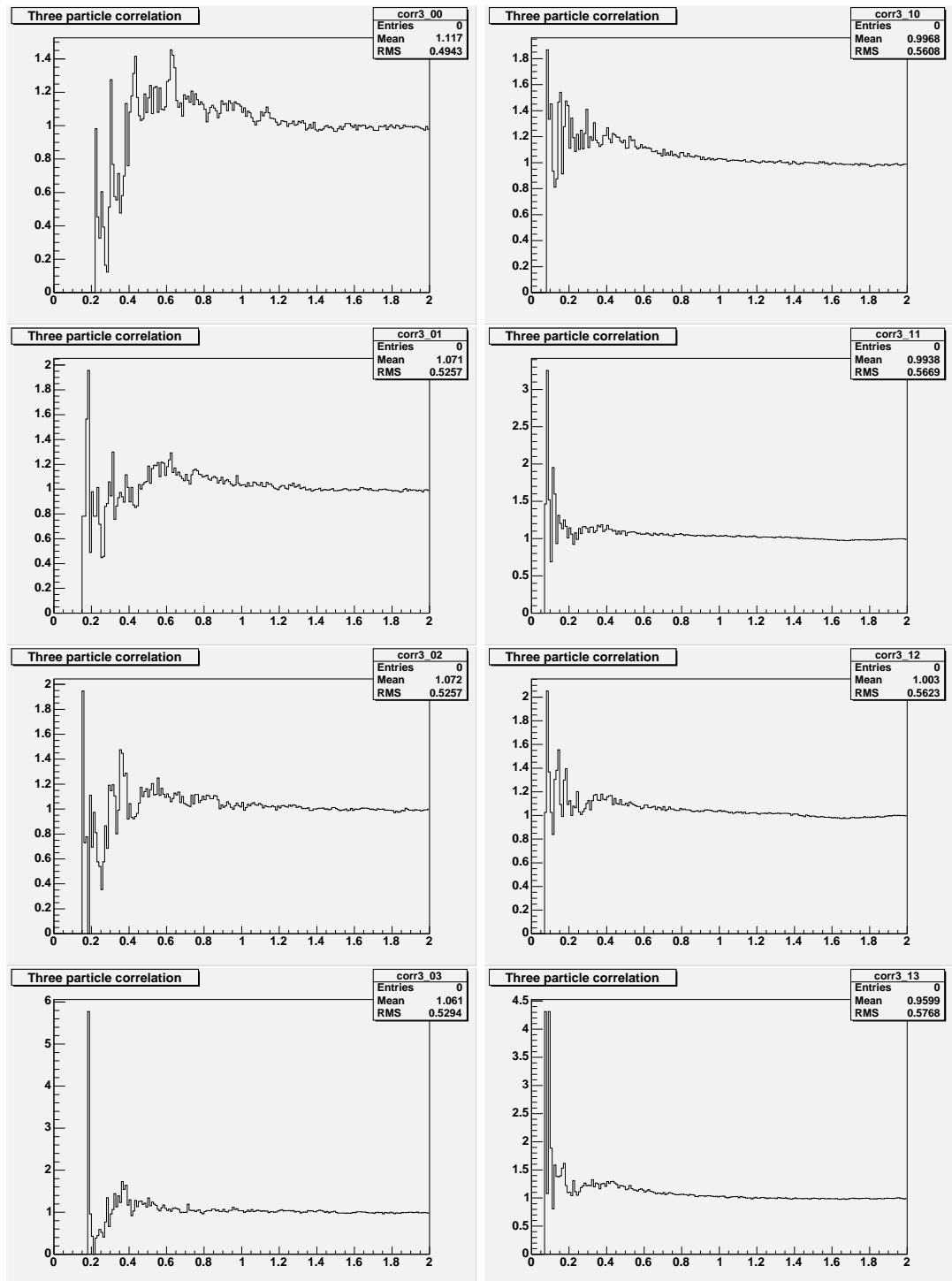


Figure 4.14: Three particle correlation function for unidentified particles and identified pions

Three particle correlation function for unidentified particles (left hand side) and identified pions (right hand side) are plotted in this figure. The four rows represent the four charge combinations: $\{+, +, +\}$, $\{+, +, -\}$, $\{+, -, -\}$ and $\{-, -, -\}$. The clear message of these plots is, that as the errors grow at decreasing momenta, we have to improve a lot on statistics.

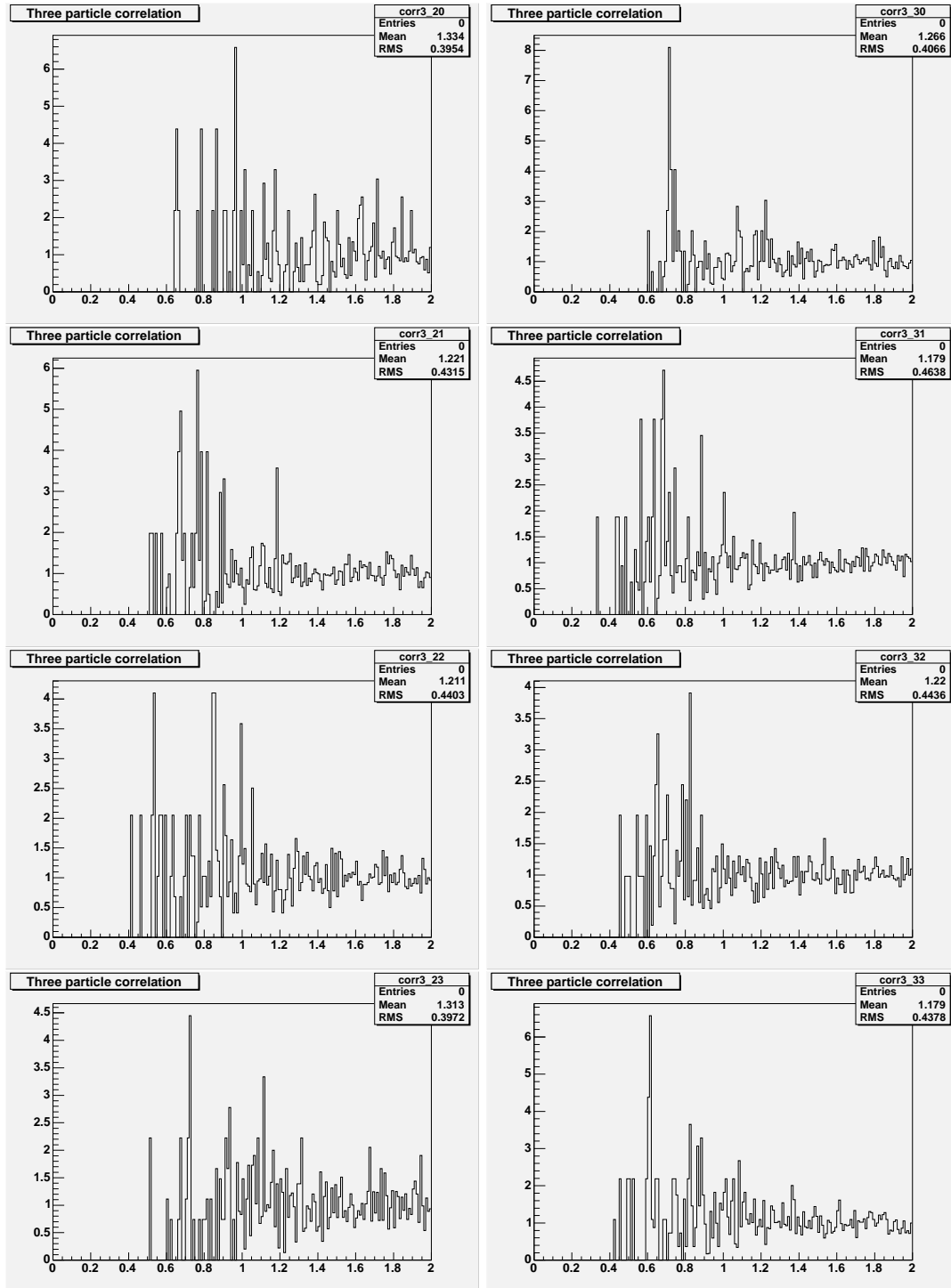


Figure 4.15: Two particle correlation function for identified kaons and protons

C_3 is plotted here for identified kaons (right hand side) and protons (left hand side). The only thing to see here is that the correlation functions are near to one at higher Q_3 , but the errors are too small and the statistic is too small.

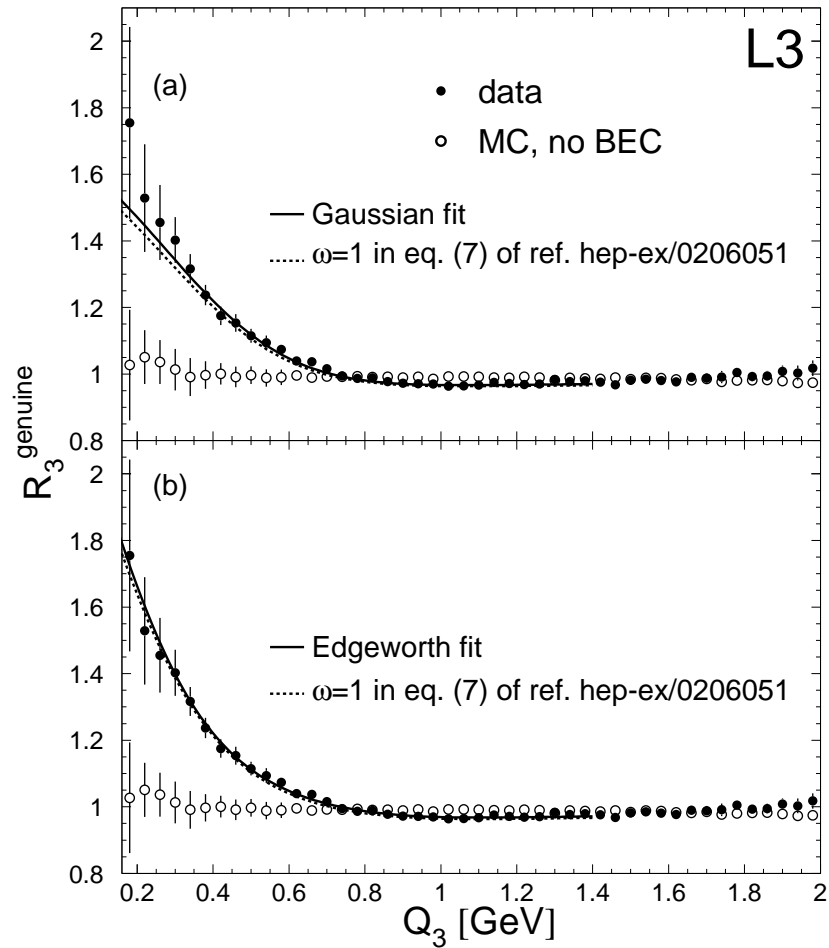


Figure 4.16: Correlation function results of L3

In this figure the $C_3 \equiv R_3^{\text{genuine}}$ result of L3 from ref. [18] is plotted. The upper panel shows the fit with a Gaussian shape, the lower panel the fit with an Edgeworth shape. In the latter case, the fit is much better, so the value at zero relative momenta can be extrapolated more accurately.

On these distributions it was already possible to see, that higher statistics is needed, because too few particles are present in the interesting small relative momentum range for all possible particle-combinations. Then I calculated the raw two- and three-particle correlation functions. Raw means here, that I made no corrections on detector efficiencies or a Coulomb-correction. These correlation functions tend at high relative momenta as desired, and for the pion case it is clearly to see that there is a rise at the low relative momentum end of the histograms. Here the corrections have to be made and then the shape to be fitted.

Chapter 5

Model building

Science . . . never solves a problem without creating ten more.

G. B. SHAW

5.1 The Buda-Lund hydro model

5.1.1 Introduction

The Buda-Lund hydro model [3] is successful in describing the BRAHMS, PHENIX, PHOBOS and STAR data on identified single particle spectra and the transverse mass dependent Bose-Einstein or HBT radii as well as the pseudorapidity distribution of charged particles in Au + Au collisions both at $\sqrt{s_{NN}} = 130$ GeV [19] and at $\sqrt{s_{NN}} = 200$ GeV [20] and in p+p collisions at $\sqrt{s_{NN}} = 200$ GeV [21]. Recently, Fodor and Katz calculated the phase diagram of lattice QCD at finite net baryon density [22]. Their results, obtained with light quark masses four times heavier than the physical value, indicated that in the $0 \leq \mu_B \leq 300$ MeV region the transition from confined to deconfined matter is not a first or second order phase-transition, but a cross-over with a nearly constant critical temperature, $T_c = 172 \pm 3$ MeV. This value was recently calculated more precisely, using the physical quark masses, to be $T_c = 162 \pm 2$ MeV [23], even lower than thought before. The result of the Buda-Lund fits to Au+Au data, both at $\sqrt{s_{NN}} = 130$ and 200 GeV, indicate the existence of a very hot region. The temperature distribution $T(x)$ of this region is characterized with a central temperature T_0 , found to be greater than the critical value calculated from lattice QCD: $T_0 > T_c$ [24]. The Buda-Lund fits thus indicate quark deconfinement in Au + Au collisions at RHIC. The observation of a superheated center in Au+Au collisions at RHIC is confirmed by the analysis of p_t and η dependence of the elliptic flow [24], measured by the PHENIX [25] and PHOBOS collaborations [26, 27]. A similar analysis of Pb+Pb collisions at CERN SPS energies yields central temperatures lower than the critical value, $T_0 < T_c$ [28, 29].

5.1.2 General Buda-Lund hydrodynamics

Hydrodynamics is describing the local conservation of matter, momentum and energy. Due to this nature, hydrodynamical solutions are applied to a tremendous range of physical phenomena ranging from the stellar dynamics to the description of high energy collision of heavy ions as well as collisions of elementary particles. Some of the most famous hydrodynamical solutions, like the Hubble flow of our Universe or the Bjorken flow in ultra-relativistic heavy ion physics have the properties of self similarity and scale-invariance. Heavy ion collisions are known to create three dimensionally expanding systems. In case of non-central collisions, cylindrical symmetry is violated, but an ellipsoidal symmetry can be well assumed to characterize the final state. The data motivated, spherically or cylindrically symmetric hydrodynamical parameterizations and/or solutions of refs. [30, 31] are generalized in the Buda-Lund model, providing new families of exact analytic hydrodynamical solutions.

Hydrodynamics is used to calculate the phase-space distribution, because if we had the phase-space distribution, we could use the collisionless Boltzmann-equation after the freeze-out:

$$\left(\frac{\partial}{\partial t} + \mathbf{v} \nabla \right) f = S(\mathbf{r}, \mathbf{p}, t), \quad (5.1)$$

and so, we would have the emission function. In order to calculate the phase-space distribution, we have to solve the equations of hydrodynamics. There were Buda-Lund solutions for both relativistic and nonrelativistic cases. For example, a general group of solutions for nonrelativistic hydro presented in ref [31, 32, 33] is

$$n(t, \mathbf{r}) = n_0 \frac{V_0}{V} \nu(s), \quad (5.2)$$

$$\mathbf{v}(t, \mathbf{r}) = \left(\frac{\dot{X}}{X} r_x, \frac{\dot{Y}}{Y} r_y, \frac{\dot{Z}}{Z} z_x \right) \text{ and} \quad (5.3)$$

$$T(t, \mathbf{r}) = T_0 \left(\frac{V_0}{V} \right)^{c_s^2} \mathcal{T}(s), \quad (5.4)$$

if the scales X , Y and Z fulfill

$$X\ddot{X} = Y\ddot{Y} = Z\ddot{Z} = \frac{T_i}{m} \left(\frac{V_0}{V} \right)^{c_s^2}. \quad (5.5)$$

Here c_s is the speed of sound, defined as

$$c_s^2 = \left. \frac{dp}{d\epsilon} \right|_{s/n}. \quad (5.6)$$

Furthermore, the scaling functions $\nu(s)$ and $\mathcal{T}(s)$ are not independent, but can be calculated from each other:

$$\nu(s) = \frac{1}{\mathcal{T}(s)} \exp \left(-\frac{T_i}{2T_0} \int_0^s \frac{du}{\mathcal{T}(u)} \right), \quad (5.7)$$

and they depend on a scaling variable s , which can be chosen as

$$s = \frac{r_x^2}{2X_f^2} + \frac{r_y^2}{2Y_f^2} + \frac{r_z^2}{2Z_f^2}. \quad (5.8)$$

Then, the Buda-Lund type of solution is a special case, with the choice of

$$\mathcal{T}(s) = \frac{1}{1+bs} \quad \text{and} \quad (5.9)$$

$$\nu(s) = (1+bs) \exp \left(-\frac{T_i}{2T_0} (s + bs^2/2) \right). \quad (5.10)$$

From this solution, the phase-space distribution is

$$f(\mathbf{r}, \mathbf{p}, t) = C \exp \left(-\frac{r_x^2}{2X(t)^2} - \frac{r_y^2}{2Y(t)^2} - \frac{r_z^2}{2Z(t)^2} - \frac{(\mathbf{p} - m\mathbf{v}(\mathbf{r}, t))^2}{2mT(\mathbf{r}, t)} \right), \quad (5.11)$$

with the constant

$$C = \frac{N}{V_0(4\pi^2 m T_0)^{3/2}}. \quad (5.12)$$

If we now assume a sudden freeze-out and take the simplest, spherically symmetric case with $X = Y = Z$, we can calculate the emission function:

$$S(\mathbf{r}, \mathbf{p}, t) = C \exp \left(-\frac{r^2}{2R_0^2} - \frac{(\mathbf{p} - \frac{m}{\tau}\mathbf{r})^2}{2mT_0} \right) \delta(t - t_0). \quad (5.13)$$

In ref [34, 35] a group of relativistic solutions was calculated:

$$u_\mu(x) = \frac{x_\mu}{\tau}, \quad (5.14)$$

$$n(x) = n_0 \left(\frac{\tau_0}{\tau} \right)^3 \nu(s), \quad (5.15)$$

$$p(x) = p_0 \left(\frac{\tau_0}{\tau} \right)^{3+3/\kappa}, \quad (5.16)$$

$$T(x) = T_0 \left(\frac{\tau_0}{\tau} \right)^{3/\kappa} \frac{1}{\nu(s)}. \quad (5.17)$$

In the following sections, we will assume a source function, which is similar to the case of these solutions, but the exact solution, which would lead to that particular source function, was not found yet. The next section will describe the axially symmetric case, and in the section after that the model is generalized to the case of ellipsoidal symmetry. Detailed calculations are presented in this latter case only, because the former case would be the same, just with more symmetry.

5.2 Axially symmetric Buda-Lund hydro model

5.2.1 The emission function

The Buda-Lund hydro model was introduced in refs. [3, 36]. This model was defined in terms of its emission function $S(x, k)$, for axial symmetry, corresponding to central collisions of symmetric nuclei. The observables are calculated analytically, see refs. [29, 19] for details and key features. Here we summarize the Buda-Lund emission function in terms of its fit parameters. The presented form is equivalent to the original shape proposed in refs. [3, 36], however, it is easier to fit and interpret it.

The single particle invariant momentum distribution, $N_1(k_1)$, is obtained as

$$N_1(k_1) = \int d^4x S(x, k_1). \quad (5.18)$$

For chaotic (thermalized) sources, in case of the validity of the plane-wave approximation, the two-particle invariant momentum distribution $N_2(k_1, k_2)$ is also determined by $S(x, k)$, the single particle emission function, if non-Bose-Einstein correlations play negligible role or can be corrected for, see ref. [29] for a more detailed discussion. Then the two-particle Bose-Einstein correlation function, $C_2(k_1, k_2) = N_2(k_1, k_2) / [N_1(k_1)N_1(k_2)]$ can be evaluated in a core-halo picture [37], where the emission function is a sum of emission functions characterizing a hydrodynamically evolving core and a surrounding halo of decay products of long-lived resonances, $S(x, k) = S_c(x, k) + S_h(x, k)$. Consequently, the single particle spectra can also be given as a sum, $N_1(k) = N_{1,c}(k) + N_{1,h}(k)$.

$$C_2(k_1, k_2) = 1 + \frac{|\tilde{S}(q, K)|^2}{|\tilde{S}(0, K)|^2} \simeq 1 + \lambda_*(K) \frac{|\tilde{S}_c(q, K)|^2}{|\tilde{S}_c(0, K)|^2}, \quad (5.19)$$

where the relative and the momenta are $q = k_1 - k_2$, $K = 0.5(k_1 + k_2)$, and the Fourier-transformed emission function is defined as

$$\tilde{S}(q, K) = \int d^4x S(x, K) \exp(iqx). \quad (5.20)$$

The measured λ_* parameter of the correlation function is utilized to correct the core spectrum for long-lived resonance decays [37]. This parameter can be calculated from the equation

$$N_1(k) = N_{1,c}(k) / \sqrt{\lambda_*(k)} \quad (5.21)$$

as

$$\lambda_*(k) = \left[\frac{N_{1,c}(k)}{N_{1,c}(k) + N_{1,h}(k)} \right]^2 \quad (5.22)$$

The emission function of the core is assumed to have a hydrodynamical form,

$$S_c(x, k) d^4x = \frac{g}{(2\pi)^3} \frac{k^\nu d^4\Sigma_\nu(x)}{B(x, k) + s_q}, \quad (5.23)$$

where g is the degeneracy factor ($g = 1$ for pseudoscalar mesons, $g = 2$ for spin=1/2 barions). The particle flux over the freeze-out layers is given by a generalized Cooper-Frye factor: the freeze-out hypersurface depends parametrically on the freeze-out time τ and the probability to freeze-out at a certain value is proportional to $H(\tau)$,

$$k^\nu d^4\Sigma_\nu(x) = m_t \cosh(\eta - y) H(\tau) d\tau \tau_0 d\eta dr_x dr_y. \quad (5.24)$$

Here the coordinates are $x = (t, r_x, r_y, r_z)$, the components of the momenta $k = (E, k_x, k_y, k_z)$, while $\eta = 0.5 \log[(t + r_z)/(t - r_z)]$, $\tau = \sqrt{t^2 - r_z^2}$, $y = 0.5 \log[(E + k_z)/(E - k_z)]$ and $m_t = \sqrt{E^2 - k_z^2}$.

The freeze-out time distribution $H(\tau)$ is approximated by a Gaussian,

$$H(\tau) = \frac{1}{(2\pi\Delta\tau^2)^{3/2}} \exp\left[-\frac{(\tau - \tau_0)^2}{2\Delta\tau^2}\right], \quad (5.25)$$

where τ_0 is the mean freeze-out time, and the $\Delta\tau$ is the duration of particle emission, satisfying $\Delta\tau \ll \tau_0$. The (inverse) Boltzmann phase-space distribution, $B(x, k)$ is given by

$$B(x, k) = \exp\left(\frac{k^\nu u_\nu(x)}{T(x)} - \frac{\mu(x)}{T(x)}\right), \quad (5.26)$$

and the term s_q is 0, -1 , and $+1$ for Boltzmann, Bose-Einstein and Fermi-Dirac statistics, respectively. The flow four-velocity, $u^\nu(x)$, the chemical potential, $\mu(x)$, and the temperature, $T(x)$ distributions for axially symmetric collisions were determined from the principles of simplicity, analyticity and correspondence to hydrodynamical solutions in the limits when such solutions were known [3, 36]. Recently, the Buda-Lund hydro model lead to the discovery of a number of new, exact analytic solutions of hydrodynamics, both in the relativistic [34, 35] and in the non-relativistic domain [31, 32, 33].

The expanding matter is assumed to follow a three-dimensional, relativistic flow, characterized by transverse and longitudinal Hubble constants,

$$u^\nu(x) = (\gamma, H_t r_x, H_t r_y, H_z r_z), \quad (5.27)$$

where γ is given by the normalization condition $u^\nu(x)u_\nu(x) = 1$. In the original form, this four-velocity distribution $u^\nu(x)$ was written as a linear transverse flow, superposed on a scaling longitudinal Bjorken flow. The strength of the transverse flow was characterized by its value $\langle u_t \rangle$ at the ‘‘geometrical’’ radius R_G , see refs. [3, 38, 39]:

$$\begin{aligned} u^\nu(x) &= \left(\cosh[\eta] \cosh[\eta_t], \sinh[\eta_t] \frac{r_x}{r_t}, \sinh[\eta_t] \frac{r_y}{r_t}, \sinh[\eta] \cosh[\eta_t] \right), \\ \sinh[\eta_t] &= \langle u_t \rangle r_t / R_G, \end{aligned} \quad (5.28)$$

with $r_t = (r_x^2 + r_y^2)^{1/2}$. Such a flow profile, with a time-dependent radius parameter R_G , was recently shown to be an exact solution of the equations of relativistic hydrodynamics of a perfect fluid at a vanishing speed of sound, see refs. [40, 41].

The Buda-Lund hydro model characterizes the inverse temperature $1/T(x)$, and fugacity, $\exp[\mu(x)/T(x)]$ distributions of an axially symmetric, finite hydrodynamically expanding system with the mean and the variance of these distributions, in particular

$$\frac{\mu(x)}{T(x)} = \frac{\mu_0}{T_0} - \frac{r_x^2 + r_y^2}{2R_G^2} - \frac{(\eta - y_0)^2}{2\Delta\eta^2}, \quad (5.29)$$

$$\frac{1}{T(x)} = \frac{1}{T_0} \left(1 + \frac{r_t^2}{2R_s^2}\right) \left(1 + \frac{(\tau - \tau_0)^2}{2\Delta\tau_s^2}\right). \quad (5.30)$$

Here R_G and $\Delta\eta$ characterize the spatial scales of variation of the fugacity distribution, $\exp[\mu(x)/T(x)]$. These variables control particle densities. Hence these scales are referred to as geometrical lengths. These are distinguished from the scales on which the inverse temperature distribution changes, the temperature drops to half if $r_x = r_y = R_s$ or if $\tau = \tau_0 + \sqrt{2}\Delta\tau_s$. These parameters can be considered as second order Taylor expansion coefficients of these profile functions, restricted only by the symmetry properties of the source, and can be trivially expressed by re-scaling the earlier fit parameters. The above is the most direct form of the Buda-Lund model. However, different combinations may also be used to measure the flow, temperature and fugacity profiles [3, 29]: $H_t \equiv b/\tau_0 = \langle u_t \rangle / R_G = \langle u_t' \rangle / R_s$, $H_l \equiv \gamma_t / \tau_0$, where $\gamma_t = \sqrt{1 + H_t^2 r_t^2}$ is evaluated at the point of maximal emittivity, and

$$\frac{1}{R_s^2} = \frac{a^2}{\tau_0^2} = \left\langle \frac{\Delta T}{T} \right\rangle_r \frac{1}{R_G^2} = \frac{T_0 - T_s}{T_s} \frac{1}{R_G^2}, \quad (5.31)$$

$$\frac{1}{\Delta\tau_s^2} = \frac{d^2}{\tau_0^2} = \left\langle \frac{\Delta T}{T} \right\rangle_s \frac{1}{\Delta\tau^2} = \frac{T_0 - T_e}{T_e} \frac{1}{\Delta\tau^2}. \quad (5.32)$$

Buda-Lund parameter	Au+Au 200 GeV	Au+Au 130 GeV
T_0 [MeV]	196 \pm 13	214 \pm 7
T_e [MeV]	117 \pm 12	102 \pm 11
μ_B [MeV]	61 \pm 52	77 \pm 38
R_G [fm]	13.5 \pm 1.7	28.0 \pm 5.5
R_s [fm]	12.4 \pm 1.6	8.6 \pm 0.4
$\langle u'_t \rangle$	1.6 \pm 0.2	1.0 \pm 0.1
τ_0 [fm/c]	5.8 \pm 0.3	6.0 \pm 0.2
$\Delta\tau$ [fm/c]	0.9 \pm 1.2	0.3 \pm 1.2
$\Delta\eta$	3.1 \pm 0.1	2.4 \pm 0.1
χ^2/NDF	114 / 208	158.2 / 180

Table 5.1: Fit results from RHIC $\sqrt{s_{NN}} = 130$ and 200 GeV data

The first column shows the source parameters from simultaneous fits of final BRAHMS and PHENIX data for 0 - 30 % most central Au + Au collisions at $\sqrt{s_{NN}} = 200$ GeV, as shown in Figs. 1 and 2, as obtained with the Buda-Lund hydro model, version 1.5. The errors on these parameters are still preliminary. The second column is the result of an identical analysis of BRAHMS, PHENIX, PHOBOS and STAR data for 0 - 5 % most central Au+Au collisions at $\sqrt{s_{NN}} = 130$ GeV, ref. [19].

5.2.2 Buda-Lund fit results to central Au+Au data

In this section, we present new fit results to 0-5(6) % central Au+Au data at $\sqrt{s_{NN}} = 130$ GeV from refs. [42, 43, 44, 45, 46], to BRAHMS data on charged particle pseudorapidity distributions [47], and PHENIX data on identified particle momentum distributions and Bose-Einstein (HBT) radii [48, 49] in Au+Au collisions at $\sqrt{s_{NN}} = 200$ GeV. The fits are shown in figures 5.1 and 5.2, the fit parameters in table 5.1.

Let us clarify first the meaning of the parameters shown in table 5.1. The temperature at the center of the fireball at the mean freeze-out time is denoted by $T_0 \equiv T(r_x = r_y = 0, \tau = \tau_0)$. The ‘‘surface temperature’’ $T_s \equiv T(r_x = r_y = R_s, \tau = \tau_0) = T_0/2$ is also a characteristic value. This relationship defines the ‘‘surface’’ radius R_s , which is in fact the FWHM (full-width at half-maximum) of the temperature distribution. During the particle emission, the system may cool due to evaporation and expansion, this is measured by the ‘‘post-evaporation temperature’’ $T_e \equiv T(r_x = r_y = 0, \tau = \tau_0 + \sqrt{2}\Delta\tau)$. In the presented cases, the strength of the transverse flow is measured by $\langle u'_t \rangle$, it’s value at the ‘‘surface radius’’ R_s . The ‘‘mean freeze-out time’’ parameter is denoted by τ_0 and the ‘‘duration’’ of particle emission, or the width of the freeze-out time distribution is measured by $\Delta\tau$. The fugacity distribution varies on the characteristic transverse scale given by the ‘‘geometrical radius’’ R_G . If $R_G \rightarrow \infty$, then $\mu(x)/T(x)$ is constant. Finally, the width of the space-time rapidity distribution, or the longitudinal variation scale of the fugacity distribution is measured by the parameter $\Delta\eta$.

Perhaps it could be more appropriate to directly fit the transverse Hubble constant, $H_t = \langle u'_t \rangle/R_s$ to the data, as this value is not sensitive to the length-scale chosen to evaluate the ‘‘average’’ transverse flow $\langle u'_t \rangle$. In the case of parameters shown in Table 1, the density drop in the transverse direction is dominated by the cooling of the local temperature distribution in the transverse direction, and not so much by the change of the fugacity distribution. That is why we fitted here $\langle u'_t \rangle$ at the ‘‘surface radius’’ R_s . Note also that τ_0 could more properly be interpreted as the inverse of the longitudinal Hubble constant H_l , which is only an order of magnitude estimate of the mean freeze-out time, similarly to how the inverse of the present value of the Hubble constant in astrophysics provides only an order of magnitude estimate of the life-time of our Universe. The feasibility of directly fitting the transverse and longitudinal Hubble constants to data will be investigated in a subsequent publication.

Let us also note, that we have fitted the absolute normalized spectra for identified particles, and the normalization conditions were given by central chemical potentials μ_0 that were taken as free normalization parameters for each particle species. All these directly fitted parameters are

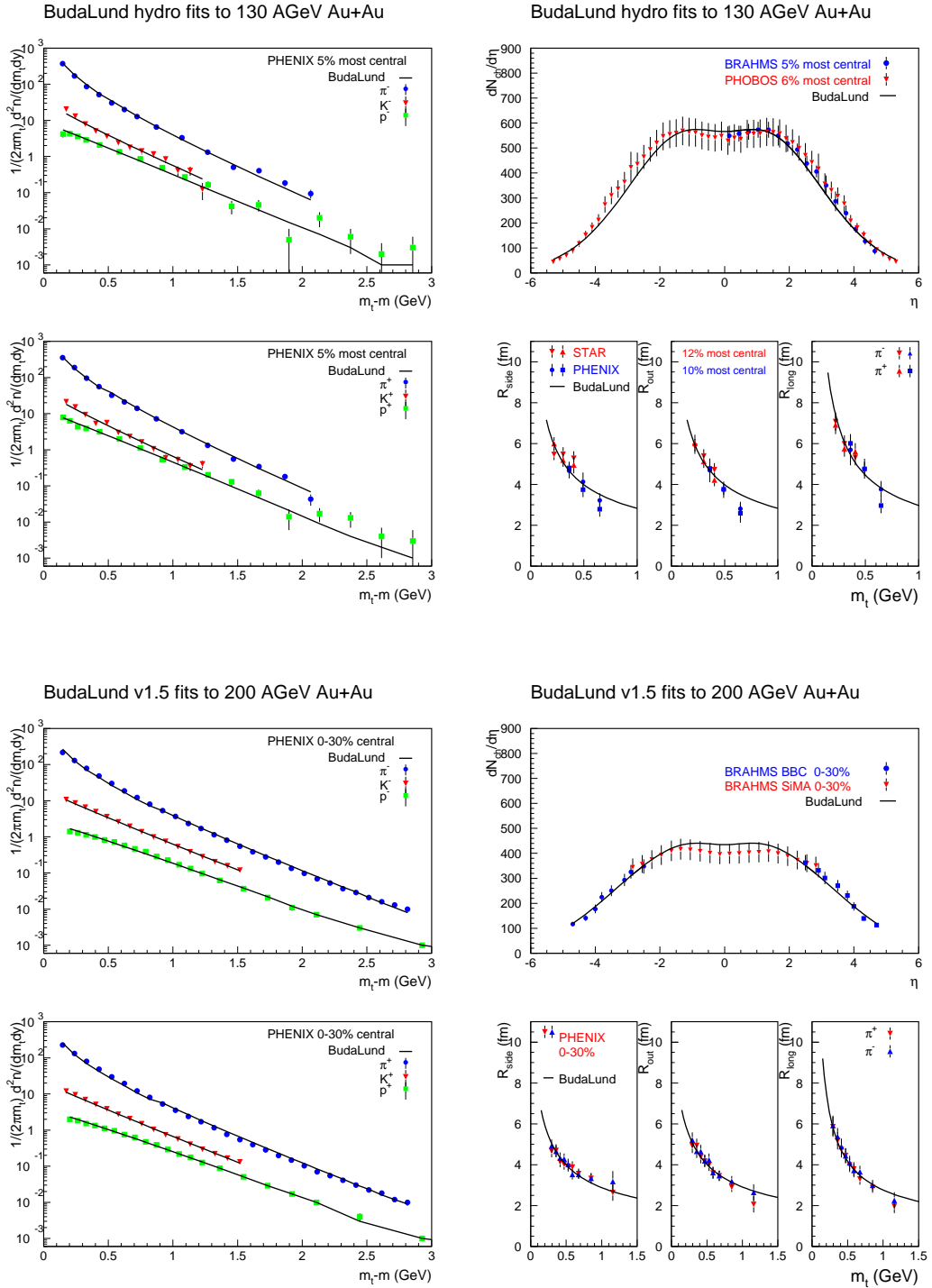


Figure 5.1: Fits to RHIC $\sqrt{s_{NN}} = 130$ and 200 GeV data

The upper four panels show a simultaneous Buda-Lund fit to 0-5(6) % central Au+Au data at $\sqrt{s_{NN}} = 130$ GeV, refs. [42, 43, 44, 45, 46]. The lower four panels show similar fits to 0-30 % central Au+Au data at $\sqrt{s_{NN}} = 200$ GeV, refs. [47, 48, 49]. Note that the identified particle spectra are published in more detailed centrality classes, but we recombined the 0-30% most central collisions so that the fitted spectra and radii be obtained in the same centrality class. The fit parameters are summarized in table 5.1.

BudaLund v1.5 fits to 200 AGeV Au+Au

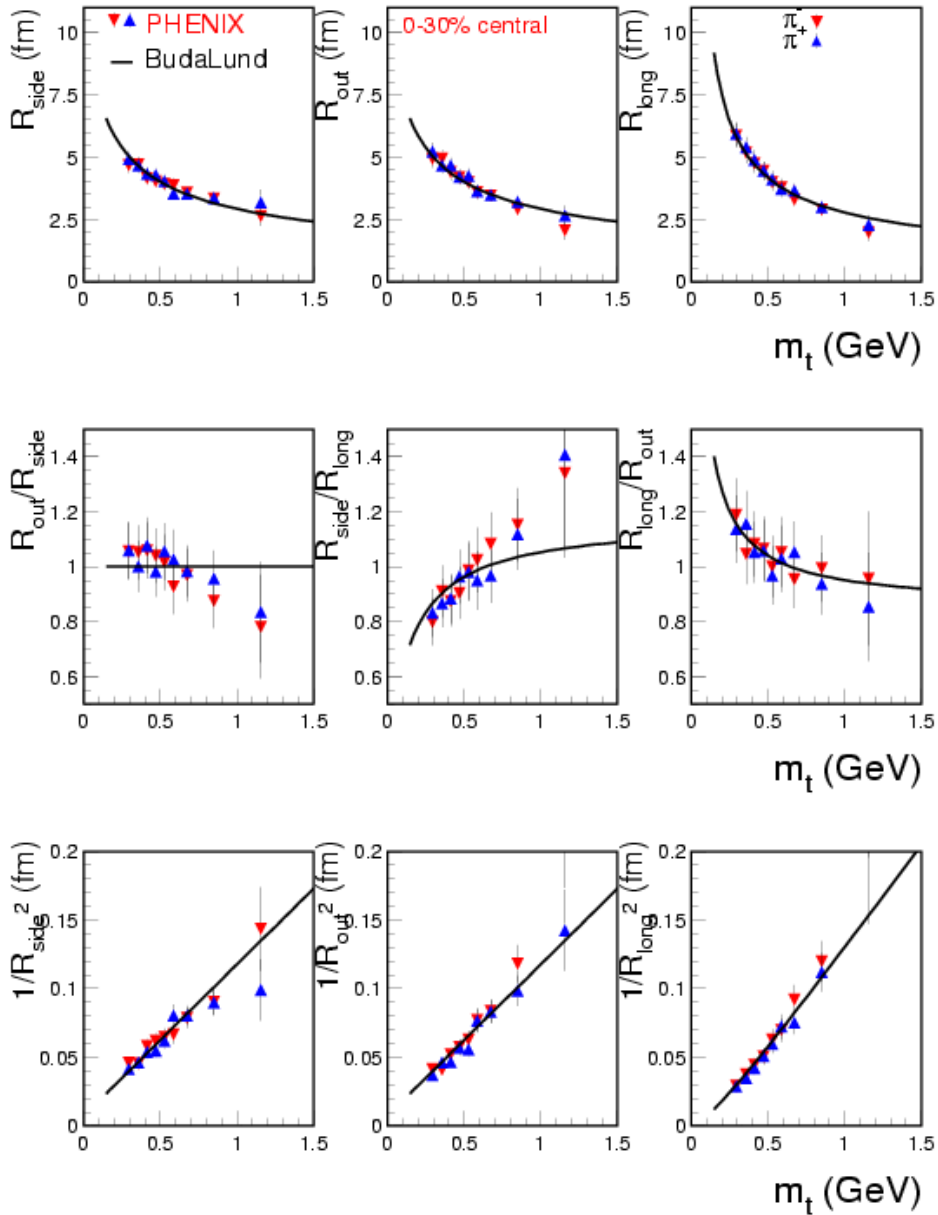


Figure 5.2: Various quantities calculated from the HBT radii

Top row shows the transverse mass dependence of the side, out and longitudinal HBT radii, the central line shows their pairwise ratio (usually only $R_{\text{out}}/R_{\text{side}}$ is shown) together with the Buda-Lund fits, vers. 1.5. The bottom line shows the inverse of the squared radii. The intercept of the curves in this row is within errors zero for the two transverse components, so the fugacity is within errors independent of the transverse coordinates. However, the intercept is nonzero in the longitudinal direction, which makes the fugacity (hence particle ratios) rapidity dependent. See also ref. [19] for a similar plot at $\sqrt{s_{\text{NN}}} = 130$ GeV.

made public at [50]. From these values, we have determined the net bariochemical potential as $\mu_B = \mu_p - \mu_{\bar{p}}$. Although this parameter is not directly fitted but calculated, we have included μ_B in Table 1, so that our results could be compared with other successful models of two-particle Bose-Einstein correlations at RHIC, namely the AMPT cascade [51], Tom Humanic's cascade [52], the blast-wave model [53, 54], the Hirano-Tsuda numerical hydro [55] and the Cracow "single freeze-out thermal model" [56, 57, 58].

Now, we are ready for the discussion of the results in table 5.1. In case of more central collisions at the lower RHIC energies, a well defined minimum was found, with accurate error matrix and a statistically acceptable fit quality, $\chi^2/\text{NDF} = 158/180$, that corresponds to a confidence level of 88 %. In the case of the less central but more energetic Au+Au collisions, the obtained χ^2/NDF fit is *too small*. Note that in these fits we added the systematic and statistical errors in quadrature, and this procedure is preliminary and has to be revisited before we can report on the final values of the fit parameters and determine their error bars. It could also be advantageous to analyze a more central data sample, or the centrality dependence of the radius parameters and the pseudorapidity distributions, or to fit additional data of STAR and PHOBOS too, so that the parameters of the Buda-Lund hydro model could be determined with smaller error bars.

At present, we find that $T_0 > T_c = 172 \pm 3$ MeV [22] by 3σ in case of the 0-30 % mostcentral Au+Au data at $\sqrt{s_{\text{NN}}} = 200$ GeV, while $T_0 > T_c$ by more than 5σ in case of the 0-5(6) % most central Au+Au data at $\sqrt{s_{\text{NN}}} = 130$ GeV. Thus this signal of a cross-over transition to quark deconfinement is not yet significant in the more energetic but less central Au+Au data sample, while it is significant at the more central, but less energetic sample. In this latter case of 130 GeV Au+Au data, R_G obviously became an irrelevant parameter, with $1/R_G \approx 0$. This is explicitly visible in Fig. 2 of ref. [19], where the last row indicates that the correlation radii are in the scaling limit and the fugacity distribution, $\exp[\mu(x)/T(x)]$ is independent of the transverse coordinates.

The Buda-Lund model predicted, see eqs. (53-58) in ref. [3] and also eqs. (26-28) in [33], that the linearity of the inverse radii as a function of m_t can be connected to the Hubble flow and the temperature gradients. The slopes are the same for side, out and longitudinal radii if the Hubble flow (and the temperature inhomogeneities) become direction independent. The intercepts of the linearly extrapolated m_t dependent inverse squared radii at $m_t = 0$ determine $1/R_G^2$, or the magnitude of corrections from the finite geometrical source sizes, that stem from the $\exp[\mu(x)/T(x)]$ terms. We can see on Fig. 2, that these corrections within errors vanish also in $\sqrt{s_{\text{NN}}} = 200$ Au+Au collisions at RHIC. This result is important, because it explains, why thermal and statistical models are successful at RHIC: if $\exp[\mu(x)/T(x)] = \exp(\mu_0/T_0)$, then this factor becomes an overall normalization factor, proportional to the particle abundances. Indeed, we found that when the finite size in the transverse direction is generated by the $T(x)$ distribution, the quality of the fit increased and we had no degenerate parameters in the fit any more. This is also the reason, why we interpret R_s , given by the condition that $T(r_x = r_y = R_s) = T_0/2$, as a "surface" radius: this is the scale where particle density drops.

Note that we have obtained similarly good description of these data if we require that the four-velocity field is a fully developed, three-dimensional Hubble flow, with $u^\nu = x^\nu/\tau$ as shown in section 5.4.

5.2.3 Conclusions

Table 5.1, figures 5.1 and 5.2 indicate that the Buda-Lund hydro model works well both at the lower and the higher RHIC energies, and gives a good quality description of the transverse mass dependence of the HBT radii. For the dynamical reason, see refs. [33] and [3]. In fact, even the time evolution of the entropy density can be solved from the fit results, $s(\tau) = s_0(\tau_0/\tau)^3$, which is the consequence of the Hubble flow, $u^\nu = x^\nu/\tau$, a well known solution of relativistic hydrodynamics, see also ref. [35]. This can be considered as the resolution of the RHIC HBT "puzzle", although a careful search of the literature indicates that this "puzzle" was only present in models that were not tuned to CERN SPS data [59].

We also observe that the central temperature is $T_0 = 214 \pm 7$ MeV in the most central Au+Au

collisions at $\sqrt{s_{NN}} = 130$ GeV, and we find here a net bariochemical potential of $\mu_B = 77 \pm 38$ MeV. Recent lattice QCD results indicate [22], that the critical temperature is within errors a constant of $T_c = 172 \pm 3$ MeV in the $0 \leq \mu_B \leq 300$ MeV interval. Our results clearly indicate (T, μ_B) values above this critical line, which is a significant, more than 5σ effect. The present level of precision and the currently fitted PHENIX and BRAHMS data set does not yet allow a firm conclusion about such an effect at $\sqrt{s_{NN}} = 200$ GeV, however, a similar behavior is seen on a 3 standard deviation level. This can be interpreted as a hint at quark deconfinement at $\sqrt{s_{NN}} = 200$ GeV at RHIC.

Finding similar parameters from the analysis of the pseudorapidity dependence of the elliptic flow, it was estimated in ref. [24] that 1/8th of the total volume is above the critical temperature in Au+Au collisions at $\sqrt{s_{NN}} = 130$ GeV, at the time when pions are emitted from the source. We interpret this result as an indication for quark deconfinement and a cross-over transition in Au+Au collisions at $\sqrt{s_{NN}} = 130$ GeV at RHIC. This result was signaled first in ref. [59] in a Buda-Lund analysis of the final PHENIX and STAR data on midrapidity spectra and Bose-Einstein correlations, but only at a three standard deviation level. By including the pseudorapidity distributions of BRAHMS and PHOBOS, the $T_0 \gg T_c$ effect became significant in most central Au+Au collisions at $\sqrt{s_{NN}} = 130$ GeV. We are looking forward to observe, what happens with the present signal in Au+Au collisions at $\sqrt{s_{NN}} = 200$ GeV, if we include STAR and PHOBOS data to the fitted sample.

The above observation of temperatures, that are higher than the critical one, is only an indication, with other words, an indirect proof for the production of a new phase, as the critical temperature is not extracted directly from the data, but taken from recent lattice QCD calculations.

More data are needed to clarify the picture of quark deconfinement at the maximal RHIC energies, for example the centrality dependence of the Bose-Einstein (HBT) radius parameters could provide very important insights.

5.3 Ellipsoidal Buda-Lund hydro model

5.3.1 Introduction

Ultra-relativistic collisions of almost fully ionized Au atoms are observed in four major experiments at the RHIC accelerator at the highest currently available colliding energies of $\sqrt{s_{NN}} = 200$ GeV to create new forms of matter that existed before in Nature only a few microseconds after the Big Bang, the creation of our Universe. At lower bombarding energies at CERN SPS, collisions of Pb nuclei were studied in the $\sqrt{s_{NN}} = 17$ GeV energy domain, with a similar motivation. If experiments are performed near to the production threshold of a new state of matter, perhaps only the most violent and most central collisions are sufficient to generate a transition to a new state. However, if the energy is well above the production threshold, new states of matter may appear already in the mid-central or even more peripheral collisions. Hence the deviation from axial symmetry of the observed single particle spectra and two-particle correlation functions can be utilized to characterize the properties of such new states.

The PHENIX, PHOBOS and STAR experiments at RHIC produced a wealth of information on the asymmetry of the particle spectra with respect to the reaction plane [25, 26, 27, 60, 61, 62], characterized by the second harmonic moment of the transverse momentum distribution, frequently referred to as the ‘‘elliptic flow’’ and denoted by v_2 . This quantity is determined, for various centrality selections, as a function of the transverse mass and particle type at mid-rapidity as well as a function of the pseudo-rapidity $\eta = 0.5 \log\left(\frac{|p|+p_z}{|p|-p_z}\right)$. Pseudorapidity measures the zenithal angle distribution in momentum space, but for particles with high momentum, $|p| \approx E_{|p|}$, it approximates the rapidity $y = 0.5 \log\left(\frac{E+p_z}{E-p_z}\right)$ that characterizes the longitudinal momentum distribution and transforms additively for longitudinal boosts, hence the rapidity density dn/dy is invariant for longitudinal boosts. The PHOBOS collaboration found [26], that $v_2(\eta)$ is a strongly decreasing function of $|\eta|$, which implies that the concept of boost-invariance, suggested by Bjorken in ref. [63] to characterize the physics of very high energy heavy ion collisions, cannot

be applied to characterize the hadronic final state of Au+Au collisions at RHIC. A similar conclusion can be drawn from the measurement of the inhomogeneous (pseudo)rapidity $dn/d\eta$ and dn/dy distributions of charged particle production at RHIC by both the BRAHMS [64] and PHOBOS [45] collaborations, proving the lack of boost-invariance in these reactions, as $dn/dy \neq \text{const}$ at RHIC. Although many models describe successfully the transverse momentum dependence of the elliptic flow at mid-rapidity, $v_2(p_t, \eta = 0)$, see ref. [65] for a recent review on this topic, to our best knowledge and an up-to-date scanning of the available high energy and nuclear physics literature, no model has yet been able to reproduce the measured pseudo-rapidity dependence of the elliptic flow at RHIC.

Hence we present here the first successful attempt to describe the pseudo-rapidity dependence of the elliptic flow $v_2(\eta)$ at RHIC. Our tool is the Buda-Lund hydrodynamic model [3, 36], which we extend here from axial to ellipsoidal symmetry. The Buda-Lund hydro model takes into account the finite longitudinal extension of the particle emitting source, and we show here how the finite longitudinal size of the source leads naturally to a v_2 that decreases with increasing values of $|\eta|$, in agreement with the data. We tuned the parameters by hand to describe simultaneously the pseudorapidity and the transverse momentum dependence of the elliptic flow, with a parameter set, that reproduces [19] the single-particle transverse momentum and pseudo-rapidity distributions as well as the radius parameters of the two-particle Bose-Einstein correlation functions, or HBT radii, in case when the orientation of the event plane is averaged over. All these benefits are achieved with the help of transparent and simple analytic formulas, that are natural extensions of our earlier results to the case of ellipsoidal symmetry.

5.3.2 Buda-Lund hydro for ellipsoidal expansions

The Buda-Lund model is defined with the help of its emission function $S(x, p)$, where $x = (t, r_x, r_y, r_z)$ is a point in space-time and $p = (E, p_x, p_y, p_z)$ stands for the four-momentum. To take into account the effects of long-lived resonances, we utilize the core-halo model [37], and characterize the system with a hydrodynamically evolving core and a halo of the decay products of the long-lived resonances. Within the core-halo picture, the measured intercept parameter λ_* of the two-particle Bose-Einstein correlation function is related [37] to the strength of the relative contribution of the core to the total particle production at a given four-momentum,

$$S(x, p) = S_c(x, p) + S_h(x, p), \quad \text{and} \quad (5.33)$$

$$S_c(x, p) = \sqrt{\lambda_*} S(x, p). \quad (5.34)$$

Based on the success of the Buda-Lund hydro model to describe $Au + Au$ collisions at RHIC [19, 66], $Pb + Pb$ collisions at CERN SPS [67] and $h + p$ reactions at CERN SPS [29, 68], we assume that the core evolves in a hydrodynamical manner,

$$S_c(x, p) d^4x = \frac{g}{(2\pi)^3} \frac{p^\mu d^4\Sigma_\mu(x)}{B(x, p) + s_q}, \quad (5.35)$$

where g is the degeneracy factor ($g = 1$ for identified pseudoscalar mesons, $g = 2$ for identified spin=1/2 baryons), and $p^\mu d^4\Sigma_\mu(x)$ is a generalized Cooper-Frye term, describing the flux of particles through a distribution of layers of freeze-out hypersurfaces, $B(x, p)$ is the (inverse) Boltzmann phase-space distribution, and the term s_q is determined by quantum statistics, $s_q = 0, -1$, and $+1$ for Boltzmann, Bose-Einstein and Fermi-Dirac distributions, respectively.

For a hydrodynamically expanding system, the (inverse) Boltzmann phase-space distribution is

$$B(x, p) = \exp\left(\frac{p^\nu u_\nu(x)}{T(x)} - \frac{\mu(x)}{T(x)}\right). \quad (5.36)$$

We will utilize some ansatz for the shape of the flow four-velocity, $u_\nu(x)$, chemical potential, $\mu(x)$, and temperature, $T(x)$ distributions. Their form is determined with the help of recently found exact solutions of hydrodynamics, both in the relativistic [34, 35, 69] and in the non-relativistic cases [31, 32, 33], with the conditions that these distributions are characterized by mean values

and variances, and that they lead to (simple) analytic formulas when evaluating particle spectra and two-particle correlations.

The generalized Cooper-Frye prefactor is determined from the assumption that the freeze-out happens, with probability $H(\tau)d\tau$, at a hypersurface characterized by $\tau = \text{const}$ and that the proper-time measures the time elapsed in a fluid element that moves together with the fluid, $d\tau = u^\mu(x)dx_\mu$. We parameterize this hypersurface with the coordinates (r_x, r_y, r_z) and find that $d^3\Sigma^\mu(x|\tau) = u^\mu(x)d^3x/u^0(x)$. Using $\partial_t\tau|_r = u^0(x)$ we find that in this case the generalized Cooper-Frye prefactor is

$$p^\mu d^4\Sigma_\mu(x) = p^\mu u_\mu(x)H(\tau)d^4x, \quad (5.37)$$

This finding generalizes the result of ref. [58] from the case of a spherically symmetric Hubble flow to anisotropic, direction dependent Hubble flow distributions.

From the analysis of CERN SPS and RHIC data [19, 66, 67], we find that the proper-time distribution in heavy ion collisions is rather narrow, and $H(\tau)$ can be well approximated with a Gaussian representation of the Dirac-delta distribution,

$$H(\tau) = \frac{1}{(2\pi\Delta\tau^2)^{1/2}} \exp\left(-\frac{(\tau - \tau_0)^2}{2\Delta\tau^2}\right), \quad (5.38)$$

with $\Delta\tau \ll \tau_0$.

Based on the success of the Buda-Lund hydro model to describe the axially symmetric collisions, we develop an ellipsoidally symmetric extension of the Buda-Lund model, that goes back to the successful axially symmetric case [3, 19, 36, 66, 67] if axial symmetry is restored, corresponding to the $X = Y$ and $\dot{X} = \dot{Y}$ limit.

We specify a fully scale invariant, relativistic form, which reproduces known non-relativistic hydrodynamic solutions too, in the limit when the expansion is non-relativistic. Both in the relativistic and the non-relativistic cases, the ellipsoidally symmetric, self-similarly expanding hydrodynamical solutions can be formulated in a simple manner, using a scaling variable s and a corresponding four-velocity distribution u^μ , that satisfy

$$u^\mu \partial_\mu s = 0, \quad (5.39)$$

which means that s is a good scaling variable if it's co-moving derivative vanishes [34, 35]. This equation couples the scaling variable s and the flow velocity distribution. It is convenient to introduce the dimensionless, generalized space-time rapidity variables (η_x, η_y, η_z) , defined by the identification of

$$(\sinh \eta_x, \sinh \eta_y, \sinh \eta_z) = (r_x \frac{\dot{X}}{X}, r_y \frac{\dot{Y}}{Y}, r_z \frac{\dot{Z}}{Z}). \quad (5.40)$$

Here (X, Y, Z) are the characteristic sizes (for example, the lengths of the major axis) of the expanding ellipsoid, that depend on proper-time τ and their derivatives with respect to proper-time are denoted by $(\dot{X}, \dot{Y}, \dot{Z})$. The distributions will be given in this η_i variables, but the integral-form is the standard $d^4x = dt dr_x dr_y dr_z$, so we have to take a Jacobi-determinant into account. Eq. (5.39) is satisfied by the choice of

$$s = \frac{\cosh \eta_x - 1}{\dot{X}_f^2} + \frac{\cosh \eta_y - 1}{\dot{Y}_f^2} + \frac{\cosh \eta_z - 1}{\dot{Z}_f^2}, \quad (5.41)$$

$$u^\mu = (\gamma, \sinh \eta_x, \sinh \eta_y, \sinh \eta_z), \quad (5.42)$$

and from here on $(\dot{X}_f, \dot{Y}_f, \dot{Z}_f) = (\dot{X}(\tau_0), \dot{Y}(\tau_0), \dot{Z}(\tau_0)) = (\dot{X}_1, \dot{X}_2, \dot{X}_3)$, assuming that the rate of expansion is constant in the narrow proper-time interval of the freeze-out process. The above form has the desired non-relativistic limit,

$$s \rightarrow \frac{r_x^2}{2\dot{X}_f^2} + \frac{r_y^2}{2\dot{Y}_f^2} + \frac{r_z^2}{2\dot{Z}_f^2}, \quad (5.43)$$

where again $(X_f, Y_f, Z_f) = (X(\tau_0), Y(\tau_0), Z(\tau_0)) = (X_1, X_2, X_3)$. From now on, we drop subscript f . From the normalization condition of $u^\mu(x)u_\mu(x) = 1$ we obtain that:

$$\gamma = \sqrt{1 + \sinh^2 \eta_x + \sinh^2 \eta_y + \sinh^2 \eta_z}, \quad (5.44)$$

For the fugacity distribution we assume a shape, that leads to Gaussian profile in the non-relativistic limit,

$$\frac{\mu(x)}{T(x)} = \frac{\mu_0}{T_0} - s, \quad (5.45)$$

corresponding to the solution discussed in refs. [31, 32, 70]. We assume that the temperature may depend on the position as well as on proper-time. We characterize the inverse temperature distribution similarly to the shape used in the axially symmetric model of ref. [3, 36], and discussed in the exact hydro solutions of refs [31, 32],

$$\frac{1}{T(x)} = \frac{1}{T_0} \left(1 + \frac{T_0 - T_s}{T_s} s \right) \left(1 + \frac{T_0 - T_e}{T_e} \frac{(\tau - \tau_0)^2}{2\Delta\tau^2} \right), \quad (5.46)$$

where T_0 , T_s and T_e are the temperatures of the center, and the surface at the mean freeze-out time τ_0 , while T_e corresponds to the temperature of the center after most of the particle emission is over (cooling due to evaporation and expansion). Sudden emission corresponds to $T_e = T_0$, and the $\Delta\tau \rightarrow 0$ limit. It's convenient to introduce the following quantities:

$$a^2 = \frac{T_0 - T_s}{T_s} = \left\langle \frac{\Delta T}{T} \right\rangle_r, \quad (5.47)$$

$$d^2 = \frac{T_0 - T_e}{T_e} = \left\langle \frac{\Delta T}{T} \right\rangle_t. \quad (5.48)$$

5.3.3 Integration and saddlepoint approximation

The observables can be calculated analytically from the Buda-Lund hydro model, using a saddle-point approximation in the integration. This approximation is exact both in the Gaussian and the non-relativistic limit, and if $p^\nu u_\nu / T \gg 1$ at the point of maximal emittivity. In this approximation, the emission function looks like:

$$S(x, k) d^4x = \frac{g}{(2\pi)^3} \frac{p^\mu u_\mu(x_s) H(\tau_s)}{B(x_s, p) + s_q} \exp(-R_{\mu\nu}^{-2} (x - x_s)^\mu (x - x_s)^\nu) d^4x, \quad (5.49)$$

where

$$R_{\mu\nu}^{-2} = \partial_\mu \partial_\nu (-\ln(S_0))_s, \quad (5.50)$$

and x_ν stands here for (τ, r_x, r_y, r_z) . In the integration, a Jacobian $\frac{\tau}{t}$ has to be introduced when changing the integration measure from d^4x to $d\tau d^3x$.

The position of the saddle-point can be calculated from the equation

$$\partial_\mu (-\ln(S_0))(x_s, p) = 0. \quad (5.51)$$

Here we introduced S_0 , as the 'narrow' part of the emission function:

$$S_0(x, p) = \frac{H(\tau)}{B(x, p) + s_q}. \quad (5.52)$$

In general, we get the following saddle-point equations in $(\tau, \eta_x, \eta_y, \eta_z)$ coordinates:

$$\tau_s = \tau_0, \quad (5.53)$$

$$\sinh \eta_{i,s} = \frac{p_i \dot{X}_i^2 \cosh \eta_{i,s}}{T(x_s) \left(1 + a^2 \frac{p_\mu u^\mu(x_s)}{T_0} \right) + p_0 \frac{\cosh \eta_{i,s}}{\gamma(x_s)} \dot{X}_i^2}. \quad (5.54)$$

The system of equations (5.54) can be solved efficiently for the saddle-point positions $\eta_{s,i}$ using a successive approximation. This method was implemented in our data fitting procedure.

For the distribution widths, the exact result is:

$$R_{ij}^{-2} = \frac{B(x_s, p)}{B(x_s, p) + s_q} \left(\frac{\dot{X}_i \dot{X}_j}{X_i X_j} \frac{1}{\cosh \eta_{i,s} \cosh \eta_{j,s}} \right) \frac{\partial^2 b}{\partial \eta_i \partial \eta_j} \Big|_s, \quad (5.55)$$

$$R_{0,0}^{-2} = \frac{t_s}{\tau_s} \frac{1}{\Delta \tau_*^2} = \frac{1}{\Delta \tau^2} + \frac{B(x_s, p)}{B(x_s, p) + s_q} \frac{\partial^2 b}{\partial \tau^2} \Big|_s \quad (5.56)$$

$$R_{i,0}^{-2} = 0, \quad \text{with,} \quad (5.57)$$

$$\begin{aligned} \frac{\partial^2 b}{\partial \eta_{i,s} \partial \eta_j} \Big|_s &= \delta_{ij} \left[\frac{\cosh \eta_{i,s}}{\dot{X}_i^2} + \frac{\cosh \eta_{i,s} a^2}{\dot{X}_i^2 T_0} p_\mu u^\mu(x_s) \right. \\ &+ \frac{1}{T(x_s)} \left(\frac{E}{\gamma(x_s)} \cosh(2\eta_{i,s}) - p_i \sinh \eta_{i,s} \right) \Big] + \\ &+ \frac{a^2 \sinh \eta_{i,s}}{2T_0 \dot{X}_i^2} \left(\frac{E}{\gamma(x_s)} \sinh(2\eta_{i,s}) - p_i \cosh \eta_{i,s} \right) + \\ &+ \frac{a^2 \sinh \eta_{j,s}}{2T_0 \dot{X}_j^2} \left(\frac{E}{\gamma(x_s)} \sinh(2\eta_{j,s}) - p_j \cosh \eta_{j,s} \right) - \\ &- \frac{E}{4T(x_s) \gamma(x_s)^3} \sinh(2\eta_{i,s}) \sinh(2\eta_{j,s}), \quad \text{and} \end{aligned} \quad (5.59)$$

$$\frac{\partial^2 b}{\partial \tau^2} \Big|_s = \frac{p^\mu u^\mu(x)}{T_0} (1 + a^2 s). \quad (5.60)$$

We introduced here the exponent

$$b(x_s, p) = \log B(x_s, p). \quad (5.61)$$

For clarity, we give the resulting analytic expressions only in the case, where $r_{x,s}/X \ll 1$, $r_{y,s}/Y \ll 1$, and $\eta_s - y \ll \Delta \eta = \dot{Z}$. In this case, we expand the parts of the emission function into a Taylor series of second order. First:

$$\begin{aligned} \frac{u^\mu(x) p_\mu}{T(x)} &= \frac{m_t \cosh(\eta_z - y)}{T_0} \times \\ &\times \left(1 + a^2 \left(\frac{r_x^2}{2X^2} + \frac{r_y^2}{2Y^2} + \frac{r_z^2}{2Z^2} \right) + d^2 \frac{(\tau - \tau_0)^2}{2\tau_0^2} + r_x^2 \frac{\dot{X}^2}{2X^2} + r_y^2 \frac{\dot{Y}^2}{2Y^2} \right) \\ &- \frac{p_x \dot{X}}{T_0 X} r_x - \frac{p_y \dot{Y}}{T_0 Y} r_y \end{aligned} \quad (5.62)$$

This way, we get:

$$\begin{aligned} b(x, p) &= \frac{m_t \cosh(\eta_z - y)}{T_0} \times \\ &\times \left(1 + a^2 \left(\frac{r_x^2}{2X^2} + \frac{r_y^2}{2Y^2} + \frac{r_z^2}{2Z^2} \right) + d^2 \frac{(\tau - \tau_0)^2}{2\tau_0^2} + r_x^2 \frac{\dot{X}^2}{2X^2} + r_y^2 \frac{\dot{Y}^2}{2Y^2} \right) \\ &- \frac{p_x \dot{X}}{T_0 X} r_x - \frac{p_y \dot{Y}}{T_0 Y} r_y - \frac{\mu_0}{T_0} + \frac{r_x^2}{2X^2} + \frac{r_y^2}{2Y^2} + \frac{r_z^2}{2Z^2} \end{aligned} \quad (5.63)$$

In this case, we get the following for the saddle-point and the distribution widths:

$$\eta_{z,s} - y = \frac{\frac{m_t}{T_0} \sinh y}{\frac{m_t}{T_0} \left(1 + \frac{a^2}{Z^2}\right) \cosh y + \frac{1}{Z^2}}, \quad (5.64)$$

$$\frac{r_{i,s}}{Y} = \frac{\frac{p_i}{T_0} \dot{X}_i}{1 + \frac{X_i^2}{R_{T,i}^2}} \quad \text{for } i = 1 \dots 2, \quad (5.65)$$

$$\frac{1}{\Delta \eta_*^2} = \frac{B(x_s, p)}{B(x_s, p) + s} \left(\frac{1}{Z^2} + \frac{1}{\Delta \eta_T^2} \right), \quad (5.66)$$

$$\frac{1}{R_{*,i}^2} = \frac{B(x_s, p)}{B(x_s, p) + s} \left(\frac{1}{X_i^2} + \frac{1}{R_{T,i}^2} \right), \quad (5.67)$$

$$\frac{1}{\Delta \tau_*^2} = \frac{1}{\Delta \tau^2} + \frac{B(x_s, p)}{B(x_s, p) + s} \frac{1}{\Delta \tau_T^2}. \quad (5.68)$$

Equations (5.66)–(5.68) imply, that the HBT radii are dominated by the smaller of the thermal and the geometrical length scales in all directions. Note that the geometrical scales stem from the density distribution, governed by the fugacity term $\exp(\mu(x)/T(x))$, while the thermal lengths stem from the local thermal momentum distribution $\exp(-p^\mu u_\mu(x)/T(x))$, and in this limit they are defined as

$$\frac{1}{\Delta \tau_T^2} = \frac{m_t}{T_0} \cosh(\eta_{z,s} - y) \frac{d^2}{\tau_0^2}, \quad (5.69)$$

$$\frac{1}{\Delta \eta_T^2} = \frac{m_t}{T_0} \cosh(\eta_{z,s} - y) \left(1 + \frac{a^2}{Z^2} \right), \quad (5.70)$$

$$\frac{1}{R_{T,i}^2} = \frac{m_t}{T_0} \cosh(\eta_{z,s} - y) \left(\frac{a^2}{X_i^2} + \frac{\dot{X}_i^2}{X_i^2} \right). \quad (5.71)$$

In the simplest case, where all three $\eta_{i,s}$ are small:

$$\frac{r_{i,s}}{X_i} = \frac{\frac{p_i}{T_0} \dot{X}_i}{1 + \frac{X_i^2}{R_{T,i}^2}}, \quad \text{for } i = x, y, z, \quad (5.72)$$

$$\frac{1}{R_{i,i}^2} = \frac{B(x_s, p)}{B(x_s, p) + s_q} \left(\frac{1}{X_i^2} + \frac{1}{R_{T,i}^2} \right), \quad (5.73)$$

$$\frac{1}{R_{0,0}^2} = \frac{1}{\Delta \tau_*^2} = \frac{1}{\Delta \tau^2} + \frac{B(x_s, p)}{B(x_s, p) + s} \frac{1}{\Delta \tau_T^2}. \quad (5.74)$$

In the above limit the thermal lengths are

$$\frac{1}{\Delta \tau_T^2} = \frac{m_t}{T_0} \frac{d^2}{\tau_0^2}, \quad (5.75)$$

$$\frac{1}{R_{T,i}^2} = \frac{m_t}{T_0} \left(\frac{a^2}{X_i^2} + \frac{\dot{X}_i^2}{X_i^2} \right). \quad (5.76)$$

5.4 Results from the ellipsoidal model

5.4.1 The invariant momentum distribution

The invariant momentum distribution can be calculated as

$$N_1(p) = \int d^4x S(x, p) = \frac{1}{\sqrt{\lambda_*}} \int d^4x S_c(p, x). \quad (5.77)$$

Then the invariant momentum distribution is

$$N_1(p) = \frac{1}{\sqrt{\lambda_*}} \frac{g}{(2\pi)^3} p_\mu u^\mu(x_s) \frac{\Delta\tau_*}{\Delta\tau} [\det R_{i,j}^2]^{1/2} \frac{1}{B(x_s, p) + s_q}.$$

It can be expressed on a more simple way:

$$N_1(p) = \frac{g}{(2\pi)^3} \bar{E} \bar{V} \bar{C} \frac{1}{\exp b(x_s, p) + s_q}, \quad (5.78)$$

where

$$\bar{E} = p_\mu u^\mu(x_s), \quad (5.79)$$

$$\bar{V} = (2\pi)^{3/2} \frac{\Delta\tau_*}{\Delta\tau} [\det R_{i,j}^2]^{1/2}, \quad (5.80)$$

$$\bar{C} = \frac{1}{\sqrt{\lambda_*}} \frac{\tau_s}{t_s}. \quad (5.81)$$

Let us investigate the structure of this invariant momentum distribution. If we evaluate the exponent $b(x_s, p)$ in the limit, where the saddle-point coordinates are all small, (except η_z , which is written from here as η simply):

$$\begin{aligned} b(x_s, p) &= -\frac{r_{x,s}}{2R_{*,x}^2} - \frac{r_{y,s}}{2R_{*,y}^2} + \frac{\eta_s^2}{2} \left(\frac{m_t}{T_0} \cosh(\eta_s - y) \frac{a^2}{\dot{Z}^2} + \frac{1}{\dot{Z}^2} \right) + \\ &+ \frac{m_t}{T_0} \cosh(\eta_s - y) - \frac{\mu_0}{T_0}. \end{aligned} \quad (5.82)$$

Or, in an other form

$$b(x_s, p) = \frac{p_x^2}{2\bar{m}_t T_{*,x}} + \frac{p_y^2}{2\bar{m}_t T_{*,y}} - \frac{p_t^2}{2\bar{m}_t T_0} + \frac{\eta_s^2}{2} \left(\frac{\bar{m}_t a^2}{T_0 \dot{Z}^2} + \frac{1}{\dot{Z}^2} \right) + \frac{\bar{m}_t}{T_0} - \frac{\mu_0}{T_0}, \quad (5.83)$$

where $\bar{m}_t = m_t \cosh(\eta_s - y)$ and the direction dependent slope parameters are

$$T_{*,x} = T_0 + \bar{m}_t \dot{X}^2 \frac{T_0}{T_0 + \bar{m}_t a^2}, \quad (5.84)$$

$$T_{*,y} = T_0 + \bar{m}_t \dot{Y}^2 \frac{T_0}{T_0 + \bar{m}_t a^2}. \quad (5.85)$$

It is useful to show the low-rapidity limit, where η is small, because it helps to understand the behavior of our formulas, although in data fitting we used the exact, more complicated formulas. The Boltzmann-exponent b is in this low-rapidity limit the following:

$$b(x_s, p) = \frac{p_x^2}{2\bar{m}_t T_{*,x}} + \frac{p_y^2}{2\bar{m}_t T_{*,y}} + \frac{p_z^2}{2m_t T_{*,z}} + \frac{m_t}{T_0} - \frac{p_t^2}{2m_t T_0} - \frac{\mu_0}{T_0}, \quad (5.86)$$

where

$$T_{*,z} = T_0 + m_t \dot{Y}^2 \frac{T_0}{T_0 + m_t a^2}. \quad (5.87)$$

In the limit when the possibility of a temperature inhomogeneity on the freeze-out hypersurface is neglected, we can substitute $a = 0$. Using a non-relativistic approximation of $\bar{m}_t \approx m$, we recover the recent result of ref. [70] for the mass dependence of the slope parameters of the single-particle spectra:

$$T_{*,x} = T_0 + m \dot{X}^2, \quad (5.88)$$

$$T_{*,y} = T_0 + m \dot{Y}^2, \quad (5.89)$$

$$T_{*,z} = T_0 + m \dot{Z}^2. \quad (5.90)$$

5.4.2 The elliptic flow

The elliptic flow is defined as the second harmonic momentum of the invariant momentum distribution, or the second Fourier-coefficient of $N_1(\varphi)$:

$$N_1 = \frac{d^3 n}{dp_z p_t dp_t d\varphi} = \frac{d^2 n}{2\pi dp_z p_t dp_t} \left[1 + 2 \sum_{n=1}^{\infty} v_n \cos(n\varphi) \right] \quad (5.91)$$

Note, that $b(x_s, p)$ is the only part of the IMD, that is explicitly angle dependent, so

$$\begin{aligned} N_1(p) &\sim \exp\left(-\frac{p_x^2}{2\bar{m}_t T_{*,x}} - \frac{p_y^2}{2\bar{m}_t T_{*,y}}\right) = \\ &= \exp\left(-\frac{p_t^2}{2\bar{m}_t T_{eff}} + \left(\frac{p_t^2}{2\bar{m}_t T_{*,x}} - \frac{p_t^2}{2\bar{m}_t T_{*,y}}\right) \frac{\cos(2\varphi)}{2}\right), \end{aligned} \quad (5.92)$$

where

$$T_{eff} = \frac{1}{2} \left(\frac{1}{T_{*,x}} + \frac{1}{T_{*,y}} \right). \quad (5.93)$$

So, we can easily extract the angular dependencies. Let us compute v_2 by integrating on the angle:

$$v_2 = \frac{I_1(w)}{I_0(w)}, \quad (5.94)$$

where

$$w = \frac{p_t^2}{4\bar{m}_t} \left(\frac{1}{T_{*,y}} - \frac{1}{T_{*,x}} \right). \quad (5.95)$$

Generally, we get from the definition (eq. 5.91) the following equations:

$$v_{2n} = \frac{I_n(w)}{I_0(w)}, \quad \text{and} \quad (5.96)$$

$$v_{2n+1} = 0. \quad (5.97)$$

As first and the third flow coefficients vanish in this case, a tilt angle ϑ has to be introduced to get results compatible with observations, as discussed in the subsequent parts.

Note that for large rapidities, $|\eta_s - y|$ becomes also large, so $\bar{m}_t = m_t \cosh(\eta_s - y)$ diverges and

$$\frac{1}{T_{*,y}} - \frac{1}{T_{*,x}} \rightarrow \frac{1}{T_0} \left(\frac{a^2}{a^2 + \dot{Y}^2} - \frac{a^2}{a^2 + \dot{X}^2} \right), \quad (5.98)$$

hence

$$w \xrightarrow[\eta \rightarrow \infty]{} 0. \quad (5.99)$$

Thus we find a natural mechanism for the decrease of v_2 for increasing values of $|y|$, as in this limit, $v_2 \rightarrow I_1(0)/I_0(0) = 0$.

5.4.3 The correlation function

Now, let us calculate the correlation function! This has the form

$$C(Q, p) = 1 + \frac{\left| \tilde{S}(Q, p) \right|^2}{\left| \tilde{S}(0, p) \right|^2} = 1 + \lambda_* \frac{\left| \tilde{S}_c(Q, p) \right|^2}{\left| \tilde{S}_c(0, p) \right|^2}, \quad (5.100)$$

where

$$\tilde{S}(Q, p) = \int S(x, p) e^{iQx} d^4x, \quad \text{and} \quad (5.101)$$

$$\tilde{S}_c(Q, p) = \int S_c(x, p) e^{iQx} d^4x. \quad (5.102)$$

From here on, we don't write out the p dependence. The result for the correlation function is, with this notation:

$$C(Q) = 1 + \lambda_* e^{-R_{\mu\nu}^2 Q^\mu Q^\nu}. \quad (5.103)$$

In the physically interesting case, the expansion is predominantly longitudinal. So, let us consider the case, when the emission function is characterized in terms of the variables (τ, η, r_x, r_y) , similarly to the axially symmetric case of the Buda-Lund model. If we solve the saddle-point equations in the $r_{x,s}/X \ll 1$, $r_{y,s}/Y \ll 1$, and $\eta_s - y \ll \Delta\eta = \dot{Z}$ limit, then the correlation function has the following diagonal form:

$$C(Q) = 1 + \lambda_* e^{-Q_\tau^2 \Delta\tau_*^2 - Q_x^2 R_{*,x}^2 - Q_y^2 R_{*,y}^2 - Q_z^2 \tau_0^2 \Delta\eta_*^2}. \quad (5.104)$$

Then, we use the usual formalism:

$$Q_\tau = Q_0 \cosh \eta_s - Q_z \sinh \eta_s, \quad (5.105)$$

$$Q_\eta = -Q_0 \sinh \eta_s + Q_z \cosh \eta_s. \quad (5.106)$$

From the mass-shell constraint, $p_1^2 = p_2^2 = m^2$, one finds that

$$Q_0 = \beta_x Q_x + \beta_y Q_y + \beta_z Q_z. \quad (5.107)$$

So, if we write the correlation function in the usual

$$C(Q) = 1 + \lambda_* \exp \left(- \sum_{i,j=x,y,z} R_{i,j}^2 Q_i Q_j \right) \quad (5.108)$$

form, then the radii are:

$$R_x^2 = R_{*,x}^2 + \beta_x^2 (\Delta\tau_*^2 \cosh^2 \eta_s + \tau_0^2 \Delta\eta_*^2 \sinh^2 \eta_s), \quad (5.109)$$

$$R_y^2 = R_{*,y}^2 + \beta_y^2 (\Delta\tau_*^2 \cosh^2 \eta_s + \tau_0^2 \Delta\eta_*^2 \sinh^2 \eta_s), \quad (5.110)$$

$$R_z^2 = \Delta\tau_*^2 (\sinh \eta_s - \beta_z \cosh \eta_s)^2 + \tau_0^2 \Delta\eta_*^2 (\cosh \eta_s - \beta_z \sinh \eta_s)^2, \quad (5.111)$$

$$2R_{x,z}^2 = -(\Delta\tau_*^2 + \tau_0^2 \Delta\eta_*^2) \beta_x \cosh \eta_s \sinh \eta_s + \beta_x \beta_z (\Delta\tau_*^2 \cosh^2 \eta_s + \tau_0^2 \Delta\eta_*^2 \sinh^2 \eta_s), \quad (5.112)$$

$$2R_{y,z}^2 = -(\Delta\tau_*^2 + \tau_0^2 \Delta\eta_*^2) \beta_y \cosh \eta_s \sinh \eta_s + \beta_y \beta_z (\Delta\tau_*^2 \cosh^2 \eta_s + \tau_0^2 \Delta\eta_*^2 \sinh^2 \eta_s), \quad (5.113)$$

$$2R_{x,y}^2 = \beta_x \beta_y (\Delta\tau_*^2 \cosh^2 \eta_s + \tau_0^2 \Delta\eta_*^2 \sinh^2 \eta_s). \quad (5.114)$$

Then we make the coordinate-transformation (see Fig. 5.3):

$$Q_x = Q'_x \cos \vartheta - Q'_z \sin \vartheta = Q'_o \cos \varphi \cos \vartheta - Q'_s \sin \varphi \cos \vartheta - Q'_l \sin \vartheta, \quad (5.115)$$

$$Q_y = Q'_y = Q'_s \cos \varphi + Q'_o \sin \varphi, \quad (5.116)$$

$$Q_z = Q'_z \cos \vartheta + Q'_x \sin \vartheta = Q'_l \cos \vartheta + Q'_o \cos \varphi \sin \vartheta - Q'_s \sin \varphi \sin \vartheta. \quad (5.117)$$

After that, we get the following radii:

$$R_o'^2 = R_x'^2 \cos^2 \varphi + R_y'^2 \sin^2 \varphi + R_{x,y}^2 \sin(2\varphi), \quad (5.118)$$

$$R_s'^2 = R_x'^2 \sin^2 \varphi + R_y'^2 \cos^2 \varphi - R_{x,y}^2 \sin(2\varphi), \quad (5.119)$$

$$R_l'^2 = R_x^2 \sin^2 \vartheta + R_z^2 \cos^2 \vartheta - R_{x,z}^2 \sin(2\vartheta), \quad (5.120)$$

$$2R_{o,s}'^2 = -R_x^2 \sin(2\varphi) + R_y^2 \sin(2\varphi) - 2R_{x,y}^2 \cos(2\varphi), \quad (5.121)$$

$$2R_{s,l}'^2 = (R_x^2 \sin(2\vartheta) - R_z^2 \sin(2\vartheta) - 2R_{x,z}^2 \cos(2\vartheta)) \sin \varphi - (2R_{x,y}^2 \sin \vartheta - 2R_{y,z}^2 \cos \vartheta) \sin \varphi, \quad (5.122)$$

$$2R_{l,o}'^2 = (R_z^2 \sin(2\vartheta) - R_x^2 \sin(2\vartheta) + 2R_{x,z}^2 \cos(2\vartheta)) \cos \varphi - (2R_{x,y}^2 \sin \vartheta - 2R_{y,z}^2 \cos \vartheta) \sin \varphi, \quad (5.123)$$

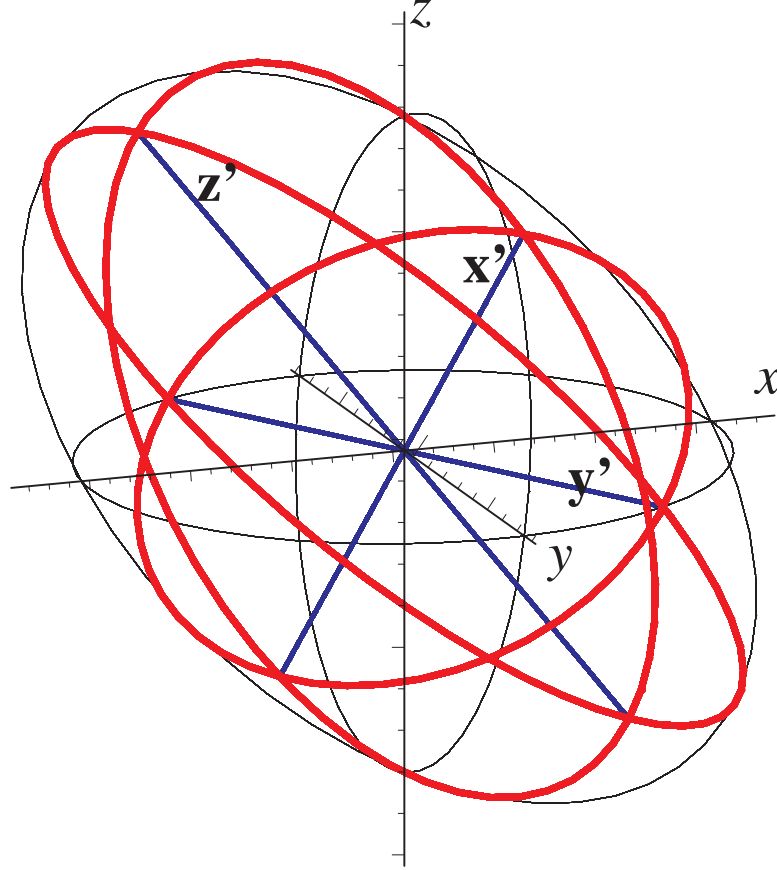


Figure 5.3: The coordinate transformation

The old coordinate system (x, y, z) is shown with thin lines, the new (x', y', z') with thick lines. The axes of the new coordinate system are the main axes of the ellipsoid. The ellipsoid is drawn with thick lines. It's sections with the xy , yz and zx coordinate planes are drawn with thin lines. The ratio of the three main axes are in this case 3 : 4 : 5, while $\vartheta = \pi/5$ and $\varphi = \pi/4$.

if we introduce

$$R_x'^2 = R_x^2 \cos^2 \vartheta + R_z^2 \sin^2 \vartheta + 2R_{x,z}^2 \cos \vartheta \sin \vartheta, \quad \text{and} \quad (5.124)$$

$$R_{x,y}^2 = R_{x,y}^2 \cos \vartheta + R_{y,z}^2 \sin \vartheta \quad (5.125)$$

In the LCMS frame, where $\beta_z = \beta_y = 0$:

$$R_o^2 = R_x'^2 \cos^2 \varphi + R_y'^2 \sin^2 \varphi, \quad (5.126)$$

$$R_s^2 = R_x'^2 \sin^2 \varphi + R_y'^2 \cos^2 \varphi, \quad (5.127)$$

$$R_l^2 = R_x'^2 \sin^2 \vartheta + R_z^2 \cos^2 \vartheta - 2R_{x,z}^2 \sin \vartheta \cos \vartheta, \quad (5.128)$$

$$2R_{o,s}^2 = (R_y'^2 - R_x'^2) \sin 2\varphi \quad (5.129)$$

$$2R_{s,l}^2 = -(R_z^2 \sin 2\vartheta - R_x'^2 \sin 2\vartheta + 2R_{x,z}^2 \cos 2\vartheta) \sin \varphi, \quad (5.130)$$

$$2R_{l,o}^2 = +(R_z^2 \sin 2\vartheta - R_x'^2 \sin 2\vartheta + 2R_{x,z}^2 \cos 2\vartheta) \cos \varphi. \quad (5.131)$$

I computed also the azimuthal sensitivity of the HBT radii in this latter simple case (see equations 5.126-5.131), for the parameter set obtained in section 5.5 and summarized in table 5.2. The plots are shown in figure 5.4.

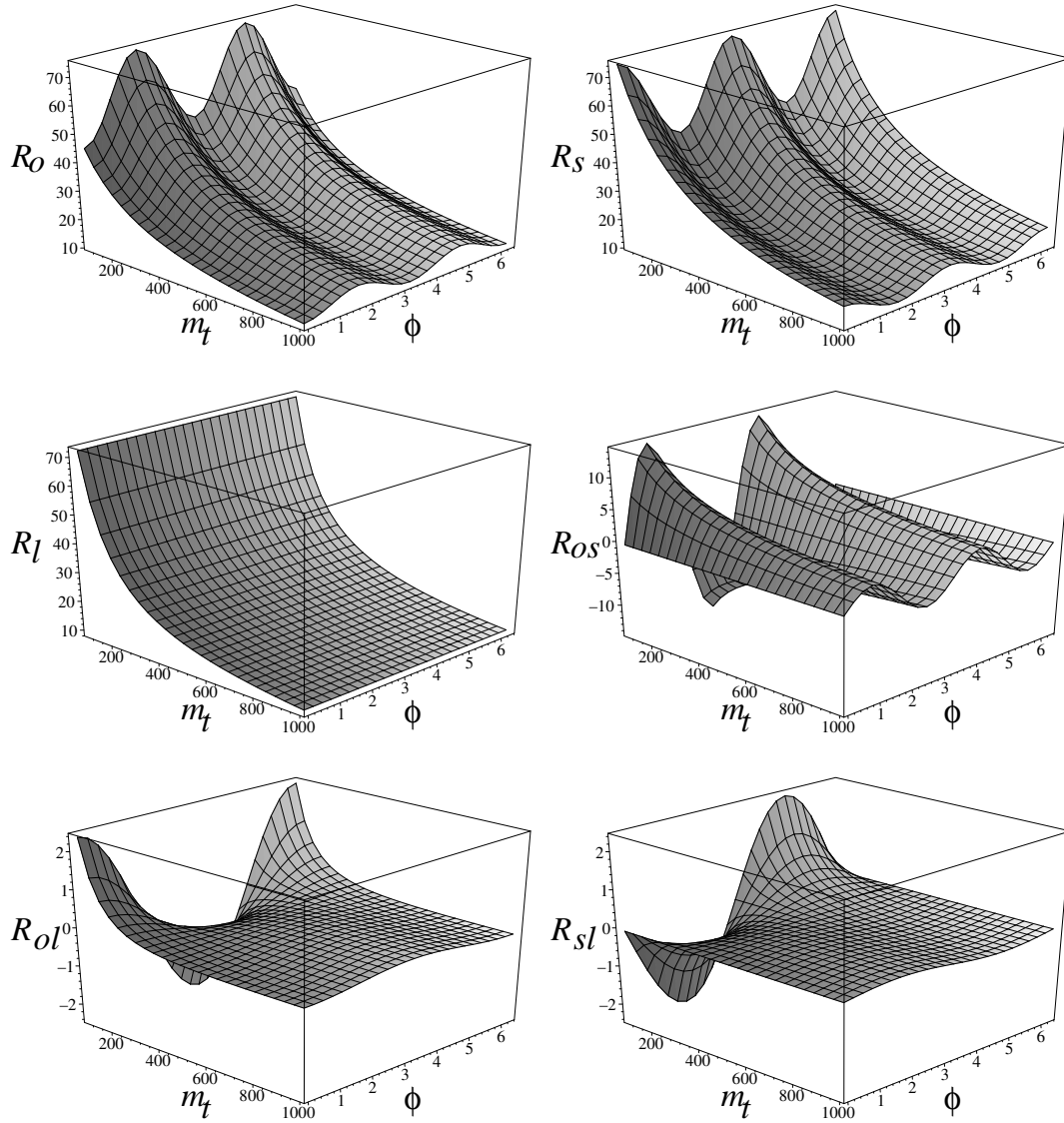


Figure 5.4: Azimuthal sensitivity of the HBT radii

On these figures, we see the transverse mass (m_t) and azimuthal angle (ϕ) dependence of the HBT radii. The period in R_O , R_S and $R_{O,s}$ is π , in $R_{S,l}$ and $R_{l,o}$ it is 2π , and R_l does not depend on ϕ , as it is shown in equations 5.126-5.131.

5.5 Comparing the ellipsoidal model to the data

5.5.1 Elliptic flow for tilted ellipsoidal expansion

Now, let us compute the elliptic flow for tilted, ellipsoidally expanding sources, too, because we can get a non-vanishing v_1 and v_3 only this way, in case of $\vartheta \neq 0$, similarly to the non-relativistic case discussed in ref. [70]. The observables are determined in the center of mass frame of the collision (CMS or LAB frame), where the r_x axis points to the direction of the impact parameter and the r_z axis points to the direction of the beam. In this frame, the ellipsoidally expanding fireball, described in the previous subsections, may be rotated. So let us assume, that we re-label all the x and p coordinates in the previous parts with the superscript $'$, e.g. $x \rightarrow x'$ and $p \rightarrow p'$, to indicate that these calculations were performed in the system of ellipsoidal expansion (SEE), where the principal axis of the expanding ellipsoid coincide with the principal axis of SEE. In the following, we use the unprimed variables to denote quantities defined in the CMS, the frame of observation.

We assume, that the initial conditions of the hydrodynamic evolution correspond to a rotated ellipsoid in CMS [70]. The tilt angle ϑ represents the rotation of the major (longitudinal) direction of expansion, r'_z , from the direction of the beam, r_z . Hence the event plane is the (r'_x, r'_z) plane, which is the same, as the (r_x, r_z) plane. The (zenithal) angle between directions r_z and r'_z is the tilt angle ϑ , while (azimuthal) angle φ is between the event plane and the direction of the transverse momentum p_t .

The definition of v_n is:

$$N'_1 = \frac{dn}{dp'_z p'_t dp'_t d\varphi} = \frac{dn}{dp'_z p'_t dp'_t 2\pi} \left(1 + 2 \sum_n v_n \cos(n\varphi) \right) \quad (5.132)$$

where the $'$ means, that we have the IMD in the system of ellipsoidal expansion. From this equation follows:

$$\frac{\frac{dn}{dp'_z p'_t dp'_t d\varphi}}{\frac{dn}{dp'_z p'_t dp'_t 2\pi}} = \left(1 + 2 \sum_n v_n \cos(n\varphi) \right) \quad (5.133)$$

From the invariant momentum distribution, v_m can be calculated as follows:

$$v_m = \int_0^{2\pi} \frac{dn}{dp_z p_t dp_t d\varphi} \cos(m\varphi) d\varphi \quad (5.134)$$

We have made the coordinate transformation

$$p'_x = p_x \cos \vartheta - p_z \sin \vartheta, \quad (5.135)$$

$$p'_y = p_y, \quad (5.136)$$

$$p'_z = p_z \cos \vartheta + p_x \sin \vartheta, \quad (5.137)$$

and in addition:

$$p_x = p_t \cos \varphi, \quad (5.138)$$

$$p_y = p_t \sin \varphi, \quad (5.139)$$

The changes in the coordinates are taken in first order in ϑ .

$$N_1(m_t, p_x, p_y, y) \rightarrow N'_1(m'_t, p'_t, \varphi, y) \quad (5.140)$$

$$p_x(m'_t, y', p'_t, \varphi) = p'_t \cos \varphi - (m'_t \sinh y') \vartheta \quad (5.141)$$

$$p_y(m'_t, y', p'_t, \varphi) = p'_t \sin \varphi \quad (5.142)$$

$$y(m'_t, y', p'_t, \varphi) = y' + \left(\frac{p'_t}{m'_t} \cosh y' \cos \varphi \right) \vartheta \quad (5.143)$$

$$m_t(m'_t, y', p'_t, \varphi) = m'_t - (p'_t \sinh y' \cos \varphi) \vartheta \quad (5.144)$$

Now, with second order calculations in p/T_0 and first order in ϑ , we get for $b(x_s, p') = \ln B(x_s, p')$:

$$\begin{aligned} b(x_s, p') &= \frac{p_t'^2 \cos^2 \varphi}{2m_t \tilde{T}'_{*,x}} + \frac{p_t'^2 \sin^2 \varphi}{2m_t \tilde{T}'_{*,y}} + \frac{p_z'^2}{2m_t \tilde{T}'_{*,z}} + \\ &+ \frac{p_t' p_z'}{m_t} \vartheta \cos \varphi \left(\frac{1}{\tilde{T}'_{*,z}} - \frac{1}{\tilde{T}'_{*,x}} \right) + \frac{1}{T_0} \left(\mu_0 - m_t + \frac{p_t'^2}{m_t} \right) \end{aligned} \quad (5.145)$$

Here for $i = x, y, z$

$$T'_{*,i} = T_0 \left(1 + m_t' \frac{\dot{R}_i^2}{T_0 + m_t' a^2} \right), \quad (5.146)$$

and

$$\frac{1}{\tilde{T}'_{*,x}} = \frac{\cos^2 \vartheta}{T'_{*,x}} + \frac{\sin^2 \vartheta}{\tilde{T}'_{*,z}} \simeq \frac{1}{T'_{*,x}} \quad (5.147)$$

$$\frac{1}{\tilde{T}'_{*,z}} = \frac{\cos^2 \vartheta}{T'_{*,z}} + \frac{\sin^2 \vartheta}{\tilde{T}'_{*,x}} \simeq \frac{1}{T'_{*,z}} \quad (5.148)$$

From the experiments, we now, that

$$m_t \cosh(\eta_s - y) \frac{\Delta \tau_*}{\Delta \tau} 2\pi R_{*,x} R_{*,y} \sqrt{2\pi \tau_0^2 \Delta \eta_*^2} = \left(\frac{T_0}{m_t} \right)^\alpha \quad (5.149)$$

$$= \left(\frac{T_0}{m_t'} \right)^\alpha (1 + C_1 \alpha \cos \varphi \vartheta) \quad (5.150)$$

so finally, we get:

$$N_1(m_t', p_t', \varphi, y) = C_0 (1 + C_1 \alpha \vartheta \cos \varphi) e^{w' \cos 2\varphi + c_2 \vartheta \cos \varphi + C_3 \vartheta \cos(3\varphi)} \quad (5.151)$$

where C_i may depend on all variables, except φ . So we get for the IMD, with a first order calculation in ϑ :

$$N_1(m_t', p_t', \varphi, y) \sim (1 + (\beta_1 \cos \varphi + \beta_2 \cos(3\varphi)) \vartheta) e^{w' \cos 2\varphi} \quad (5.152)$$

Now, we can calculate v_n . For this, the following rule is very useful:

$$\cos(n_1 \varphi) \cos(n_2 \varphi) = \frac{1}{2} (\cos((n_1 + n_2) \varphi) + \cos((n_1 - n_2) \varphi)) \quad (5.153)$$

Finally, we get:

$$v_{2n} = \frac{I_n(w')}{I_0(w')} \quad (5.154)$$

$$v_{2n+1} = \frac{\vartheta \beta_1}{2} \left(\frac{I_n(w') + I_{n+1}(w')}{2} \right) + \frac{\vartheta \beta_2}{2} \left(\frac{I_{|n-1|}(w') + I_{n+2}(w')}{2} \right) \quad (5.155)$$

Here, the argument w is the same, as before, only, that it depends on the transformed coordinates:

$$w' = \frac{p_t'^2}{4m_t'} \left(\frac{1}{T'_{*,y}} - \frac{1}{T'_{*,x}} \right) \quad (5.156)$$

In our case:

$$\begin{aligned} \beta_1 &= -\frac{p_t'^3 \sinh y'}{2m_t'^2} \left(\frac{3}{2} \frac{1 + \frac{\dot{X}^2}{a^2}}{T_{*,x}'^2} + \frac{1}{2} \frac{1 + \frac{\dot{Y}^2}{a^2}}{T_{*,y}'^2} - \frac{1}{T_0} \right) - \\ &- p_t' \sinh y' \left(\frac{1}{T'_{*,z}} - \frac{1}{T'_{*,x}} \right) + \frac{p_t'}{m_t'} \alpha \sinh y' \cos \varphi \end{aligned} \quad (5.157)$$

$$\beta_2 = -\frac{p_t'^3 \sinh y'}{2m_t'^2} \frac{1}{2} \left(\frac{1 + \frac{\dot{X}^2}{a^2}}{T_{*,x}'^2} - \frac{1 + \frac{\dot{Y}^2}{a^2}}{T_{*,y}'^2} \right) \quad (5.158)$$

Specially:

$$v_1 = \frac{\beta_1}{2} \left(\frac{I_0(w') + I_1(w')}{2} \right) + \frac{\beta_2}{2} \left(\frac{I_1(w') + I_2(w')}{2} \right) \quad (5.159)$$

$$v_2 = \frac{I_1(w')}{I_0(w')} \quad (5.160)$$

$$v_3 = \frac{\beta_1}{2} \left(\frac{I_1(w') + I_2(w')}{2} \right) + \frac{\beta_2}{2} \left(\frac{I_0(w') + I_3(w')}{2} \right) \quad (5.161)$$

These are the easy-to-understand-formulas, but it is a better way to fit the data, if we use a numeric integration over phi, and so, we get a more exact v_2 function.

5.5.2 Comparing v_2 to the data

At first, let's look at v_2 at mid-rapidity, $v_2(y = 0, p_t)$! $y = 0$ means $p_z = 0$, and as we saw, the IMD looks like:

$$N_1(p) = \frac{1}{\sqrt{\lambda_*}} \frac{g}{(2\pi)^3} p_\mu u^\mu(x_s) \frac{\Delta\tau_*}{\Delta\tau} [\det R_{i,j}^2]^{1/2} \frac{1}{B(x_s, p) + s_q} \quad (5.162)$$

In this special case, and in the $\eta_i \ll 1$ for $i = x, y$ limit:

$$B(x_s, p) = \exp \left[-\frac{p_x^2 \dot{X}^2}{2T_0^2(1 + (a^2 + \dot{X}^2)m_t/T_0)} - \frac{p_y^2 \dot{Y}^2}{2T_0^2(1 + (a^2 + \dot{Y}^2)m_t/T_0)} + \frac{m_t}{T_0} \right] \quad (5.163)$$

Here, we can make the transformation and calculate v_2 , and so we get a more exact result. But it is impossible to find the exact form of $v_2(y)$, we have to make some extrapolations, so we decided to compare the elliptic flow to the data with the exact starting formulas, but we do integrate numerically, and compute the saddle point with a successive approximation. The successive approximation means a loop here instead of solving the non-analytic equations. We have chosen a loop enough long, that means, that a longer loop won't modify the results. This was the same with the width of the integration-step. We integrated $N_1(p)$ over p_t , as the data were taken this way, too.

Finally, we calculated the transverse momentum and the pseudorapidity dependence of v_2 for a parameter set determined from fitting the axially symmetric version of the Buda-Lund hydro model to single particle pseudo-rapidity distribution of BRAHMS [64] and PHOBOS [45], the mid-rapidity transverse momentum spectra of identified particles as measured by PHENIX [48, 71] and the two-particle Bose-Einstein correlation functions or HBT radii as measured by the PHENIX [44] and STAR [46] collaborations. The only difference is, that in the present calculations \dot{X}_f and \dot{Y}_f were splitted and a tilt angle ϑ was introduced.

We determined the harmonic moment of eq. (5.134) numerically, for the case of $m = 2$, but using the analytic expression of eq. (5.78) for the invariant momentum distribution, computing the coordinates of the saddle point with a successive approximation. The successive approximation means a loop here instead of solving the non-analytic saddle-point equations. We have chosen a loop long enough and have checked that an even longer loop will not modify the results. This was the same with the width of the integration-step. We integrated $N_1(p)$ over p_t , as the data were taken this way, too. Finally, we were able to fit $v_2(\eta = 0, p_t)$ and $v_2(\eta)$ with the same set of parameters.

The results are summarized both in figures 5.5 and 5.6. We find that a small asymmetry in the expansion gives a natural description of the transverse momentum dependence of v_2 . The parameters are taken from the results Buda-Lund hydro model fits to the two-particle Bose-Einstein correlation data (HBT radii) and the single particle spectra of Au + Au collisions at $\sqrt{s_{NN}} = 130$ GeV, ref. [19, 66], where the axially symmetric version of the model was utilized. Here we have introduced parameters that control the asymmetry of the expansion in the X and Y directions such a way that the angular averaged, effective source is unchanged. For example,

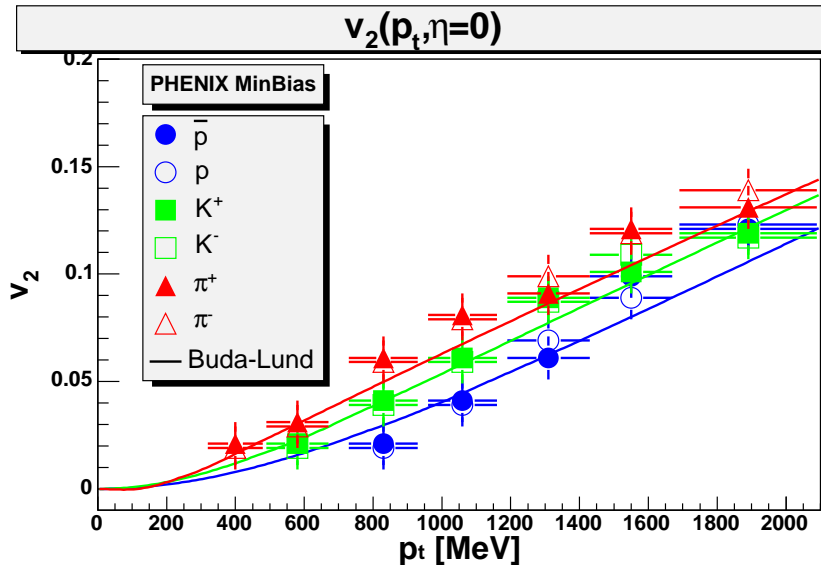


Figure 5.5: Buda-Lund results compared to the $v_2(p_t)$ data

Here we see the fit to the PHENIX $v_2(p_t)$ data of identified particles [25]. The parameter set is: $T_0 = 210$ MeV, $\dot{X} = 0.57$, $\dot{Y} = 0.45$, $\dot{Z} = 2.4$, $a = 1$, $\tau_0 = 7$ fm/c, $\vartheta = 0.09$, $X_f = 8.6$ fm, $Y_f = 10.5$ fm, $Z_f = 17.5$ fm, $\mu_{0,\pi} = 70$ MeV, $\mu_{0,K} = 210$ MeV and $\mu_{0,p} = 315$ MeV, and the masses are taken as their physical value.

we required that the effective temperature, T_{eff} of eq. (5.93) is unchanged. We see on 5.5 and 5.6 that this method was successful in reproducing the data on elliptic flow, with a small asymmetry between the two transverse expansion rates.

From the fit given on figure 5.5, we calculate the value of the transverse momentum integrated $v_2(\eta = 0)$ and find that this value is below the published PHOBOS data point at mid-rapidity. We attribute this difference of 0.02 to a non-flow contribution [72]. The PHOBOS collaboration pointed out the possible existence of such a term in their data in ref. [26], as they did not utilize the fourth order cumulant method to determine v_2 . The magnitude of the non-flow contribution has been explicitly studied at mid-rapidity by the STAR collaboration and indeed STAR found that its value is of the order of 0.01 for mid-rapidity minimum bias data, ref. [61].

The good description of the $dn/d\eta$ distribution by the Buda-Lund hydro model [19, 66] is well reflected in the good description of the pseudo-rapidity dependence of the elliptic flow. Thus the finiteness of the expanding fireball in the longitudinal direction and the scaling three dimensional expansion is found to be responsible for the experimentally observed violations of the boost invariance of both the rapidity distribution and that of the collective flow v_2 .

Furthermore, we note that our best fits correspond to a high, $T_0 > T_c = 170$ MeV central temperature, with a cold surface temperature of $T_s \approx 105$ MeV. The success of this description suggests that a small fraction of pions may be escaping from the fireball from a superheated hadron gas, which can be considered as an indication, that part of the source of Au + Au collisions at RHIC may be a deconfined matter with $T > T_c$. The results are summarized on Fig. 1 and Fig. 2.

Let us determine the size of the volume that is above the critical temperature. Within this picture, one can find the critical value of $s = s_c$ from the relation that $T_0/(1 + as_c) = T_c$. Using $T_0 = 210$ MeV, $T_c = 170$ MeV, and $a = 1$ we find $s_c = 0.235$.

The equation for the surface of the ellipsoid with $T \geq T_c$ is given by

$$\frac{r_x^2}{X_c^2} + \frac{r_y^2}{Y_c^2} + \frac{r_z^2}{Z_c^2} = 1, \quad (5.164)$$

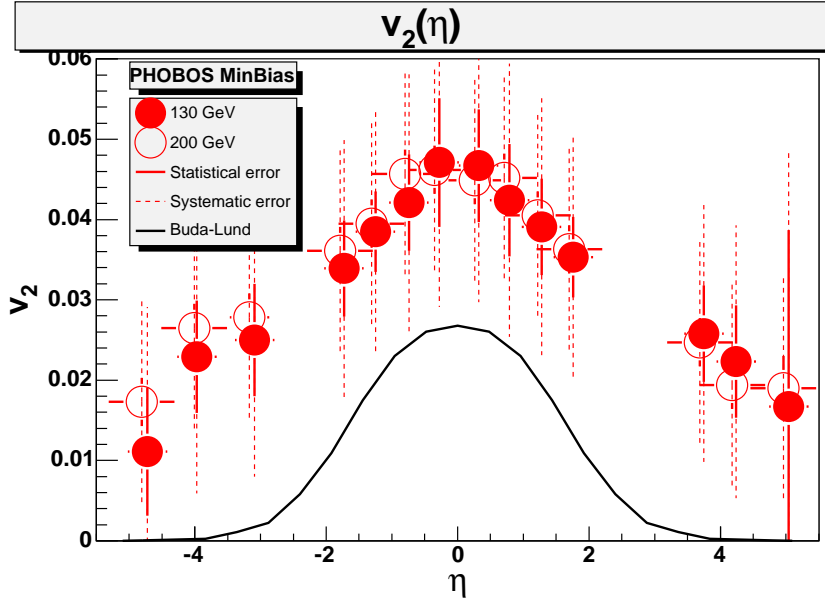


Figure 5.6: Buda-Lund results compared to the $v_2(\eta)$ data

This image shows the fit to the 130 GeV Au+Au and 200 GeV Au+Au $v_2(\eta)$ data of PHOBOS [26, 27], with the ellipsoidal generalization of the Buda-Lund hydro model. Here we used the same parameter set as at Fig. 5.5, with pion mass and chemical potential, and a constant non-flow parameter of 0.02.

where the principal axes of the “critical” ellipsoid are given by

$$X_c = X_f \sqrt{s_c} \simeq 4.2 \text{ fm}, \quad (5.165)$$

$$Y_c = Y_f \sqrt{s_c} \simeq 5.1 \text{ fm}, \quad (5.166)$$

$$Z_c = Z_f \sqrt{s_c} \simeq 8.5 \text{ fm}, \quad (5.167)$$

hence the volume of the ellipsoid with $T > T_c$ is $V_c = \frac{4\pi}{3} X_c Y_c Z_c \approx 753 \text{ fm}^3$.

Note, however, that the characteristic average or surface temperature of the fireball within this model is $T_s = T_0/(1+a) \approx 105 \text{ MeV}$. This temperature is relatively small compared to the Landau estimation of $T_f \approx m_\pi \approx 140 \text{ MeV}$. So the picture is similar to a snow-ball which has a melted core inside.

Our study shows that this picture is consistent with the pseudorapidity and transverse mass dependence of v_2 at RHIC in the soft $p_t < 2 \text{ GeV}$ domain. However, it is not yet a direct proof of the existence of a new phase. Among others, we have to determine the best fit parameters with Minuit and also to get their errors, which will be a subject of further research.

5.6 Predictions

From the definition in eq. 5.134 all harmonic momenta v_m can be calculated. If we calculate it using the parameters obtained from the fits to other data (figures 5.2-5.6) we get a prediction for these momenta. This is plotted on figure 5.7. It is clear in our calculations, that all odd momenta at midrapidity are near zero,

$$v_{2n+1}(p_t, \eta = 0) = 0, \quad (5.168)$$

so only the even harmonics are calculated. One can notice, that v_4 is around 1/10 smaller than v_2 , and v_6 is even smaller by another factor of 1/10, but they have approximately the same shape.

The situation is similar in case of the $v_n(\eta)$ functions. Here v_2 and v_4 have the same shape, just the latter is smaller by a factor of around 1/25, while v_3 is smaller than v_1 by a factor of 1/29.

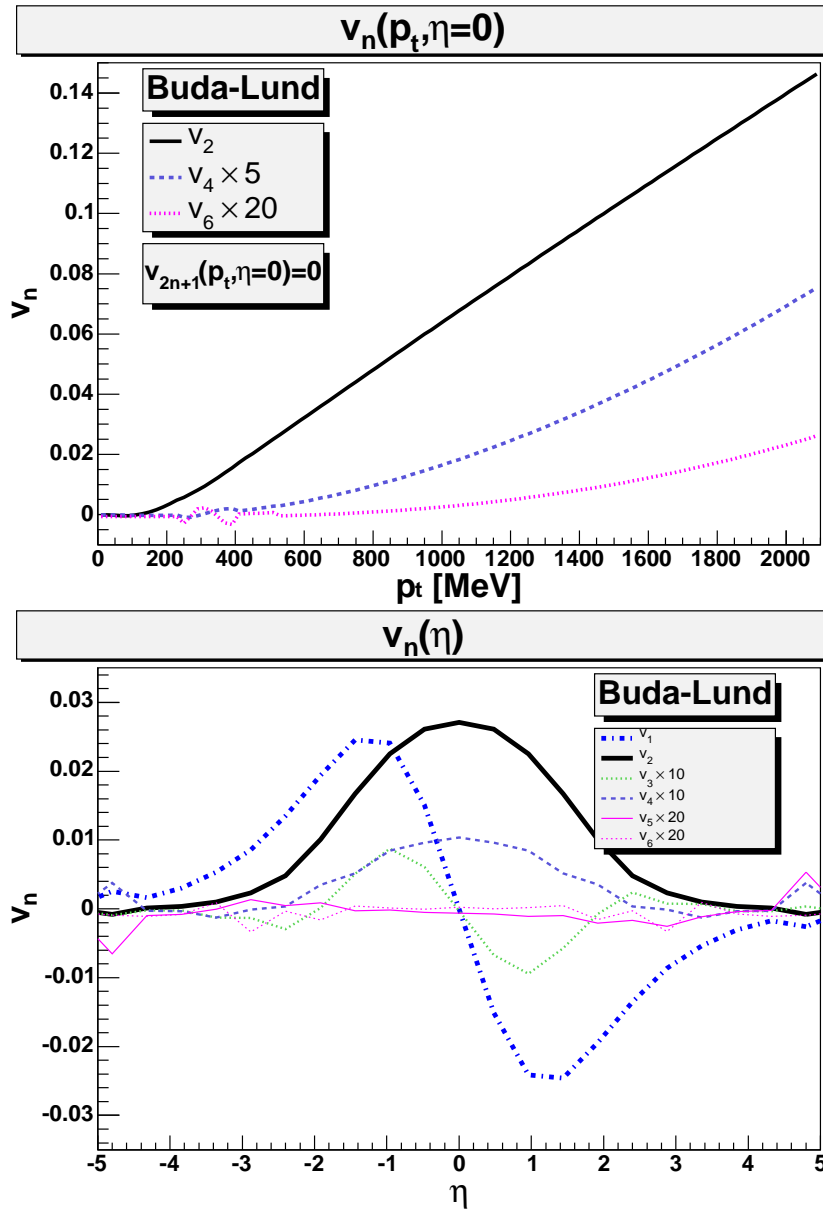


Figure 5.7: Buda-Lund prediction

I calculated higher harmonic momenta with the given set of parameters from figure 5.5. This gives a prediction, which can be later compared to the measured data. On this figure in the above panel the transverse momentum dependence of v_n for $n = 1.6$ is plotted, while below the the pseudorapidity dependence of these harmonics is to see.

The higher harmonics v_5 and v_6 are very small, and the numeric errors in the calculation package are getting even higher than the calculated value especially at high rapidities.

5.7 Summary and conclusions

We have generalized the Buda-Lund hydro model to the case of ellipsoidally symmetric expanding fireballs. We kept the parameters determined from fits to the single particle spectra and the two-particle Bose-Einstein correlation functions (HBT radii) [19, 66], and interpreted them as angular

averages for the direction of the reaction plane. Then we found that a small splitting between the expansion rates parallel and transverse to the direction of the impact parameter. This is due to the fact that the expanding fireball is more compressed in the x direction than in the y direction (see figure 5.8). We also found a small zenithal tilt of the particle emitting source is sufficient to describe simultaneously the transverse momentum dependence of the collective flow of identified particles [25] at RHIC as well as the pseudorapidity dependence of the collective flow [26, 27].

The results in figures 5.5 and 5.6 and in table 5.2 confirm the indication for quark deconfinement at RHIC found in refs. [19, 66], based on the observation, that some of the particles are emitted from a region with higher than the critical temperature, $T > T_c = 170$ MeV. We estimated that the size of this volume is about 1/8-th of the total volume measured on the $\tau = \tau_0$ main freeze-out hypersurface, totalling of about 753 fm^3 .

However, the analysis indicates that the average or surface temperature is rather cold, $T_s \approx 105$ MeV, so approximately 7/8 of the particles are emitted from a rather cold hadron gas, as it is illustrated on figure 5.8.

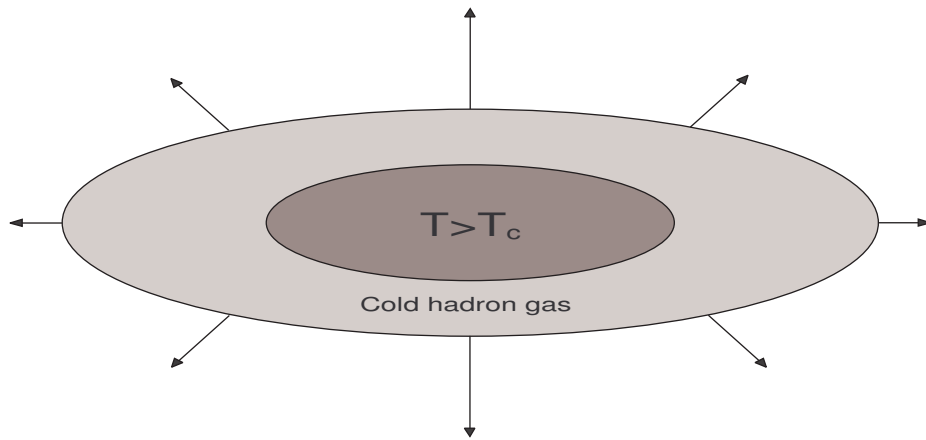


Figure 5.8: The expanding fireball

The expanding ellipsoid has a hot center with $T > T_c$ at the freeze-out, while this central region of 753 fm^3 is surrounded by a rather cold hadron gas. Note, that the expansion rate is higher in that direction where the ellipsoid is more compressed.

BL par.	value	BL par.	value
T_0	210 MeV	\dot{X}_f	0.57
T_s	105 MeV	\dot{Y}_f	0.45
X_f	8.6 fm	\dot{Z}_f	2.4
Y_f	10.5 fm	ϑ	0.09
Z_f	17.5 fm	$\mu_{0,\pi}$	70 MeV
τ_0	7 fm/c	$\mu_{0,K}$	210 MeV
$\Delta\tau$	0 fm/c	$\mu_{0,p}$	315 MeV

Table 5.2: A set of parameters of the ellipsoidal model used on figures 5.5-5.7

In this table I summarized model parameters used to describe the transverse momentum dependence of the collective flow of identified particles [25] at RHIC as well as the pseudorapidity dependence of the collective flow [26, 27]

Chapter 6

Summary

*Gray, my dear friend, is every theory,
And green alone life's golden tree*

FAUST, GOETHE

In my present thesis, I showed three main steps of researching the secrets of Nature: data taking, data analysis and model building, each step through one example. Now I would like to summarize my tasks.

After the hungarian overview and the introduction, in Chapter 3 I wrote about the Relativistic Heavy Ion Collider, about the Pioneering High Energy Nuclear Interaction eXperiment, and about it's Zero Degree Calorimeter.

Here, I have got through with the following tasks:

- Taking shifts at PHENIX
- Developing and maintaining the online monitoring software for ZDC (section 3.6)
- Minor tasks at ZDC
 - Vernier scan and it's analysis(section 3.7)
 - Being a subsystem specialist (section 3.4)

Going forward, in Chapter 4 I summarized my work on the field of data analysis. The present status of this work are first, intermediate plots of the two- and three-particle correlation functions for pions, kaons and protons from the 200 GeV Au+Au data of PHENIX.

The steps of the work were the following:

- Event selection, particle identification, making cuts (section 4.3)
- Computing pair and triplet distributions (subsections 4.4.1 and 4.4.3)
- Computing raw two- and three-particle correlation functions (subsections 4.4.2 and 4.4.4)
- Analysis of the results, determining future tasks (4.5. és 4.6)

In Chapter 5, I showed the last task, model building, through the Buda-Lund hydrodynamical model which I was working on. I made fits to RHIC data with the original, non-relativistic and axially symmetric model, and generalized the model to the relativistic and ellipsoidal symmetric case. Going in details, I did the following:

- Going through the original model (section 5.1)
- Taking part in the study of central collisions (section 5.2)
 - Searching for more exact saddle-points
 - Re-calculating the results of the model
- Developing a generalized, relativistic model with ellipsoidal symmetry(section 5.3)
- Calculating observables from the generalized model (section 5.4)
- Comparing it's results to RHIC data (sections 5.4.3 and 5.5)
- Predictions for new observables (sections 5.6 and 5.4.3)

List of Tables

3.1	PHENIX detector overview	21
3.2	ZDC channels	25
3.3	SMD channels	26
4.1	Event statistics	47
4.2	Statistics for unidentified particles	47
4.3	Statistics for pions	48
4.4	Statistics for kaons	48
4.5	Statistics for protons	48
4.6	Naming convention for the correlation figures	50
5.1	Fit results from RHIC $\sqrt{s_{NN}} = 130$ and 200 GeV data	71
5.2	A set of parameters of the ellipsoidal model used on figures 5.5-5.7	92

List of Figures

3.1	Arial view of RHIC	18
3.2	Detector arrangement in PHENIX during Run 3	22
3.3	Sketch of a high energy heavy ion collision	24
3.4	SMD energy distribution	26
3.5	ZDC main online monitor in a Au+Au run	28
3.6	ZDC main online monitor in a d+Au run	29
3.7	Expert plots in a Au+Au run	30
3.8	Expert plots in a d+Au run	31
3.9	LED energy values versus event number	32
3.10	LED timing values versus event number	33
3.11	Expert plots in a Au+Au run	34
3.12	Expert plots in a Au+Au run	36
3.13	SMD position versus event number	37
3.14	Raw ADC value distributions in the north vertical SMD	38
3.15	Expert plots in a Au+Au run	39
3.16	Vernier scan plots	40
4.1	Results of the NA22 collaboration from ref [15]	45
4.2	Particle identification	46
4.3	Particle and triplet distributions in particular events	49
4.4	Pair distributions for unidentified particles	52
4.5	Pair distributions for identified pions	53
4.6	Pair distributions for identified kaons	54
4.7	Pair distributions for identified protons	55
4.8	Two particle correlation function for unID particles and pions	56
4.9	Two particle correlation function for protons and kaons	57
4.10	Three particle distributions for unidentified particles	58
4.11	Three particle distributions for identified pions	59
4.12	Three particle distributions for identified protons	60
4.13	Three particle distributions for identified kaons	61
4.14	Three particle correlation function for unidentified particles and identified pions	62
4.15	Two particle correlation function for identified kaons and protons	63
4.16	Correraltion function results of L3	64
5.1	Fits to RHIC $\sqrt{s_{NN}} = 130$ and 200 GeV data	72
5.2	Various quantities calculated from the HBT radii	73
5.3	The coordinate transformation	84
5.4	Azimuthal sensitivity of the HBT radii	85
5.5	Buda-Lund results compared to the $v_2(p_t)$ data	89
5.6	Buda-Lund results compared to the $v_2(\eta)$ data	90
5.7	Buda-Lund prediction	91
5.8	The expanding fireball	92

Acknowledgements

I would like to thank Tamás Csörgő, my supervisor, for teaching and guiding me, for talking about the important things which are not certainly part of physics, and for his constant support during my studies.

I would like to thank the PHENIX Collaboration, especially the Global/Hadron Working Group, Gábor Dávid and Péter Tarján for initiating me into the secrets of experimental physics, Sebastian White and Alexei Denisov for teaching me so much about ZDC and SMD.

I am also thankful to Ákos Horváth who gave a starting impulse by guiding me at my first steps and helped me out from my nothing-to-do-what-is-not-a-must laziness.

Of course, I am grateful to my parents and grandparents for their patience, support and *love*. Without them this work would never have come into existence (literally).

Finally, I wish to thank the following:

Ági (for believing in me more than I do),

Ádám, Antal, Bálint, Dávid (for their understanding and support),

Éva, Orsi, Viki (for being always happy about my success),

And a great many other people (for being a great many).

Budapest, Hungary
4th June 2004

Csanád Máté

Bibliography

- [1] <http://www.phenix.bnl.gov/viewcvs/online/monitoring/Run3/subsystems/zdc/>
- [2] R. Hanbury Brown and R. Q. Twiss, *Nature* **178**, 1046 (1956)
- [3] T. Csörgő and B. Lörstad, *Phys. Rev. C* **54** (1996) 1390, hep-ph/9509213
- [4] E. V. Shuryak, hep-ph/0405066.
- [5] K. Adcox *et al.* [PHENIX Coll.], *Phys. Rev. Lett.* **88**, 022301 (2002), nucl-ex/0109003
- [6] S. Adler *et al.* [PHENIX Coll.], *Phys. Rev. Lett.* **91**, 072303 (2003), nucl-ex/0306021
- [7] K. Adcox *et al.* [PHENIX Coll.], *Phys. Rev. Lett.* **88**, 192303 (2002), nucl-ex/0202002
- [8] K. Adcox *et al.* [PHENIX Coll.], *Phys. Rev. Lett.* **89**, 082301 (2002), nucl-ex/0203014
- [9] K. Adcox *et al.* [PHENIX Coll.], *Phys. Rev. C* **66**, 024901 (2002), nucl-ex/0203015
- [10] K. Adcox *et al.* [PHENIX Coll.], *Phys. Rev. Lett.* **89**, 212301 (2002), nucl-ex/0204005
- [11] C. Adler, A. Denisov, E. Garcia, M. Murray, H. Strobele and S. White
Nucl. Instrum. Meth. A **470**, 488 (2001), nucl-ex/0008005
- [12] M. Chiu, A. Denisov, E. Garcia, J. Katzy and S. White
Phys. Rev. Lett. **89**, 012302 (2002), nucl-ex/0109018
- [13] A. J. Baltz, C. Chasman and S. N. White, *Nucl. I. M. A* **417**, 1 (1998), nucl-ex/9801002
- [14] E. O. Alt, T. Csörgő, B. Lörstad and J. Schmidt-Sørensen, hep-ph/0103019.
- [15] T. Csörgő, B. Lörstad, J. Schmid-Sørensen and A. Ster
Eur. Phys. J. C **9**, 275 (1999), hep-ph/9812422
- [16] S. S. Adler *et al.* [PHENIX Coll.], nucl-ex/0401003.
- [17] <http://www.phenix.bnl.gov/viewcvs/offline/analysis/tpcf/>
- [18] P. Achard *et al.* [L3 Coll.], *Phys. Lett. B* **540**, 185 (2002), hep-ex/0206051
- [19] M. Csanád, T. Csörgő, B. Lörstad, A. Ster
Act. Phys. Pol. **B35**, 191 (2004), nucl-th/0311102.
- [20] M. Csanád, T. Csörgő, B. Lörstad and A. Ster, nucl-th/0402037.
- [21] T. Csörgő, M. Csanád, B. Lörstad, A. Ster, nucl-th/0412345
- [22] Z. Fodor and S. D. Katz, *JHEP* **0203** (2002) 014, hep-lat/0106002
- [23] Z. Fodor and S. D. Katz, *JHEP* **0404**, 050 (2004), hep-lat/0402006
- [24] M. Csanád, T. Csörgő and B. Lörstad, nucl-th/0310040.

- [25] S. S. Adler *et al.* [PHENIX Collaboration], nucl-ex/0305013.
- [26] B. B. Back *et al.* [PHOBOS Coll.], Phys. Rev. Lett. **89**, 222301 (2002), nucl-ex/0205021
- [27] S. Manly *et al.* [PHOBOS Coll.], Nucl. Phys. A **715**, 611 (2003), nucl-ex/0210036
- [28] A. Ster, T. Csörgő and B. Lörstad, Nucl. Phys. A **661**, 419 (1999) hep-ph/9907338.
- [29] T. Csörgő, Heavy Ion Phys. **15** (2002) 1, hep-ph/0001233
- [30] J. Bondorf, S. Garpman, J. Zimányi, Nucl. Phys. A **296**, 320 (1978)
- [31] T. Csörgő, hep-ph/0111139.
- [32] T. Csörgő, nucl-th/9809011.
- [33] T. Csörgő and J. Zimányi, Heavy Ion Phys. **17**, 281 (2003), nucl-th/0206051
- [34] T. Csörgő, F. Grassi, Y. Hama, T. Kodama, Phys. Lett. B **565**, 107 (2003), nucl-th/0305059
- [35] T. Csörgő, L. Csernai, Y. Hama, T. Kodama, nucl-th/0306004.
- [36] T. Csörgő and B. Lörstad, Nucl. Phys. A **590** (1995) 465C, hep-ph/9503494
- [37] T. Csörgő, B. Lörstad and J. Zimányi, Z. Phys. C **71** (1996) 491, hep-ph/9411307
- [38] S. Chapman, P. Scotto and U. Heinz, Heavy Ion Phys. **1** (1995) 1, hep-ph/9409349.
- [39] A. Ster, T. Csörgő and J. Beier, Heavy Ion Phys. **10** (1999) 85, hep-ph/9810341
- [40] T. S. Biró, Phys. Lett. B **474** (2000) 21, nucl-th/9911004
- [41] T. S. Biró, Phys. Lett. B **487** (2000) 133, nucl-th/0003027
- [42] I. G. Bearden *et al.* [BRAHMS Coll.], Phys. Lett. B **523** (2001) 227, nucl-ex/0108016
- [43] K. Adcox *et al.* [PHENIX Coll.], Phys. Rev. Lett. **88** (2002) 242301, nucl-ex/0112006
- [44] K. Adcox *et al.* [PHENIX Coll.], Phys. Rev. Lett. **88** (2002) 192302, nucl-ex/0201008
- [45] B. B. Back *et al.* [PHOBOS Coll.], Phys. Rev. Lett. **87** (2001) 102303, nucl-ex/0106006
- [46] C. Adler *et al.* [STAR Coll.], Phys. Rev. Lett. **87** (2001) 082301, nucl-ex/0107008
- [47] I. G. Bearden *et al.* [BRAHMS Coll.], Phys. Rev. Lett. **88** (2002) 202301, nucl-ex/0112001
- [48] S. S. Adler *et al.* [PHENIX Coll.], Phys. Rev. C **69**, 034909 (2004), nucl-ex/0307022
- [49] S. S. Adler [PHENIX Coll.], nucl-ex/0401003.
- [50] <http://www.kfki.hu/~csorgo/budalund/>
- [51] Z. W. Lin, C. M. Ko and S. Pal, Phys. Rev. Lett. **89** (2002) 152301, nucl-th/0204054
- [52] T. J. Humanic, Nucl. Phys. A **715** (2003) 641, nucl-th/0205053
- [53] F. Retiere, J. Phys. G **30** (2004) S335, nucl-ex/0307026
- [54] F. Retiere and M. A. Lisa, nucl-th/0312024.
- [55] T. Hirano and K. Tsuda, Nucl. Phys. A **715** (2003) 821, nucl-th/0208068
- [56] W. Broniowski, A. Baran and W. Florkowski
AIP Conf. Proc. **660** (2003) 185, nucl-th/0212053
- [57] W. Florkowski and W. Broniowski, AIP Conf. Proc. **660** (2003) 177, nucl-th/0212052

- [58] W. Broniowski and W. Florkowski, Phys. Rev. Lett. **87** (2001) 272302, nucl-th/0106050
- [59] T. Csörgő and A. Ster, Heavy Ion Phys. **17** (2003) 295, nucl-th/0207016
- [60] K. Adcox *et al.* [PHENIX Coll.], Phys. Rev. Lett. **89**, 212301 (2002), nucl-ex/0204005
- [61] C. Adler *et al.* [STAR Coll.], Phys. Rev. C **66**, 034904 (2002), nucl-ex/0206001
- [62] C. Adler *et al.* [STAR Coll.], Phys. Rev. Lett. **87**, 182301 (2001), nucl-ex/0107003
- [63] J. D. Bjorken, Phys. Rev. D **27**, 140 (1983).
- [64] I. G. Bearden *et al.* [BRAHMS Coll.], Phys. Rev. Lett. **90**, 102301 (2003).
- [65] W. Reisdorf and H. G. Ritter, Ann. Rev. Nucl. Part. Sci. **47**, 663 (1997).
- [66] T. Csörgő and A. Ster, Heavy Ion Phys. **17**, 295 (2003), nucl-th/0207016
- [67] A. Ster, T. Csörgő and B. Lörstad, Nucl. Phys. A **661**, 419 (1999), hep-ph/9907338
- [68] N. M. Agababian *et al.* [EHS/NA22 Coll.], Phys. Lett. B **422**, 359 (1998), hep-ex/9711009
- [69] T. Csörgő and Y. Hama, manuscript in preparation
- [70] T. Csörgő, S. V. Akkelin, Y. Hama, B. Lukács, Y. M. Sinyukov
Phys. Rev. C **67**, 034904 (2003), hep-ph/0108067
- [71] K. Adcox *et al.* [PHENIX Coll.], Phys. Rev. C **69**, 024904 (2004), nucl-ex/0307010
- [72] N. Borghini, P. M. Dinh and J. Y. Ollitrault
Phys. Rev. C **63**, 054906 (2001), nucl-th/0007063
N. Borghini, P. M. Dinh and J. Y. Ollitrault
Phys. Rev. C **64**, 054901 (2001), nucl-th/0105040